

Very low-grade metamorphism of the Dezadeash flysch (Jura-Cretaceous): Constraints on the burial history of the Nutzotin-Dezadeash basin and implications regarding the tectonic evolution of the Northern Cordillera of Alaska and Yukon

Lowey Grant¹

¹Home

November 16, 2022

Abstract

Secondary mineral assemblages in sandstone and tuff indicate high temperature zeolite facies metamorphism; Kübler indices of illite and Árkai indices of chlorite in mudstone record diagenetic to high anchizone metapelitic conditions; and pyrolysis of organic matter and the color of organic matter (i.e., the Thermal Alteration Index of palynomorphs and the Conodont Alteration Index) in mudstone and hemipelagite beds suggest thermal maturation reached catagenesis to mesogenesis stages. Collectively, the mineralogic and organic thermal indicators suggest the Dezadeash Formation was subject to pressure-temperature (P-T) conditions of 2.5 kbar and 250 °C. The estimated P-T conditions, together with published thermochronometric data, shows that the Dezadeash Formation underwent rapid, short-term heating followed by gradual, long-term cooling. Moreover, a calculated tectonic subsidence curve indicates rapid, short-term subsidence, followed by gradual, long-term uplift. Secondary clay minerals associated with heating and subsidence are characterized by a restricted assemblage dominated by 2M₁ illite and chlorite. The thermal history, subsidence history, and secondary clay mineral assemblage are not supportive of deposition in peripheral foreland, backarc, strike-slip, and rift basins; nor are the results corroborative with previous deformation and crustal-scale reconstructions depicting the Dezadeash Formation being underthrust >20 km beneath the Blanchard River assemblage, Kluane Schist, and Yukon composite terrane (YCT). The Dezadeash-Nutzotin basin contrasts sharply with the contemporaneous Gravina belt and Gravina sequence in southeastern Alaska that were apparently underthrust >20 km beneath the YCT. The contrasting tectono-metamorphic histories may be a manifestation of oblique collision and diachronous, south-to-north accretion of the Chitina arc and WCT to YTC.

Hosted file

loweydez2020palynotables3.docx available at <https://authorea.com/users/523131/articles/595172-very-low-grade-metamorphism-of-the-dezadeash-flysch-jura-cretaceous-constraints-on-the-burial-history-of-the-nutzotin-dezadeash-basin-and-implications-regarding-the-tectonic-evolution-of-the-northern-cordillera-of-alaska-and-yukon>

Hosted file

loweydez2020conodonttables4.docx available at <https://authorea.com/users/523131/articles/595172-very-low-grade-metamorphism-of-the-dezadeash-flysch-jura-cretaceous-constraints-on-the-burial-history-of-the-nutzotin-dezadeash-basin-and-implications-regarding-the-tectonic-evolution-of-the-northern-cordillera-of-alaska-and-yukon>

Hosted file

loweydez2020rkevaltables5.docx available at <https://authorea.com/users/523131/articles/595172-very-low-grade-metamorphism-of-the-dezadeash-flysch-jura-cretaceous-constraints-on-the-burial-history-of-the-nutzotin-dezadeash-basin-and-implications-regarding-the-tectonic-evolution-of-the-northern-cordillera-of-alaska-and-yukon>

Hosted file

loweydez2020stationstables1.docx available at <https://authorea.com/users/523131/articles/595172-very-low-grade-metamorphism-of-the-dezadeash-flysch-jura-cretaceous-constraints-on-the-burial-history-of-the-nutzotin-dezadeash-basin-and-implications-regarding-the-tectonic-evolution-of-the-northern-cordillera-of-alaska-and-yukon>

Hosted file

loweydez2020xrddtables2.docx available at <https://authorea.com/users/523131/articles/595172-very-low-grade-metamorphism-of-the-dezadeash-flysch-jura-cretaceous-constraints-on-the-burial-history-of-the-nutzotin-dezadeash-basin-and-implications-regarding-the-tectonic-evolution-of-the-northern-cordillera-of-alaska-and-yukon>

1 **Very low-grade metamorphism of the Dezadeash flysch (Jura-Cretaceous):**
2 **Constraints on the burial history of the Nutzotin-Dezadeash basin and**
3 **implications regarding the tectonic evolution of the Northern Cordillera of**
4 **Alaska and Yukon**

5
6
7
8 Grant W. Lowey

9 Whitehorse, Yukon

10 Corresponding Author: Grant Lowey (loweygrant@gmail.com)

11
12
13 **Key Points:**

- 14 * mineralogic and organic thermal indicators record mainly high temperature
15 zeolite facies metamorphism, diagenetic to anchizone metapelitic conditions, and
16 catagenesis to metagenesis thermal maturation stages
- 17 * the thermal history, subsidence history, and secondary mineral assemblages do
18 not support peripheral foreland, backarc, strike-slip, or rift basin settings
- 19 * unlike the contemporaneous Gravina belt and Gravina sequence in southeast
20 Alaska, the Dezadeash formation was not underthrust to > 20 km beneath the
21 Yukon composite terrane

22

23 **Abstract**

24 Secondary mineral assemblages in sandstone and tuff indicate high temperature zeolite facies
25 metamorphism; Kübler indices of illite and Árkai indices of chlorite in mudstone record
26 diagenetic to high anchizone metapelitic conditions; and pyrolysis of organic matter and the
27 color of organic matter (i.e., the Thermal Alteration Index of palynomorphs and the Conodont
28 Alteration Index) in mudstone and hemipelagite beds suggest thermal maturation reached
29 catagenesis to mesogenesis stages. Collectively, the mineralogic and organic thermal indicators
30 suggest the Dezadeash Formation was subject to pressure-temperature (P-T) conditions of 2.5
31 kbar and 250 °C. The estimated P-T conditions, together with published thermochronometric
32 data, shows that the Dezadeash Formation underwent rapid, short-term heating followed by
33 gradual, long-term cooling. Moreover, a calculated tectonic subsidence curve indicates rapid,
34 short-term subsidence, followed by gradual, long-term uplift. Secondary clay minerals associated
35 with heating and subsidence are characterized by a restricted assemblage dominated by 2M₁ illite
36 and chlorite. The thermal history, subsidence history, and secondary clay mineral assemblage are
37 not supportive of deposition in peripheral foreland, backarc, strike-slip, and rift basins; nor are
38 the results corroborative with previous deformation and crustal-scale reconstructions depicting
39 the Dezadeash Formation being underthrust >20 km beneath the Blanchard River assemblage,
40 Kluane Schist, and Yukon composite terrane (YCT). The Dezadeash-Nutzotin basin contrasts
41 sharply with the contemporaneous Gravina belt and Gravina sequence in southeastern Alaska
42 that were apparently underthrust >20 km beneath the YCT. The contrasting tectono-metamorphic
43 histories may be a manifestation of oblique collision and diachronous, south-to-north accretion
44 of the Chitina arc and WCT to YTC.

45

46 **1. Introduction**

47 The Mesozoic convergence and subsequent collision of the Wrangellia composite terrane
48 with the western margin of Laurasia was accompanied by the formation of several flysch basins.
49 The flysch basins are preserved as relatively thick, variably deformed Jurassic-Cretaceous
50 sedimentary and volcanic rocks scattered along the Northern Cordillera of Alaska and Yukon
51 (Fig. 1). Conflicting basin settings have been proposed for these Jurassic-Cretaceous sedimentary
52 and volcanic rocks, including: backarc basins (Berg et al., 1972; Plafker et al., 1989; Cohen and
53 Lundberg, 1993; Monger et al., 1994; Gehrels et al., 2009; Yokelson et al., 2015); intra-arc
54 basins (Berg et al., 1972; McClelland et al., 1991; van der Heyden, 1992; Trop and Ridgway,
55 2007); forearc basins (Moore and Connelly, 1979; Gehrels and Berg, 1994; Trop and Ridgway,
56 2007; Lowey, 2019), retroarc foreland basins (Trop et al., 2002; Manuszak et al., 2007; Trop and
57 Ridgway, 2007; Hampton et al., 2010); collisional foreland basins (Trop and Ridgway, 2007);
58 remnant ocean basins (Nokleberg et al., 1985; Ridgway et al., 2002; Trop and Ridgway, 2007;
59 Hampton et al., 2010), transtensional basins (McClelland et al., 1992; Cohen and Lundberg,
60 1993; Anderson, 2015); and rift basins (Brew and Ford, 1983). The spate of inferred basins is
61 due in part to the paucity of matter-of-fact constraints on basin position and type: previous
62 research focused mainly on determining depositional environments and provenance of the
63 Jurassic-Cretaceous rocks, but depositional environments are generally non-unique with regards
64 to basin type and tectonic setting (Reading, 1980; MacDonald, 1993; Dalrymple, 2010).
65 Furthermore, provenance studies utilizing the framework mode of sandstones tend to provide
66 only generalized and overlapping “provenance terranes” reflecting a variety of tectonic settings
67 (Dickinson and Suczek, 1979; Dickinson et al., 1983; Boggs, 2009), whereas provenance studies
68 relying on detrital zircon geochronology may result in the misidentification of potential source

69 terranes (and hence tectonic settings) due to biases in data manipulation related to discordance
70 filters, concealed lead loss, and common lead correction (Anderson, et al., 2019), as well as
71 biases resulting from differential igneous zircon fertility, sediment sorting, and preservation
72 potential compared with other detrital minerals such as monazite (Moecher and Sampson, 2006;
73 Hietpas et al., 2010; Ibañez-Mejia et al., 2018).

74 Plate tectonics exerts a first-order control on the basin fill because the tectonic setting
75 determines the local geothermal gradient, subsidence mechanism, sediment accumulation rate,
76 available mineral and rock fragment composition, pore fluid composition, water circulation (i.e.,
77 porosity and permeability), and general basin type (Siever, 1979; Blatt, 1992). Hence, additional
78 constraints on the type of basin and its tectonic setting may be obtained by analysing the post-
79 depositional history of the basin fill, specifically determining diagenetic zones, metamorphic
80 facies, thermal history, and subsidence history of strata comprising the basin. For example,
81 Merriman (2002, 2005) utilized diagenetic and metamorphic clay mineral assemblages to infer
82 the tectonic setting of sedimentary basins: mudstones that evolved in extensional basins
83 contained a complex assemblage of clay minerals comprising K-, Na/K-, Na-micas and
84 pyrophyllite, as well as chlorite/mica stacks, compared with mudstones that evolved in
85 convergent basins that displayed a simple clay mineral assemblage of K-white mica and chlorite.
86 In addition, Xie and Heller (2009) employed tectonic subsidence curves to distinguish between
87 passive margin, strike-slip, and foreland basins: subsidence histories record isostatic adjustment
88 to lithospheric processes such as thermal events and sediment loading, and tectonic subsidence
89 curves reflect basin subsidence caused exclusively by a tectonic or driving mechanism,
90 calculated by removing subsidence produced by non-tectonic processes such as compaction and

91 sediment loading (i.e., "backstripping"), as well as water depth changes (Bond and Kominz,
92 1984).

93 Temperature is possibly the most important parameter affecting the basin fill since it
94 influences many of the post-depositional physical properties of sediments and pore fluids, and
95 basin thermal histories are thought to be indicative of tectonic setting and associated basins
96 (Allen and Allen, 2013). Consequently, Stone and Merriman (2004) proposed that a "basin
97 thermal history test" be undertaken as part of any terrane analysis, particularly collapsed flysch
98 basins comprising thick, variably deformed strata for which the tectonic setting is ambiguous. A
99 basin thermal history test attempts to distinguish between basins with normal or near-normal
100 paleogeothermal gradients, commonly associated with passive margins, oceanic trenches,
101 forearc, and foreland basins, from hotter-than-normal paleogeothermal gradients typical of
102 backarc, rift, and lithospheric-scale strike-slip basins (Stone and Merriman, 2004; Allen and
103 Allen, 2013). The thermal history of a sedimentary basin can be inferred from a variety of low-
104 temperature geothermometers, such as: temperature-sensitive quartz and calcite microstructures
105 (Weber et al., 2001); homogenization temperatures of fluid inclusions that indicate the minimum
106 temperature of entrapment of the fluid (Randive et al., 2014); kinetically independent thermal
107 indicators such as authigenic clay mineral assemblages and dispersed organic matter that furnish
108 a maximum paleotemperature of the material examined (Hartkopf-Fröder et al., 2015); K-Ar
109 dating of diagenetic illite that provides the time the mineral precipitated (Meunier et al., 2004);
110 and apatite and zircon fission track analyses that reveal both the time and temperature of
111 formation of the mineral analyzed (Reiners and Ehlers , 2005).

112 This paper presents the results of an integrated thermal history analysis of the Dezadeash
113 Formation, including: structural fabrics observed in outcrop; petrographic examination of thin

114 sections of sandstones, mudstone, hemipelagite, and volcanoclastic beds; X-ray diffraction of
115 sandstone, mudstone, hemipelagite, and volcanoclastic beds, including whole-rock, clay
116 speciation, and illite Kübler index and chlorite Δ index "crystallinity" determinations;
117 microfossil analysis of mudstone and hemipelagite beds for palynomorphs and limestone clasts
118 for conodonts; and pyrolysis maturation analysis of mudstones and hemipelagites. Published
119 thermochronometric data from the Dezadeash Formation are also incorporated. In addition, the
120 paper presents the results of a quantitative subsidence analysis, including sediment decompaction
121 and backstripping. The primary aim of this contribution is to characterize the post-depositional
122 alteration of the Dezadeash Formation in an attempt to determine the maximum temperature and
123 pressure reached by the strata. The goal is to constrain the burial history of the Nutzotin-
124 Dezadeash basin, which may have implications regarding the tectonic evolution of the Northern
125 Cordillera of Alaska and Yukon with respect to basin type and tectonic setting.

126

127 **2. Geologic Setting**

128 The northern Cordillera and adjoining areas are an amalgamation of allochthonous
129 composite terranes, superimposed magmatic arcs, and exhumed sedimentary flysch basins, all
130 variably offset by lithospheric-scale strike-slip faults. Geologic elements relevant to this study
131 include: the Yukon, Wrangellia, and South Margin composite terranes; the Chitina, Chisana, and
132 Kluane arcs; the Gravina, Dezadeash, Nutzotin, Wrangell, Blanchard River, and Kluane Schist
133 basins; and the Border Ranges, Fairweather, Denali, and Coast-Tatshenshini faults.

134

135 **2.1. Composite terranes**

136 **2.1.1. Yukon composite terrane**

137 The Yukon composite terrane (YCT) refers to the polymetamorphosed and polydeformed
138 Yukon-Tanana, Slide Mountain, Cache Creek, Quesnellia, and Stikinia terranes (Fig. 1)
139 (Wheeler and McFeely, 1991; Monger, 2014). The YCT includes a substrate of Proterozoic to
140 Paleozoic metasedimentary and mafic meta-igneous rocks, overlain by an assemblage of
141 Devonian-Mississippian arc-related volcanic and sedimentary rocks (Plafker and Berg, 1994;
142 Nelson et al., 2013). The YCT was rifted from the ancient margin of North America in the
143 middle Paleozoic, resulting in the formation of the oceanic Slide Mountain terrane, and
144 subsequently re-attached to North America in the latest Paleozoic (Nelson et al., 2013). The
145 Cache Creek terrane is a subduction-related assemblage that is flanked by late Paleozoic to early
146 Mesozoic volcanic arc rocks belonging to Quesnellia and Stikinia (Monger, 2014). Final
147 accretion of the YCT to the western margin of Laurentia occurred in the mid-Cretaceous
148 (Monger et al., 1982; Monger and Journeay, 1994; Nelson et al., 2013).

149

150 2.1.2. Wrangellia composite terrane

151 The Wrangellia composite terrane (WCT) is an amalgamation of three
152 tectonostratigraphic terranes referred to as the Alexander, Wrangellia, and Peninsular terranes
153 (Fig. 1) (Plafker and Berg, 1994). The Alexander terrane includes a basement of Neoproterozoic
154 to early Paleozoic island arc-related volcanic and sedimentary rocks (Nokleberg et al., 1994;
155 Beranek et al., 2012), and also late Paleozoic island arc-related volcanic and sedimentary rocks.
156 The Wrangellia terrane consists mainly of late Paleozoic to early Mesozoic island arc-related
157 volcanic and sedimentary rocks. The Peninsular terrane consists of an assemblage of Mesozoic
158 arc-related volcanic rocks (Nokleberg et al., 1994). The three terranes represent successively
159 higher structural and stratigraphic successions from southeast to northwest (Nokleberg et al.,

160 1994). The Alexander and Wrangellia terranes were contiguous during the late Paleozoic, based
161 on Pennsylvanian-age plutons that intrude both terranes (Gardner et al., 1988). The Peninsular
162 terrane collided in Late Jurassic time with either the western margin of Laurasia (the Yukon
163 composite terrane), or the combined Alexander-Wrangellia terrane (Clift et al., 2005; Beranek et
164 al., 2014). The WCT, interpreted as part of an obliquely converging oceanic plateau (Greene et
165 al., 2010), was emplaced against the margin of Laurasia during the mid-Jurassic to mid-
166 Cretaceous (Monger et al., 1982; McClelland et al., 1992a; Nokleberg et al., 1994).

167

168 2.1.3. South Margin composite terrane

169 The South Margin composite terrane (SMCT) includes the Mesozoic Chugach terrane
170 and the Cenozoic Prince William terrane (Fig. 1) (Trop and Ridgway, 2007). These two terranes
171 comprise metamorphic rocks and offscraped oceanic sedimentary and volcanic rocks interpreted
172 as a subduction complex (Plafker et al., 1994). The SMCT is in contact with the WCT along the
173 Border Ranges fault (Fig. 1). The Border Ranges fault, inferred as an Early Jurassic to Late
174 Cretaceous subduction zone megathrust, is thought record large magnitude dextral slip (possibly
175 > 500 km) since Late Cretaceous-Paleogene time (Pavlis and Roeske, 2007).

176 The Southern Margin composite terrane is flanked to the south by the Yakutat terrane.
177 (Fig. 1). The Yakutat terrane is interpreted as a displaced fragment of the western North America
178 continental margin that was transported ~600 km along the Fairweather fault (Fig. 1) (Plafker
179 and Berg, 1994). Subduction of the Yakutat terrane beneath North America began ~30 Ma ago
180 and is ongoing; the subduction is partly responsible for major uplift of the St. Elias Mountains
181 syntaxis and exhumation of the Dezadeash Formation (Plafker and Berg, 1994; Enkelmann et al.,
182 2017; McDermott et al., 2019).

183

184 **2.2. Arcs and Basins**

185 The number of magmatic arcs, their polarity, and the tectonic setting of contemporaneous
186 sedimentary basins in the northern Cordillera is controvertible (Saleeby, 1983; Hildebrand, 2013;
187 Shepard et al., 2013; Gehrels et al., 2017; Lowey, 2017; Sigloch and Mihalynuk, 2017; Pavlis et
188 al., 2019; Chen et al., 2019; Zhang et al., 2019; Fu et al., 2020). Therefore, this section presents a
189 detailed description of these Jurassic-Cretaceous rocks.

190

191 **2.2.1. Late Jurassic-Early Cretaceous**

192 Manifestations of the Chitina arc (~160–140 Ma; Plafker et al., 1989; Nokleberg et al.,
193 1994; Roeske et al., 1991, 2003) are scattered from southeastern Alaska, through southwestern
194 Yukon, and into southcentral Alaska (Fig. 1) (Nokleberg et al., 1994). In southeastern Alaska,
195 metavolcanic rocks interpreted as pillowed to massive basaltic to andesitic lava flows, basaltic
196 breccia, and crystal-rich volcanoclastics dominate the lower part of the Gravina sequence (Fig. 2)
197 (Rubin and Saleeby, 1991). Minor amounts of metasedimentary rocks (mainly conglomerate and
198 mudstone) are also present and are considered Late Jurassic in age based on the bivalve *Buchia*
199 (Rubin and Saleeby, 1991). Major, trace and rare earth element geochemistry indicates that the
200 volcanic rocks resemble modern island arc tholeiites (Rubin and Saleeby, 1991). According to
201 Rubin and Saleeby (1991), the lower unit unconformably overlies the Alexander terrane and has
202 a structural thickness of ~1300 m. The lower volcanic unit is positionally overlain by an upper
203 metasedimentary unit comprising tuffaceous turbidites, mudstone-sandstone turbidites, and
204 conglomerate (Fig. 2). The upper unit has a structural thickness of ~900 m and contains granitic
205 clasts with U-Pb zircon ages ranging from 154–158 Ma (Rubin and Saleeby, 1991). Rubin and

206 Saleeby (1991) interpreted the lower unit as lava flows shed from the flanks of submarine
207 volcanoes and the upper unit as submarine fans deposited adjacent to dissected volcanic centers;
208 they concluded that the Gravina sequence represents the remnants of an island arc with a
209 contemporaneous sedimentary cover that accumulated on the eastern (inboard) edge of the
210 Alexander terrane. In contrast, Yokelson et al. (2015) proposed that, on the basis of U-Pb and Hf
211 isotope analyses of detrital zircons, the Gravina sequence represents an “eastern facies” which
212 accumulated along the western margin of the YCT. The Gravina sequence is structurally overlain
213 by the YCT and experienced greenschist to amphibolite facies metamorphism (Rubin and
214 Saleeby, 1992).

215 Volcanic and volcanoclastic rocks derived from the Chitina arc occur also at the base of
216 the Gravina belt in southeastern Alaska (Fig. 1 and 2). The volcanic and volcanoclastic rocks are
217 inferred to be Late Jurassic in age and to depositionally overlie the Alexander terrane
218 (McClelland et al., 1991). McClelland et al. (1991) reported that the volcanic rocks consist
219 mainly of basaltic to andesitic flows that are geochemically similar to volcanic rocks at the base
220 of the Gravina sequence. Lesser amounts of pyroclastic breccias, fine-grained volcanoclastics,
221 and sandstone-mudstone turbidites are also present (McClelland et al., 1991). The basal volcanic
222 rocks of the Gravina belt are locally overlain conformably by the Seymour Canal Formation
223 (Fig. 2) (Gehrels, 2000). The Seymour Canal Formation is ~1800 m thick succession dominated
224 by sandstone and mudstone turbidites with minor amounts of conglomerate (Lanthram et al.,
225 1965; McClelland et al., 1991; Cohen, 1992; Gehrels, 2000). Sandstones contain detrital biotite
226 that reveal $^{40}\text{Ar}/^{39}\text{Ar}$ ages of ~159–129 Ma (Cohen et al., 1995), and the strata are considered to
227 be Late Jurassic (Oxfordian) to Early Cretaceous (Albian) in age based on the bivalve *Buchia*
228 (Lanthram et al., 1965; Gehrels, 2000). The Seymour Canal Formation also locally overlies

229 unconformably the Alexander terrane (Cohen, 1992; Cohen and Lundberg, 1993). The Seymour
230 Canal Formation is interpreted as upper and middle submarine fan deposits sourced from the
231 WCT (Cohen, 1992; Gehrels, 2000; Gehrels et al., 2009). Haeussler (1992) noted that sandstones
232 from the unit display prehnite-pumpellyite facies metamorphism, whereas associated volcanic
233 rocks display greenschist to amphibolite facies metamorphism. Cohen and Lundberg (1993)
234 observed that the Seymour Canal Formation is regionally metamorphosed to zeolite, prehnite-
235 pumpellyite, and lower-greenschist facies in the north, increasing to greenschist facies in the
236 south. The Seymour Canal Formation is conformably overlain by the Douglas Island Volcanics
237 and Brothers Volcanics (Lanthram et al., 1965), correlative with the Chisana arc describe later.

238 Volcaniclastic rocks derived from the Chitina arc occur in the Dezadeash Formation in
239 southwest Yukon (Fig. 1 and 2), the focus of this study. Three thick volcaniclastic beds
240 (measuring 9.7, 8.5 and 1.5 m thick from the lowest to highest bed) consisting of fine-to
241 medium-grained vitric to crystal tuff are interpreted as resedimented syn-eruptive volcaniclastic
242 gravity flow deposits (Lowey, 2011). A U-Pb zircon age of 149.4 ± 0.3 Ma indicates they are
243 contemporaneous with the Chitina arc, and a variety of tectonic discriminant diagrams show they
244 have a continental arc signature, which Lowey (2011) attributed to the WCT proxying for
245 continental crust.

246 The Dezadeash Formation is an approximately 3000 m thick succession of thin- to thick-
247 bedded turbidites and massive sandstone with minor amounts of conglomeratic mudstone
248 containing limestone clasts up to ~10 m in exposed longest dimensions, volcaniclastic rocks, and
249 hemipelagic lime mudstone (Eisbacher, 1976; Lowey, 1992, 2007). Based on detailed lithofacies
250 analysis, the Dezadeash Formation represents mainly the middle and lower subdivisions of a

251 point-source, mud/sand-rich submarine fan (Lowey, 2007) that was derived from the WCT and
252 Chitina arc (Lowey, 2019).

253 The Dezadeash Formation is Late Jurassic (Oxfordian) to Early Cretaceous (Valanginian)
254 in age based on collections of the bivalve *Buchia* (Eisbacher, 1976), and uncomfortably overlies
255 the Alexander and Wrangellia terranes, specifically Triassic volcanic, volcanoclastic, and
256 carbonate rocks belonging to the Nikolai Formation, McCarthy Formation, and Chitistone and
257 Nisina Limestone (Dodds and Campbell, 1992a). The Dezadeash Formation is overlain
258 unconformably by ~1000 m of unmetamorphosed nonmarine Paleogene clastic and
259 volcanoclastic rocks of the Amphitheater Formation (Eisbacher, 1976; Ridgway et al., 1995).

260 Eisbacher (1976) identified two phases of folding in the Dezadeash Formation: the oldest
261 folds (F_1) trend northerly, are asymmetric or overturned to the east, and locally change laterally
262 into thrust faults; the youngest folds (F_2) trend west-northwesterly and are open. The oldest folds
263 are crosscut by the Shorty Creek pluton that reveals a K-Ar age of ~106 Ma (Dodds and
264 Campbell, 1988). Eisbacher (1976) attributed the oldest folds to movement on a “tectonic slope”
265 because the trend of the folds is similar to the trend of penecontemporaneous slump folds in the
266 Dezadeash Formation; he ascribed the youngest folds to westward directed thrusting of the
267 Kluane Schist over the Dezadeash Formation and movement on the Denali fault zone. Both the
268 Kluane Schist and Denali fault are described later.

269 Metamorphism of the Dezadeash Formation is poorly documented. Sturrock (1975)
270 concluded that strata had undergone prehnite-pumpellyite facies burial metamorphism, but this
271 was based on the examination of a single thin section from the contact aureole of the Pyroxenite
272 Creek complex (Cretaceous). And Dodds and Campbell (1992b) noted in the legend of the
273 geologic map of the Dezadeash area that the Dezadeash Formation was “unmetamorphosed to

274 regionally metamorphosed up to subgreenschist facies (laumontite-prehnite-quartz)", but
275 provided no additional information on how this determination was reached.

276 The Dezadeash Formation has also been utilized in low-temperature thermochronometric
277 investigations. Specifically, two samples by Enkelmann et al. (2017) and possibly one sample by
278 McDermott et al. (2019) from the St. Elias Mountains syntaxis in southwest Yukon (Fig. 3), are
279 summarized in Table 1. The thermochronometric investigations reveal multiple episodes of
280 exhumation and landscape evolution, which McDermott et al. (2019) attribute to rapid cooling at
281 ~95–75 Ma due to accretion of the WCT to the YCT, slow cooling during ~75–30 Ma caused by
282 relief degradation, and renewed rapid cooling beginning ~30 Ma and continuing to the present,
283 attributed to flat-slab subduction of the Yakutat terrane and strike-slip displacement on the
284 Denali fault zone.

285 Volcaniclastic rocks likely derived from the Chitina arc have been reported from the
286 Nutzotin Mountains sequence in southcentral Alaska (Fig. 1 and 2), but the volcaniclastic rocks
287 have not been described in detail, nor have they been radiometrically dated (Richter, 1976). The
288 Nutzotin Mountains sequence is up to 3000 m thick and consists mainly of thin-bedded turbidites
289 with minor amounts of massive sandstone, conglomeratic mudstone (containing limestone clasts
290 up to ~10 m exposed longest dimensions), and hemipelagite beds (Berg et al., 1972; Richter,
291 1976; Kozinski, 1985; Manuszak et al., 2007). The strata are interpreted as westerly sourced,
292 distal to proximal submarine fan deposits that grade upward into shelf deposits (Kozinski, 1985;
293 Manuszak et al., 2007). The Nutzotin Mountains sequence is Late Jurassic (Tithonian) to Early
294 Cretaceous (Valanginian) in age and unconformably overlies the Wrangellia terrane (Manuszak
295 and Ridgway, 2000). The strata are deformed by north-dipping thrust faults and overturned folds

296 that are crosscut by 117–105 Ma plutons, and is conformably overlain by the mainly volcanic
297 Chisana Formation (Manuszak et al., 2007).

298 Metamorphism of the Nutzotin Mountains sequence is also poorly documented. Kozinski,
299 (1985) measured two stratigraphic sections in the northeastern part of the Nutzotin Mountains
300 sequence that are separated by ~6 km. Observing prehnite in a thin section from one of the
301 measured sequences and discovering pumpellyite in a thin section from the second measured
302 sequence, Kozinski (1985) concluded that the Nutzotin Mountains sequence had undergone
303 prehnite-pumpellyite grade metamorphism. And Dusel-Bacon et al. (1993) indicated in the
304 explanation of a map of regionally metamorphosed rocks of Alaska that the Nutzotin Mountains
305 sequence was “unmetamorphosed”.

306 Eisbacher (1976) proposed that the Dezadeash Formation and Nutzotin Mountains
307 sequence represent the same strata that was dismembered and displaced by the Denali fault
308 system (Eisbacher, 1976). The Denali fault system is one of the main strike-slip faults in the
309 Northern Cordillera, along which ~370 km of dextral slip occurred since the Early Cretaceous
310 (Clague, 1979; Lowey, 1998, and references therein). Sedimentologic and stratigraphic studies
311 by Kozinski (1985), Manuszak (2000), and Manuszak and Ridgway (2000) on the Nutzotin
312 Mountains sequence, and Lowey (2019) on the Dezadeash Formation corroborates this
313 interpretation.

314 Volcanic rocks of the Chitina arc likely also occur in the Wrangell Mountains basin of
315 south-central Alaska (Fig. 1 and 2). The Wrangell Mountains basin is comprised of three
316 depositional sequences each bounded by unconformities: the lower sequence consists of ~1700
317 m of mudstone, sandstone, and conglomerate (i.e., Root Glacier Formations and Kotsina
318 Conglomerate) that is Late Jurassic (Kimmeridgian-Tithonian) in age; the middle sequence

319 consists of ~300 m of calcareous sandstone and mudstone (i.e., Berg Creek and Kuskulana
320 formations) that is Early Cretaceous (Hauterivian-Barremian) in age; and the upper sequence
321 consists ~3575 m of sandstone, conglomerate, and mudstone, with minor porcellanite and rare
322 tuff (i.e., Kennicott, Moonshine Creek, Schultze, Chititu, and MacColl Ridge formations) that is
323 Early to Late Cretaceous (Albian-Campanian) in age (MacKevitt, 1971; Trop et al., 2002). The
324 lower sequence rests unconformably on the WCT, and the upper sequence is unconformably
325 overlain by siliciclastic rocks (Fredrika Formation) and volcanic rocks (Wrangell Lava) that are
326 Miocene to Pliocene in age (Trop et al., 2002). In the lower sequence, thin bedded aphanitic
327 flows and vitric tuffs are interbedded with mudstone and sandstone of the ~1100 m thick Root
328 Glacier Formation (Trop et al., 2002). The volcanic and volcanoclastic rocks have not been
329 described in detail, nor have they been radiometrically dated. The Root Glacier Formation is
330 Early Jurassic (Oxfordian-Tithonian) in age, and is interpreted as submarine slope and fan
331 deposits sourced from the WCT (Trop and Ridgway, 2007). Strata appear to be
332 unmetamorphosed (MacKevitt, 1971; Trop et al., 2002).

333 Plutonic rocks interpreted as the roots of the Chitina arc extend from southeastern Alaska,
334 through southwestern Yukon and into southcentral Alaska. The plutonic rocks occur as elongate
335 batholithic complexes to smaller single and multiple phase plutons that are widespread, and
336 generally decrease in size, abundance, mafic composition and possibly depth of emplacement
337 from west to east (Dodds and Campbell, 1988; Hudson, 1983; Plafker et al., 1989). The
338 intrusions are commonly parallel to regional trends, exhibit abrupt to gradational boundaries, and
339 are locally foliated (Dodds and Campbell, 1988; Hudson, 1983). The rocks are calc-alkaline in
340 composition and consist mainly of quartz diorite, tonalite and granodiorite ranging from Late
341 Jurassic to Early Cretaceous in age (~160–130 Ma) (Dodds and Campbell, 1988; Hudson, 1983;

342 Miller, 1994; Plafker et al., 1989; Roeske et al., 1991). The batholiths and plutons include the
343 Tonsina–Chichagof belt of Hudson (1983) and the Saint Elias plutonic suite of Dodds and
344 Campbell (1988). They correspond to the 160–140 Ma period of magmatic flux summarized by
345 Gehrels et al. (2009) for the Northern Cordillera. The Chitina arc is restricted to the Wrangell
346 and Alexander terranes of the WCT (Fig. 1), and there are no conclusive data to constrain the
347 polarity of subduction of the arc (Plafker et al., 1989; Monger and Price, 2002).

348 Trop and Ridgway (2007) proposed that the Chitina arc represents the eastern extension
349 of the Talkeetna arc ('T' in Fig. 1). However, volcanism associated with the Talkeetna arc ended
350 during Early to Middle Jurassic time (~180–170 Ma) (Rioux et al., 2007), before initiation of
351 Chitina arc volcanism in Late Jurassic time (~150 Ma). In addition, the Talkeetna arc is
352 interpreted as an archetypal example of an intraoceanic arc and is mainly restricted to the
353 Peninsular terrane (Rioux et al., 2007), whereas the Chitina arc displays continental margin arc
354 signatures and is confined to the Wrangellia and Alexander terranes (Lowey, 2011). Polarity of
355 the Talkeetna arc is debatable (Reed et al., 1983; Trop and Ridgway, 2007)

356

357 2.2.2. Early Cretaceous

358 The Chisana arc (~120–105 Ma; Short et al, 2005; Falkowski and Enkelman, 2016) is
359 represented by the Douglas Island Volcanics and Brothers Volcanics in southeastern Alaska, and
360 the Chisana Formation in southcentral Alaska (Fig. 1 and 2). In southeastern Alaska, the Douglas
361 Island Volcanics and Brothers Volcanics conformably overly the Gravina belt (specifically the
362 Seymour Canal Formation) (Lanthram et al., 1965). The volcanic units are dominated by augite
363 porphyritic basalt characterized as breccia and pillowed flows, and minor amounts of
364 volcanoclastics and mudstone-sandstone turbidites (Lanthram et al., 1965; Gehrels, 2000).

365 Geochemically, the volcanic rocks are calc-alkaline and related to a volcanic arc and subduction
366 zone setting (Stowell et al., 2000). The Douglas Island/Brothers Volcanics are ~300–600 m thick
367 and are considered Early Cretaceous in age (mainly Hauterivian to possibly Albian) (Lanthram et
368 al., 1965; Gehrels, 2000). The Douglas Island Volcanics experienced prehnite-pumpellyite to
369 greenschist facies metamorphism with pressure-temperature (P-T) estimated to have reached 2–
370 7.5 kbars and 325 °C (Himmelberg et al., 1995). The Douglas Island Volcanics are conformably
371 overlain by sandstone, mudstone, and conglomerate assigned to the Treadwell Formation that has
372 a detrital zircon inferred maximum depositional age of ~105 Ma (Gehrels, 2000).

373 The Gravina belt (i.e., Seymour Canal Formation, Douglas Island and Brothers
374 Volcanics, and Treadwell Formation) is structurally overlain by the YCT to the east (Fig. 1).
375 Stowell and Crawford (2000) summarized the metamorphic history of the Gravina belt and
376 recognized that the earliest metamorphic event as regional in extent (i.e., M_1^R) and characterized
377 by low- to moderate-pressure (2–6 kbar) and low temperature (~150–275 °C). In contrast,
378 McClelland and Mattinson (2000) postulated that parts of the belt were underthrust to deep
379 crustal levels of 25–30 km.

380 The Chisana Formation (Fig. 2) gradationally overlies the Nutzotin Mountains sequence
381 in southcentral Alaska. The Chisana Formation includes a lower unit of mainly basaltic and
382 andesitic flows and minor amounts of sandstone, mudstone, and volcaniclastic rocks up to ~1100
383 m thick, and an upper unit of interlayered volcanic-lithic breccia, basaltic-andesite flows,
384 conglomerate, and mudstone, and volcaniclastic rocks up to ~2500 m thick (Berg et al., 1972;
385 Richter, 1976; Barker, 1987; Manselle et al., 2020). The formation is Late Cretaceous in age
386 (Aptian-Albian) based on $^{40}\text{Ar}/^{39}\text{Ar}$ ages of ~116–113 Ma (Short et al., 2005). The unit is
387 interpreted to have been deposited proximal to volcanic vents on subaqueous (lower unit) and

388 subaerial (upper unit) slopes of the contemporaneous proto-continental, or intraoceanic Chisana
389 arc (Short et al., 2005; Manselle et al., 2020). The Chisana Formation appears to have been
390 subject to unspecified subgreenschist facies metamorphism (Berg et al., 1972; Manselle et al.,
391 2020), and is unconformably overlain by the unmetamorphosed Beaver Lake Formation, a ~90 m
392 thick assemblage of Early to Late Cretaceous conglomerate, tuff and coal deposited in fluvial
393 systems (Manselle et al., 2020).

394 Other Early Cretaceous flysch basins contemporaneous with the Chisana arc include the
395 Wrangell Mountain basin in south-central Alaska and the Blanchard River assemblage in
396 southwestern Yukon (Fig.1 and 2). In the Wrangell Mountains basin, calcareous sandstone and
397 mudstone of the Berg Creek and Kuskulana formations are Early Cretaceous (Hauterivian-
398 Barremian, 132-121 Ma) in age and restricted to the western half of the basin (Trop et al., 2002).
399 The Blanchard River assemblage consists mainly of interlayered quartz-biotite schist and quartz-
400 biotite psammitic schist that grades eastward into proto-gneiss and paragneiss before becoming
401 engulfed by the Ruby Range batholith (~64–54 Ma) of the Coast Plutonic Complex (Vice, 2017).
402 According to Vice (2017), the Blanchard River assemblage is ~5000–6000 m thick with a
403 detrital zircon based maximum depositional age of 130–125 Ma. The zircons are inconclusive
404 with regards to provenance and suggest derivation from either the YCT, the WCT, or both, and it
405 is unknown if the Blanchard River assemblage was deposited on WCT or YCT crust (Vice,
406 2017). The Blanchard river assemblage is structurally overlain by the YCT, and reached
407 amphibolite facies metamorphism with P-T conditions estimated to have been ~6.5 kbars (~24
408 km depth) and ~640°C (Vice, 2017).

409 Plutonic rocks interpreted as the roots of the Chisana arc extend from southeastern
410 Alaska, through southwestern Yukon and into southcentral Alaska. The plutonic rocks occur as

411 elongate batholithic complexes and plutons of granodiorite, quartz diorite, diorite, and rarer
412 quartz monzonite (Dodds and Campbell, 1988). The rocks are calc-alkaline in composition and
413 are Early Cretaceous in age (~117–106 Ma) (Dodds and Campbell, 1988; Hudson, 1983; Miller,
414 1994; Plafker et al., 1989; Roeske et al., 1991). The batholiths and plutons include the Nutzotin-
415 Chichagof belt (120–105 Ma) belt of Hudson (1983) and the Muir-Chichagof belt of Brew and
416 Morrell (1983) in Alaska, and the Kluane Ranges plutonic suite of Dodds and Campbell (1988)
417 in southwest Yukon. The Shorty Creek pluton of the Kluane Ranges plutonic suite intrudes the
418 Dezadeash Formation (Fig. 2) and has a K-Ar age of ~106 Ma (Dodds and Campbell, 1988).

419 Roots of the Chisana arc are also preserved as Alaskan-type ultramafic complexes,
420 specifically the Klukwan-Duke belt in southeast Alaska (Brew and Morrell, 1983), and the
421 Pyroxenite Creek complex in southwestern Yukon (Fig. 3) (Dodds and Campbell, 1988). The
422 Pyroxenite Creek complex intrudes the Dezadeash Formation and has K-Ar ages of ~128–109
423 Ma and a Rb-Sr age of ~116 Ma (Rb-Sr) (Sturrock et al., 1980). According to Sturrock (1975),
424 the intrusion resulted in a 30 m wide contact metamorphic aureole of albite-epidote hornfels
425 facies in the Dezadeash Formation.

426 The Chisana arc is restricted to the Wrangell and Alexander terranes of the WCT (Fig.1),
427 and is included in of the 120–78 Ma period of magmatic flux summarized by Gehrels et al.
428 (2009) for the Northern Cordillera. There are no conclusive data to constrain the polarity of
429 subduction of the arc, although subduction is generally assumed to be northeastward (Plafker et
430 al., 1989; Monger and Price, 2002)

431

432

433

434 2.2.3. Late Cretaceous-Paleogene (Eocene)

435 Volcaniclastic rocks likely derived from the Kluane arc (~85–45 Ma, Nokleberg et al.,
436 2000; Amato et al., 2007) also occur in the Wrangell Mountain basin in southcentral Alaska (Fig.
437 1 and 2). In the uppermost sequence, tuff is interbedded with ~1150 m of sandstone,
438 conglomerate, and mudstone of the MacColl Ridge Formation (Trop et al., 2002). Vitric tuff
439 beds measuring 10–100 cm thick reveal $^{40}\text{Ar}/^{39}\text{Ar}$ ages of ~80–76 Ma (Stamatakos et al., 2001),
440 contemporaneous with the Kluane arc. The MacColl Ridge Formation is Late Cretaceous
441 (Campanian) in age, and is interpreted as submarine fan deposits sourced from the WCT (Trop
442 and Ridgway, 2007). Strata appear to be unmetamorphosed (MacKevett, 1971; Trop et al.,
443 2002).

444 Other Early Cretaceous basins contemporaneous with the Kluane arc include the Kluane
445 Schist in southwestern Yukon (Fig.1 and 2). The Kluane Schist is a sequence of graphitic mica–
446 chlorite–quartz schist and gneiss with a structural thickness of ~12,000 m that contains
447 interfoliated bodies of serpentinized dunite up to 1.5×15 km in exposed dimensions (Mezger et
448 al., 2001a). Zircon geochronology indicates the protolith of the Kluane Schist is Late Cretaceous
449 in age (<94 Ma) (Stanley, 2012), although Tempelman-Kluit (1976) reports a K-Ar biotite age of
450 140 Ma. It is not known if the Kluane Schist was sourced from the WCT, the YCT, or both, and
451 whether the unit was deposited on WCT or YCT crust (Mezger et al., 2001a; Canil et al. (2015)).
452 The Kluane Schist is structurally overlain by the YCT and was subject to greenschist to
453 amphibolite facies metamorphism with P-T estimated to have been 7 kbar (~24 km depth) and
454 500 °C (Tempelman-Kluit, 1976; Mezger et al., 2001a).

455 Plutonic rocks interpreted as the roots of the Kluane arc form part of the extensive Coast
456 Plutonic Complex, or Coast Mountains Batholith (~175–45 Ma, Armstrong, 1988; Gehrels et al.,

457 2009) that extends for much of the length of the Northern Cordillera and into east-central Alaska
458 (Fig. 1). The Coast Plutonic Complex is inferred to have formed immediately after accretion of
459 the WCT with the YCT (i.e., the ancient margin of western North America) and the intrusive
460 complex obscures the “Shakwak” suture between these two composite terranes (Eisbacher, 1985;
461 Amato et al., 2007). The roots of the Kluane arc are preserved mainly as calc-alkaline diorite,
462 quartz diorite, granodiorite and locally monzonite, and syenite plutons that intrude both the WCT
463 and the YCT (Plafker et al., 1989). The Kluane arc is interpreted as part of a continental-margin
464 arc that was active during the Late Cretaceous and Paleogene (Plafker et al., 1989; Nokleberg et
465 al., 1994; Plafker and Berg, 1994; Monger and Nokleberg, 1996). The Kluane arc overlaps the
466 periods of high magnetic flux of 120–78 Ma and 55–48 Ma and the magnetic lull of 78–55 Ma of
467 Gehrels et al. (2009). There are no conclusive data to constrain the polarity of subduction of the
468 arc, although subduction is generally assumed to be northeastward (Plafker et al., 1989; Monger
469 and Price, 2002).

470 Intimately associated with the Coast Plutonic Complex is the Coast shear zone (Fig.1).
471 The Coast shear zone, as defined by Andronicos et al. (1999) and Chardon et al. (1999), consists
472 of the Great Tonalite Sill (located along the western margin of the Coast Mountains Complex)
473 and related flanking structures extending more than 1000 km from southern British Columbia
474 into southeastern Alaska (Fig. 1). Displacement across the Coast shear zone is dominantly east-
475 over-west and this occurred in mid-Cretaceous time (Brew, 1997; Brew and Ford, 1998; Stowell
476 and Hooper, 1990; McClelland et al., 1992b; Andronicos et al., 1999; Chardon et al., 1999); the
477 Great Tonalite Sill is interpreted as a synkinematic sill intruding the shear zone (Stowell and
478 Hooper, 1990; McClelland et al., 1992; Ingram and Hutton, 1994; Brew and Ford, 1998; Klepeis
479 et al., 1998; Andronicos et al., 1999; Chardon et al., 1999). McClelland and Mattinson (2000)

480 proposed that the Coast shear zone may have originated as a lithospheric strike-slip fault that
481 accommodated 300-600 km dextral translation.

482 Stowell and Crawford (2000) determined that emplacement of Coast Plutonic Complex
483 sill plutons along the Coast shear zone next to the Gravina belt resulted in contact metamorphism
484 (M_4^C) characterized by sillimanite-zone assemblages indicating moderate pressure (~6 kbar) and
485 high temperature (700 °C). Lowey (2000) extended the Coast Shear zone into southwest Yukon
486 as part of the Tatshenshini shear zone (Fig. 1). The Tatshenshini shear zone is characterized by
487 protomylonitic and mylonitic turbidites of the Dezadeash Formation in the footwall and
488 protomylonitic granodiorite of the Ruby Range Batholith (part of the Coast Plutonic Complex) in
489 the hangingwall (Lowey, 2000). Kinematic indicators from the Dezadeash Formation and Ruby
490 Range Batholith record a top-to-the southwest sense of shear. A whole rock K-Ar age of 60.2
491 ± 1.9 Ma obtained from mylonite indicates that the main phase of shearing took place no later
492 than ~60 Ma ago. Initial emplacement of the Ruby Range Batholith along the Tatshenshini shear
493 zone appears to have occurred ~75–68 Ma ago. The intrusion resulted in contact metamorphism
494 of the Dezadeash Formation that is characterized by andalusite-chiastolite poikiloblastic phyllite
495 with a K-Ar age of 68.2 ± 1.8 Ma (Lowey, 2000); the intrusion was apparently shallow and
496 reached ~490 °C (Mezger, 1997).

497 Stowell et al. (2000) concluded that metamorphism and emplacement of Coast Plutonic
498 Complex in the Gravina belt resulted in an average geothermal gradient of < 20 °C/km at ~100
499 Ma, and likely closer to <14 °C/km (Stowell and Crawford, 2000). Stowell and Crawford (2000)
500 suggested that these inferred geothermal gradients are not compatible with a rift setting for the
501 Gravina belt because such a setting would be characterized by a higher heat flow and a higher
502 temperature of metamorphism.

503

504 **3. Methods**

505 This study is based on 16,335 m of measured strata from 75 sections throughout the
506 Dezadeash Formation (Fig. 3 and Supplementary Table S1). In addition to collecting standard
507 bed-by-bed sedimentological measurements (i.e., bed thickness, lithology, grain size, and
508 sedimentary structures), data was also collected pertaining to secondary deformation features
509 (i.e., cleavage, folds, joints, and veins). Approximately 200 samples were collected from these
510 sections, and a subset of samples from the 200 initially collected were selected for analysis.

511 Seventy-two samples were selected for thin-section analysis, including 35 sandstone, 4
512 coquina, 11 mudstone, 7 hemipelagite, and 15 tuff samples. Standard thin sections, half of which
513 were impregnated with blue epoxy, and standard off-cuts, all of which were stained for
514 potassium feldspars, were prepared by Vancouver Petrographics Ltd., Langley, British
515 Columbia. The thin-sections were examined by transmitted light microscopy with a standard
516 petrographic microscope.

517 Eight samples of were selected for processing for palynomorphs (spores and pollen). The
518 samples were prepared following standard extraction techniques (Traverse, 1988), including
519 disaggregation and washing, HCl and HF acid digestion, oxidation with Schulze's solution, and
520 separation of the organic fraction from the heavier residue with ZnCl₂. The organic fraction was
521 mounted on glass slides with liquid bioplastic and examined with a transmitted light microscope
522 using oil immersion at 400x and 1000x magnification. The degree of maturation of the organic
523 fraction, basically the thermally induced, systematic and irreversible changes in the color of the
524 organic material, was determined by visual comparison with the Thermal Alteration Index of
525 Staplin (1969). The Thermal Alteration Index (TAI) is a semi-quantitative numerical scale from

526 1 to 5, with 1 being the lower maturity light color (i.e., colorless to light yellow) and 5 being the
527 more mature darker color (i.e., black with indications of metamorphism) (Staplin, 1969).

528 One limestone clast was selected for conodont analysis and separated using standard
529 acetic acid processing techniques by the Geological Survey of Canada, Vancouver, British
530 Columbia. A discussion of the procedure is provided by Harris and Sweet (1989) and Orchard
531 and Foster (1991). The degree of maturation of the recovered conodonts was determined by
532 visual comparison with the Conodont Alteration Index (Epstein et al., 1977). The Conodont
533 Alteration Index (CAI) is also a semi-quantitative numerical scale from 1 to 5, similar in
534 principle to the TAI, with 1 corresponding to a lower maturity light color (i.e., clear or colorless)
535 and 5 corresponding to a more mature darker color (i.e., black) (Epstein et al., 1977).

536 Two samples of sandstone and one sample each of hemipelagite and tuff were submitted
537 to AGAT Laboratories Ltd., Calgary Alberta, for quantitative X-ray diffraction analysis
538 including clay speciation, and scanning electron microscope (SEM) and energy dispersive X-ray
539 (EDX) analyses. The quantitative XRD analysis was performed on the bulk sample and clay
540 fraction. The clay fraction (less than 2 μm size) was separated from the bulk sample by
541 centrifuging. The samples were treated in an ultrasonic bath using sodium hexametaphosphate as
542 a deflocculating agent to facilitated complete disintegration of the matrix from the grains.
543 Samples were centrifuged in two phases. In the first phase, the samples were centrifuged at 600
544 rpm for 5 minutes to enable coarser particles to settle to the bottom of the tube. Clay particles
545 remaining in fluid suspension were decanted into another tube, and for the second phase
546 centrifuged at 3000 rpm for 45 minutes. The clay fraction was mounted on glass slides and
547 placed in glycol vapor bath for 24 hours in order to identify expandable clays. Weight fractions
548 were measured for both bulk and clay portions of the samples. Step-scan X-ray powder-

549 diffraction data was collected over a range of $3\text{--}80^\circ 2\theta$ with $\text{CoK}\alpha$ radiation on a standard
550 Siemens (Bruker) D5000 Bragg-Brentano diffractometer equipped with a Fe monochromator
551 foil, 0.6 mm (0.3°) divergence slit, incident- and diffracted-beam Sollers slits and a Vantec-1
552 strip detector. The long fine-focus Co X-ray tube was operated at 35 kV and 40 mA, using a
553 take-off angle of 6° . The X-ray diffractograms were analyzed using the International Center for
554 Diffraction database PDF-4 using Search-Match software by Siemens (Bruker). For SEM
555 analysis, a piece of each sample was glued on to aluminum stubs and after lightly blowing off
556 loose particles with air, the samples were coated with gold to facilitate observations and
557 photography. The gold-coated samples were examined with a scanning electron microscope to
558 highlight the distribution and morphology of minerals. EDX analysis was also carried out to
559 determine elemental compositions of minerals.

560 Two mudstone samples were submitted to Activation laboratories Ltd., Ancaster, Ontario
561 for quantitative XRD analysis including clay speciation. The quantitative XRD analysis was
562 performed on the clay fraction of the sample. A portion of each sample was pulverized, mixed
563 with corundum and packed into a standard holder. Corundum was used as an internal standard.
564 For the clay speciation analysis, a portion of each sample was dispersed in distilled water and
565 clay minerals in the $< 2\ \mu\text{m}$ size fraction separated by gravity settling of particles in suspension.
566 Oriented slides of the $< 2\ \mu\text{m}$ size fraction were prepared by placing a portion of the suspension
567 onto a glass slide. The oriented slides were analyzed air-dried, after treatment with ethylene
568 glycol and after heating at $375\ ^\circ\text{C}$ for 1 hour. The XRD analysis was performed on a Panalytical
569 X'Pert Pro diffractometer equipped with Cu X-ray source and an X'Celerator detector and
570 operating at the following conditions: 40 kV and 40 mA; range $5\text{--}70^\circ 2\theta$ for random specimens
571 and $4\text{--}30^\circ 2\theta$ for oriented specimens; step size $0.017^\circ 2\theta$; time per step 30 sec; fixed divergence

572 slit angle 0.25° . The X'Pert HighScore plus software along with the PDF4/Minerals ICDD
573 database were used for mineral identification. The quantities of the crystalline mineral phases
574 were determined using Rietveld method. The Rietveld method is based on the calculation of the
575 full diffraction pattern from crystal structure data. The amounts of the crystalline minerals were
576 recalculated based on a known percent of corundum and the remainder to 100 % was considered
577 X-ray amorphous material. The Kübler Index (KI) was determined for illite in the $< 2 \mu\text{m}$ size
578 fraction following the procedure described by Kisch (1991): the full width of the peak at half the
579 maximum peak height (FWHM) of the 10 \AA -illite-peak was measured from the X-ray
580 diffractogram in units of $\Delta^\circ 2\theta$ $\text{CuK}\alpha$ radiation. Similarly, the Árkai Index (AI) was determined
581 for chlorite in the $< 2 \mu\text{m}$ size fraction following the method described by Árkai (1991): the
582 FWHM of the 14 \AA -chlorite-peak was measured from the X-ray diffractogram in units of $\Delta^\circ 2\theta$
583 $\text{CuK}\alpha$ radiation. Both KI and AI measure the sharpness of the diffractogram peaks; the sharpness
584 of the peaks is an indication of the crystallinity of the clay minerals, which provide an indication
585 of the extent of diagenesis and metamorphism.

586 Twenty-three samples were selected for pyrolysis analysis. The samples were submitted
587 to the Geological Survey of Canada in Calgary, Alberta, and analyzed using a Rock-Eval 6
588 Turbo (RE 6) instrument. This instrument uses a ramped temperature technique whereby a small
589 amount of sample (70–100 mg) is heated in an inert atmosphere (helium or nitrogen) and also
590 combusted with air to obtain several key geochemical parameters relating to the thermal
591 maturation of the rock. Parameters important to this study include the total organic carbon (TOC
592 wt %) in the sample, and the instrument oven temperature ($T_{\text{max}} \text{ }^\circ\text{C}$) at which the maximum
593 quantity of hydrocarbons (S_2) generated by pyrolytic degradation of kerogen in the sample
594 occurs. TOC is a measure of the utility of the analysis ($< 0.3 \text{ wt.}\%$ TOC suggests all parameters

595 have questionable significance), and T_{\max} is a measure of the thermal maturation of the sample
596 (Peters, 1986). Two calculated parameters applicable to the study are the hydrogen index (HI)
597 and the oxygen index (OI). HI is a measure of the amount of hydrogen in the sample and is
598 calculated as $HI = (S_2 \times 100 / TOC)$; and OI is a measure of the amount of oxygen in the sample and
599 is calculated as $OI = (S_3 \times 100 / TOC)$, where S_3 represents the carbon dioxide generated during
600 pyrolysis (Behar et al., 2001). Plots of HI versus OI indicate the type of kerogen present:
601 generally, high HI and low to intermediate OI values indicate lacustrine organic matter (Type I
602 or Algal/Sapropelic) and mixed marine-terrestrial organic matter (Type II or planktonic),
603 whereas low HI values and moderate to low OI values indicate woody terrestrial organic matter
604 (Type III or humic) and degraded organic matter (Type IV or inert) (Behar et al., 2001). Details
605 of the Rock-Eval apparatus, procedures and applications are available in Lafargue et al. (1998)
606 and Behar et al. (2001).

607 Quantitative subsidence analysis followed the procedures outlined by van Hite (1978),
608 Angevine et al. (1990), and Allen and Allen (2013). A one-dimensional, local isostatic Airy
609 model was assumed for the analysis, and decompaction and backstripping formulas presented in
610 Angevine et al. (1990) were used. Subsidence analysis produces a sedimentation rate for the
611 decompacted basin fill and a basin subsidence curve due solely to tectonic forces. The tectonic
612 subsidence curve depicts the subsidence history of the basin, and this can be used to evaluate the
613 veracity of the thermal history of the basin determine via mineral and organic thermal indicators.
614 The shape of the tectonic subsidence curve may also be useful in delimiting the basin type (Xie
615 and Heller, 2009; Allen and Allen, 2013).

616

617

618 3. RESULTS

619

620 3.1. Field relationships

621

622 Well-exposed outcrops of the Dezadeash Formation occur throughout the St. Elias
623 Mountains in southwestern Yukon. The majority of the outcrops are dominated by thin- to thick-
624 bedded sandstone–mudstone couplets that form packets up to ~335 m thick, and medium- to
625 thick-bedded sandstone that form amalgamated units up to ~136 m thick. Well preserved primary
626 sedimentary structures are common in these lithologies, including erosional structures (sole
627 marks and small channels), depositional structures (graded bedding, planar-stratification, and
628 cross-stratification), deformation structures (load and flame structures, convolute stratification,
629 dish and pillar structures, and slump structures), and biogenic sedimentary structures comprising
630 sparse bioturbation with few discrete trace fossils preserved in the interior of beds and on the
631 soles of beds. Detailed descriptions of these sedimentary structures and their distribution are
632 presented in Eisbacher (1976) and Lowey (1980, 2007). The pristine nature of the sedimentary
633 structures provided unambiguous evidence for the way-up of strata, and slump folds overlain by
634 undeformed beds confirm that the slumps are due to soft-sediment movement and not a later
635 tectonic deformation.

636 Superimposed on the primary sedimentary structures are a variety of secondary
637 structures. Sandstone beds in thin- to medium-bedded sandstones-mudstone couplets locally
638 display a sub-vertical parting (Fig. 4A). The parting is spaced 5–30 cm apart with a mean
639 spacing of ~10.2 cm. Parting planes are parallel to each other and can be traced from one
640 sandstone bed into several overlying or underlying sandstone beds, but they are not present in
641 thick-bedded sandstone beds. Although the parting resembles a poorly developed spaced

642 cleavage, the mean ratio of the separation of the partings to the thickness of the beds (s/l) is
643 ~ 0.95 . According to Hancock (1982), $s/l > 0.05$ belong to a joint set.

644 Mudstones are characterized by a poorly developed parting or diagenetic foliation (cf.
645 Passchier and Trouw, 1996) that is sub-parallel to bedding (Fig. 4B). The diagenetic foliation is
646 moderately to strongly developed, parallel to curvilinear, and generally spaced 3–8 mm,
647 although up to 20 mm spacing is also present. The diagenetic foliation is associated with a
648 weakly to strongly developed spaced cleavage that is at a high-angle to bedding. The cleavage
649 domains have a spacing of 5–85 mm and are smooth, occupy $< 1\%$ of the rock volume and are
650 parallel to curvilinear to each other. The intersection of the diagenetic foliation and spaced
651 cleavage results in mudstones weathering into angular, irregularly-shaped pebble-sized clasts.
652 Locally, mudstones display a moderately to well-developed spaced cleavage (Passchier and
653 Trouw, 1996). The cleavage domains have a spacing of 1–5 mm and are smooth, occupy $< 1\%$ of
654 the rock volume and are parallel to each other (Fig. 4C). The spaced cleavage is associated with
655 the oldest folds (F_1) recognized by Eisbacher (1976). The F_1 folds have amplitudes ranging from
656 10's–100's m, are asymmetric to overturned to the east, and are cross-cut by the ~ 106 Ma Shorty
657 Creek pluton (Fig. 3). The spaced cleavage appears to be roughly axial planar, and both the
658 spaced cleavage and F_1 folds trend northerly. Rarely, well developed pencil structure (Passchier
659 and Trouw, 1996) is also present in the mudstone (Fig. 4D). The pencil structure, formed by the
660 intersection of well-developed diagenetic cleavage and spaced cleavage (S_0 – S_1), trends
661 northwesterly, parallel to the F_1 folds. The pencil length varies from 49.5–164.2 mm and the
662 width ranges from 2.25–11.25 mm, with a mean shape factor (length-to-width ratio, L/W) of
663 14.5. A plot of the length and width of the pencils suggests a shortening of 9–26% (Fig. 5).

664 Hemipelagite beds display an irregular jointing spaced 10–20 cm (Fig. 4E), resulting in
665 the beds weathering into angular, block-shaped cobble-sized clasts. Volcaniclastic beds display a
666 more regular jointing spaced 20–50 cm that is intersected by a very irregular second joint set that
667 is sub-parallel to bedding (Fig. 4F). As a result, the volcaniclastic beds weather into angular,
668 irregularly-shaped boulder-sized clasts.

669 Several types of veins are locally present in the thin- to medium-bedded sandstones-
670 mudstone couplets. The more common type of veining are swarms of veins that cross-cut
671 bedding at various angles. The veins occur as differently oriented sets, often forming prominent
672 networks, with sub-parallel veins regularly spaced ~10–20 cm. The veins are ~0.5–6 cm wide
673 and syntaxial, with one or more phases of white quartz and minor amounts of calcite present that
674 impart a banded appearance to the veins. Occasionally associated with the vein swarms are
675 randomly oriented irregular vein masses, ptygma-like veins, and veinlets of milky white quartz.
676 A less common type of veining are isolated veins and sets of veins parallel to bedding. The veins
677 are ~4–8 cm wide and syntaxial, with a single phase of massive white quartz growing out from
678 the wall rock of the vein.

679

680 3.2. Petrography

681 3.2.1. Sandstone

682 Sandstones consist mainly of fine- to coarse-grained sand that is clast-supported and
683 moderately to well sorted. Grains are subangular to sub-rounded, and grain boundaries tend to be
684 indistinct, with mainly longitudinal to concavo-convex contacts and rare sutured contacts.
685 Overall, the sandstones are characterized by a poorly developed fitted grain fabric (i.e.,
686 “complete” grain contacts, c.f., Wolf and Chilingarian, 1976). Sandstones are very pale brown

687 (10YR 7/4; Munsell Color Chart, 1994) to pale brown (10YR 6/3) in transmitted light at 35x
688 magnification. Most grains have a thin black (5Y 2.5/2) rim in transmitted light at 35x
689 magnification. When viewed at 500x magnification, the rim consists of minute, subhedral, semi-
690 transparent olive (5Y 4/3) crystals. The remainder of the grain interstices (i.e., other interstitial
691 material including matrix and cement), representing to ~5–15% of the area in thin sections, are
692 dark grayish brown (10YR 4/2) at 35x magnification in transmitted light. There is no visible pore
693 space.

694 Detailed petrography of the framework mode of sandstones can be found in Lowey
695 (2019). Sandstones are characterized by a dominance of lithic fragments and are classified as
696 litharenites to feldspathic litharenites ($\sim Q_{12}F_{26}L_{62}$) (Lowey, 2019). Lithic fragments include
697 mainly volcanic grains, with minor amounts sedimentary lithic grains (chert, limestone, and
698 mudstone), and rare metamorphic lithic fragments (phyllite and schist) are present. Feldspar
699 fragments are dominated by plagioclase grains (showing mainly Carlsbad+albite polysynthetic
700 twinning), and minor amounts of potassium feldspar grains (as untwined orthoclase) and rare
701 microcline grains (displaying “grid” or “tartan” twinning) are also present. Quartz fragments are
702 dominated by monocrystalline quartz grains, and minor amounts of polycrystalline quartz grains
703 are present. Quartz grains are unaltered, and approximately one-half of the grains have undulose
704 extinction and deformation lamellae, but it is uncertain if these structures were inherited or are
705 secondary in origin. Non-framework grains, accounting for <1% of all grains, include
706 clinopyroxene, orthopyroxene, hornblende, epidote, sphene, and zircon (all relatively unaltered),
707 carbonate allochems (recrystallized fossils, intraclasts, and possibly pellets), siltstone (indented
708 and squished), and biotite and muscovite (bent, frayed, and partly altered to chlorite).

709 The main secondary constituents include calcite, prehnite, chlorite, and illite (all
710 identified optically), as well as kaolinite (identified by XRD). Minor secondary constituents
711 include laumontite, celadonite, pyrite, magnetite, and hematite (all identified optically), in
712 addition to quartz and albite (both identified by XRD). Calcite was observed in all sandstone thin
713 sections. It occurs as specks of microspar replacing plagioclase, and as sparry cement replacing
714 grains and grain interstices (up to 20% of the area in several thin sections). The sparry cement
715 has straight, thick Type II calcite twins and rare curved, thick Type III twins (cf., Weber et al.,
716 2001). Illite was also observed in most thin sections, and it occurs as partial replacements of
717 plagioclase grains, as interstitial material (i.e., the variety ‘sericite’), and completely replaces
718 pre-existing grains of undetermined mineralogy (in which illite is relatively coarse-grained and
719 displays bold first-order yellow and red interference colors). Laumontite (*sensu stricto*, the
720 mineral is likely leonardite, the partially dehydrated version of laumontite; Neuhoff and Bird,
721 2001) was noted in ~50% of the thin sections. It occurs as clear, irregular masses with distinct
722 cleavage that forms poikilotopic patches replacing grains and as interstitial material. Celadonite
723 was seen in ~25% of the thin sections. It partially replaces pre-existing grains along with
724 chlorite, and completely replaces grains of pre-existing undetermined mineralogy. Celadonite is
725 typically bright blue-green and fibrous, has blue-green and pale green pleochroism, and
726 anomalous brown interference colors. Pyrite and magnetite were found ~75% of the thin
727 sections. They form irregular grains that are widely dispersed throughout the thin sections.
728 Hematite was observed in only a few thin sections and is associated with magnetite. Kaolinite,
729 quartz, and albite, all identified by XRD (< 2 μm size fraction), likely form interstitial material
730 that is too fine-grained to be identified optically. The sandstone thin sections also contain

731 microveins of quartz-prehnite, calcite-prehnite, and calcite-quartz-prehnite, that in turn are cross-
732 cut by calcite microveins.

733 In summary, the dominant secondary mineral assemblage in sandstone is prehnite \pm
734 laumontite + chlorite + kaolinite + illite \pm celedonite, indicative of high temperature zeolite facies
735 metamorphism (Liou et al., 1987).

736 In addition to the siliciclastic sandstones describe previously, four thin sections from
737 coquina beds (“shell hash”) were also examined. The coquinas beds are moderately well sorted
738 bivalve rudstones. Minor amounts of coarse-grained silt to coarse-grained sand, comprising
739 quartz, feldspar and volcanic rock fragments, are present as a matrix. Calcite is abundant and
740 occurs as coarse to very coarse sparry cement displaying straight, thick Type II twins and curved,
741 thick Type III twins. Bivalves have well developed microstylolites, with solution seams
742 highlighted by a film of opaque, black (5Y 2.5/2) material. Several bivalves are also broken and
743 splintered due to compaction. Celedonite is rare and completely replaces pre-existing grains of
744 undetermined mineralogy. Rare magnetite and pyrite occur as widely dispersed irregular grains.

745

746 3.2.2. Mudstone

747 Mudstones are relatively undeformed or have an incipient to moderately developed
748 foliation in thin sections. Undeformed mudstones are moderately to well sorted, and poorly to
749 well laminated with several laminae composed of coarse-grained silt. Rare wispy lamination is
750 present in several thin sections. Mudstones are almost an isotropic, dark grayish brown (10YR
751 4/2) in transmitted light at 35x magnification. Widely dispersed white (10YR 8/1) specks of
752 possibly quartz and plagioclase, and black (5Y 2.5/2) specks of pyrite are also present.

753 The main secondary constituents include quartz, albite, chlorite, and illite (all identified
754 by XRD), and minor amounts of calcite, stipnomelane, actinolite, and pyrite (all identified
755 optically), and rare garnet (identified optically). Quartz, albite, chlorite, and illite, identified by
756 XRD (< 2 μm size fraction), likely form the irresolvable turbid matrix that is too fine grained to
757 identify optically. Calcite is present in most thin sections and forms irregular patches of
758 microspar to sparry cement. Pyrite is rare and occurs as widely dispersed grains and irregular
759 masses.

760 Stipnomelane, actinolite, and garnet are restricted to deformed mudstones. Stipnomelane
761 was observed in ~50% of the thin sections of deformed mudstones. It occurs as small (~0.1 mm
762 long), elongated crystals that are strongly pleochroic dark brown and pale brown, and lack the
763 “bird's eye maple” texture present in biotite. Stipnomelane shows varying degrees of preferred
764 alignment, accounting for the foliation in the deformed mudstones. Actinolite was noted in one
765 thin section and is associated with stipnomelane. Actinolite forms small (~0.2 mm), poorly
766 aligned needles to radiating clusters, is weakly pleochroic pale green to clear, and displays
767 obvious cleavage. Garnet was observed in only two thin sections, and is also associated with
768 stipnomelane. It forms small (~0.3 mm diameter), euhedral grains.

769 In summary, mudstones are characterized by the secondary mineral assemblage quartz +
770 albite + chlorite + illite \pm calcite \pm stipnomelane that is non-diagnostic for determining the
771 metamorphic facies.

772

773 3.2.3. Hemipelagite

774 Hemipelagites are massive to poorly laminated in thin section. They appear light
775 brownish gray (10YR 6/2) to grayish brown (10YR 5/2) in transmitted light at 35x

776 magnification. Widely dispersed white (10YR 8/1) specks of quartz and black (5Y 2.5/2) specks
777 and minute cubes of pyrite are also present.

778 The major secondary constituents include calcite (identified optically), as well as illite,
779 kaolinite, and chlorite (identified by XRD), with minor amounts of celedonite and pyrite
780 (identified optically), and rare rhombohedral ‘ghosts’ of an unidentified mineral (observed
781 optically). Calcite is ubiquitous and occurs as irregular patches of microspar. Illite, kaolinite, and
782 chlorite, identified by XRD (<2 µm size fraction), likely form the irresolvable turbid matrix that
783 is too fine grained to identify optically. Rare celedonite occurs as distinctive bright blue-green
784 spots that occur widely scattered in the matrix. Small (~ 0.1 mm diameter) rhombohedral
785 “ghosts” observed in the matrix of one thin section may be poorly preserved carbonate (dolomite
786 or siderite), or laumontite crystals. The hemipelagite thin sections also contain microveins of
787 calcite-pyrite.

788 In summary, hemipelagites are characterized by the secondary mineral assemblage illite +
789 kaolinite + chlorite ± calcite ± celedonite that is also non-diagnostic for determining
790 metamorphic facies.

791

792 3.2.4. Volcaniclastics

793 The volcaniclastic rocks, geochemically classified as dacite-rhyolite (Lowey, 2011),
794 include shard-dominated tuff layers and crystal-dominated tuff layers. The petrology of the
795 crystal tuffs is similar to the siliciclastic sandstones described previously. Vitric tuffs are clast-
796 supported and well sorted. They consist of fine- to medium-grained sand-sized shards that are
797 angular, and platy to cusped. All of the shards are pseudomorphs of laumontite (viz., leonardite).
798 In addition, some shards appear to have been vesicular, with the vesicles now completely filled

799 by chlorite. Minor amounts of quartz, plagioclase, volcanic lithic fragments, and rare biotite
800 grains are also present. Vitric tuffs are pale brown (10 YR 6/3) or mottled light gray (10YR 6/1)
801 to very pale brown (10 YR 8/3) in transmitted light at 35x magnification. Most shards have a thin
802 (~0.05 mm) dark grayish brown (10YR 4/2) rim in transmitted light at 35x magnification. When
803 viewed at 500x magnification, the rim consists of minute, subhedral, semi-transparent olive
804 yellow (5Y 6/6) crystals.

805 The major secondary mineral constituent is laumontite (identified optically and by XRD),
806 with minor amounts of albite, chlorite, illite, prehnite, calcite, pyrite, and palagonite (identified
807 optically), as well as minor amounts of illite, and kaolinite (identified by XRD). Laumontite is
808 ubiquitous in all of the thin sections (~70 % by area). It occurs as clear, irregular masses with
809 distinct cleavage that form poikilotopic patches replacing shards and interstitial material. Albite
810 replaces some plagioclase grains, while other plagioclase grains appear unaltered. Albitized
811 plagioclase appears turbid, particularly towards the center of the grain, and exhibits irregular
812 twin boundaries that reveal a composition of ~Ab₉₀. Pale green chlorite was noted in most of the
813 thin sections. It occurs as specks replacing plagioclase grains, as a partial replacement of biotite
814 grains, as vesicle-filling cement in shards, and likely forms the olive yellow rim on shards. Illite
815 was also observed in all of the thin sections and it occurs as specks replacing plagioclase grains.
816 Calcite was observed in all the thin sections. It occurs as specks of microspar replacing
817 plagioclase grains, and as sparry cement replacing grains and grain interstices. Prehnite was
818 found in ~50 % of the thin sections. It comprises cloudy, granular aggregates that form irregular
819 poikilotopic patches replacing shards and interstitial material. Pyrite is rare and occurs as widely
820 dispersed, irregular grains; and rare spots of brown, semi-translucent material interpreted as
821 palagonite was observed in several thin sections. Quartz, illite, kaolinite, and albite, identified by

822 XRD (< 2 μm size fraction), likely form interstitial material too fine-grained to be identified
823 optically. Thin sections of vitric tuffs also contain microveins of quartz, calcite, calcite+quartz,
824 laumontite+quartz, and calcite+quartz+laumontite+prehnite.

825 In summary, vitric tuffs are characterized by the secondary mineral assemblage
826 laumontite ± prehnite + illite + chlorite + quartz, indicative of high temperature zeolite facies
827 metamorphism (Liou et al., 1987).

828

829 3.3. X-Ray Diffraction

830 Results of the XRD analyses are provided in Figure 6 (diffratograms), Figure 7
831 (compositional pie diagrams), and Supplementary Table S2. XRD analysis of bulk sandstone
832 samples show that they are dominated by plagioclase and quartz. The sandstones contain ~5–9
833 wt% of material that is <2μm. The clay-size material consists mainly of chlorite, kaolinite, and
834 illite, with minor amounts of calcite, quartz, and plagioclase (Fig. 7). Clay minerals detected in
835 the XRD analysis are difficult to identify by SEM analysis due to a lack of diagnostic
836 morphological features, but EDX analysis corroborates the XRD analysis. The clay minerals
837 occur in the matrix between framework grains (i.e., plagioclase, quartz, calcite, and muscovite)
838 as pore filling material.

839 XRD analysis of the bulk hemipelagite sample shows that it is dominated by calcite. The
840 hemipelagite contains ~4 wt% of material that is <2μm. The clay-size material consists mainly of
841 chlorite, kaolinite, and illite, with minor amounts of calcite. Clay minerals detected in the XRD
842 analysis are also difficult to identify in by SEM analysis due to a lack of diagnostic
843 morphological features, but EDX analysis corroborates the XRD analysis. Irregular flakes of

844 illite and poorly formed kaolinite and/or chlorite platelets occur tightly packed between
845 framework grains (i.e., calcite, quartz, and plagioclase).

846 XRD analysis of the bulk volcanoclastic sample shows that it is dominated by quartz and
847 laumontite. The volcanoclastic contains ~5 wt% of material that is $<2\mu\text{m}$. The clay-size material
848 consists mainly of laumontite and illite, with minor amounts of kaolinite, chlorite, quartz, albite,
849 and calcite (Fig. 7). SEM analysis reveals a predominance of interlocking aggregates of
850 columnar to tabular structures, and EDX analysis indicates that Si, Al, Ca, and O are the only
851 constituents composing the structures; the morphology and elemental composition of the
852 structures confirm that the structures are laumontite. Clay minerals detected in the XRD analysis
853 are again difficult to identify by SEM analysis due to a lack of diagnostic morphological
854 features, but EDX analysis corroborates the XRD analysis. The abundance of illite indicates the
855 tuff has been altered to a K-bentonite (Huff, 2016).

856 Only the $<2\mu\text{m}$ material was analyzed in the mudstones. The clay-size material consists
857 mainly of albite, quartz, chlorite, and illite (the two-layer monoclinic polytype $2M_1$), minor
858 amounts of calcite and potassium feldspar, and rare interstratified illite/smectite (I/S) (Fig. 7). In
859 particular, sample GL12-5 displays $<10\%$ interstratified I/S characterized by long-range Rietveld
860 ordering (i.e., R3). The KI for mudstone sample GL12-5 is $0.42 \Delta^\circ 2\theta$, and the AI is $0.34 \Delta^\circ 2\theta$,
861 whereas for mudstone sample GL26-1, the KI is $0.26 \Delta^\circ 2\theta$ and the AI is $0.33 \Delta^\circ 2\theta$. Three
862 alteration zones have been defined based on the KI: diagenetic, with $\text{KI} > 0.42 \Delta^\circ 2\theta$; anchizone,
863 with $0.42 \Delta^\circ 2\theta \leq \text{KI} \leq 0.25 \Delta^\circ 2\theta$; and epizone, as $\text{KI} < 0.25 \Delta^\circ 2\theta$ (Blenkinsop, 1988; Merriman
864 and Frey, 1999). The anchizone is transitional between diagenesis and metamorphism (i.e., the
865 epizone). The diagenetic zone is subdivided into shallow ($\text{KI} > 1.0 \Delta^\circ 2\theta$) and deep ($1.0 \Delta^\circ 2\theta >$
866 $\text{KI} > 0.42 \Delta^\circ 2\theta$) subzones, and the anchizone is subdivided into low ($0.42 \Delta^\circ 2\theta < \text{KI} < 0.30 \Delta^\circ 2\theta$)

867 and high subzones ($0.30 \Delta^{\circ}2\theta < KI < 0.25 \Delta^{\circ}2\theta$) (Valín et al., 2016). Árkai (1991) designated
868 boundaries for the three main KI zones based on AI: diagenetic, with $AI > 0.33 \Delta^{\circ}2\theta$; anchizone,
869 with $0.33 \Delta^{\circ}2\theta \leq AI \leq 0.26 \Delta^{\circ}2\theta$; and epizone, with $AI < 0.26 \Delta^{\circ}2\theta$. Note that KI and AI are
870 defined such that the values decrease with increasing alteration. Mudstone samples from the
871 Dezadeash Formation indicate deep diagenetic to high anchizone conditions.

872

873 3.4. Palynomorph Assemblage

874 Preservation of palynomorphs extracted from the mudstone and hemipelagite samples is
875 very poor (Supplementary Table S3). Only an extremely sparse assemblage of dark brown to
876 black, corroded silhouettes of what appear to be trilete spores, monosulcate pollen grains, and
877 possibly one bisaccate pollen grain are present. The majority of the organic residue is dominated
878 by palynodebris comprising: unstructured amorphous organic matter in the form of small (~ 20
879 μm), nearly equidimensional particles that are dark brown to black and semi-opaque or opaque
880 (“black debris”); slightly larger ($\sim 50 \mu\text{m}$), irregular “fluffy” masses that are dark brown and
881 partly translucent; minor amounts of dark brown globular masses that possibly represent
882 degraded *Botryococcus* colonies; and rare dark brown to black phytoclasts (leaf cuticles?) with
883 no clear internal structure. The spore and pollen “wrecks” indicate a TAI of ~ 4.5 , suggesting
884 mature thermal maturation.

885

886 3.5. Conodont Assemblage

887 Preservation of conodonts obtained from the limestone bolder is excellent
888 (Supplementary Table S4), and includes ramiform elements, *Neogondolella steinbergensis*
889 (Mosher, 1968) and *Epigondolella bidentata* (Mosher 1968) that indicate a Late Triassic (Late

890 Norian) age. Also present are ichthyoliths, microbivalves, and foraminifers. Garcia-Lopez et al.
891 (2001) proposed alteration zones similar to the KI and AI zones: diacaizone, with $CAI < 4$,
892 ancaizone, with $4 \geq CAI \leq 5.5$, and epicaizone, with $CAI > 5.5$, for which the CAI values increase
893 with increasing alteration. The conodonts indicate a CAI of ~ 4 – 4.5 , suggesting mature thermal
894 maturation and ancaizone conditions.

895 896 3.6. Pyrolysis

897 All but one sample indicates TOC < 0.3 wt%, rendering the majority of the T_{max} values as
898 suspect (Supplementary Table S5). Mudstone sample GL4-8 contains 1.26% TOC and has a
899 corresponding T_{max} value of 589 °C. Three stages of thermal maturity with respect to oil source
900 rocks have been designated as follows (Peters and Cassa, 1994): immature, with $T_{max} < 435$ °C
901 and attributed to diagenesis; mature (corresponding to the “oil window”), with T_{max} 435–470 °C
902 and due to catagenesis (increasing pressure and temperature); and postmature, with $T_{max} > 470$ °C
903 and indicative of metagenesis (i.e., incipient metamorphism). The one reliable sample is
904 postmature, suggesting metagenesis conditions. Calculated parameters for this sample indicate
905 $HI=5$ and $OI=33$, suggesting Type III (terrestrial) and IV (degraded or inert) kerogen is present.
906 Type III kerogen is also indicated using the values of $S2=0.06$ and $TOC=1.26\%$ from the
907 Dezadeash Formation and the $S2$ versus TOC graph of Langford and Blanc-Valleron (1990). HI ,
908 OI , $S2$ and TOC parameters are in agreement with the type of organic matter recovered during
909 the processing of samples for palynomorphs.

910 The extremely low TOC values discouraged the use of vitrinite reflectance analysis,
911 perhaps the most widely utilized technique for determining thermal maturity of sedimentary
912 rocks (Allen and Allen, 2013). The percent reflectivity in oil (R_o) of vitrinite (a kerogen maceral)
913 corresponds to the stage of thermal maturity: diagenesis, with $R_o < 0.5$ (also referred to as

914 immature); catagenesis, with $>0.5R_o < 1.3$ (also referred to as mature with $>0.5R_o < 1.3$, and
915 postmature with $>1.3 R_o < 2$); metagenesis, with $>2R_o < 4$ (also referred to as overmature); and
916 values of $R_o > 4$ are in the realm of metamorphism (Tissot and Welte, 1984; Hartkopf-Fröder et al.,
917 2015). A correlation between T_{max} and R_o has been proposed by Barker and Pawlewicz (1994)
918 and Jarvie (2018). Barker and Pawlewicz (1994) derived the equation $\ln(\%R_m) = (0.078T_{max}) - 1.2$,
919 which converts the T_{max} of 589 °C obtained from the mudstone sample to 3.8 % R_o . Jarvie (2018)
920 devised the equation $\text{Equivalent \%}R_o = (0.0165T_{max}) - 6.5143$, which converts the mudstone T_{max}
921 value of 589 °C to 3.2 Equivalent% R_o . The T_{max} value of the Dezadeash sample indicates a
922 metagenesis stage of thermal maturation (i.e., overmature), and conversion of the T_{max} value to
923 vitrinite reflectance values is consistent with metagenesis conditions.

924

925 3.7. Subsidence Analysis

926 Parameters used in the subsidence analysis of the Dezadeash Formation are poorly
927 constrained or unknown. Nevertheless, reasonable estimates can be made regarding the life span
928 of the basin, bathymetry of the basin, sediment accumulation rate, and compaction of the basin
929 fill. Based on macrofossils (i.e., *Buchia*), the Dezadeash Formation is Late Jurassic (Oxfordian,
930 163.1 Ma, Ogg et al., 2016) to Early Cretaceous (Valangin, 134.7 Ma, Ogg et al., 2016) in age,
931 equal to a duration of ~30 Ma. This time span is compatible with the life span of rift, forearc,
932 backarc, and foreland basins (Allen and Allen, 2013). Hemipelagite beds consisting of lime
933 mudstone (~30–33% CaCO_3) are common in the Dezadeash Formation, indicating that the floor
934 the basin was above the calcite compensation depth (CCD). The CCD at the time of the Jurassic-
935 Cretaceous boundary (145.7 Ma, Ogg et al., 2016) was ~3400–4000 m (van Andel, 1975;
936 Ridgwell, 2004). Furthermore, *Chondrites* and *Zoophycos* occur as endichnial trace fossils within

937 the hemipelagite beds, whereas *Paleodictyon* and *Urohelminthoida* are present as hypichnial
938 trace fossils on the soles of sandstone beds in thin- to medium-bedded sandstone-mudstone
939 couplets. The two trace fossil assemblages are similar to the *Zoophycos* ichnofacies (intermediate
940 between shelf and bathyal) and *Nereites* ichnofacies (bathyal to abyssal, particularly distal areas
941 of outer fans or fan-fringe facies of lobes and basin plain deposits) of Seilacher (2007),
942 suggesting paleowater depths of 1–4 km. However, ichnofacies are no longer regarded as
943 rigorous indicators of paleobathymetry, and are more reflective of environmental conditions (i.e.,
944 substrate and oxygen levels) during deposition (Uchman and Wetzel, 2012). In the absence of
945 unequivocal evidence of the paleobathymetry, a water depth of 1000 m is assumed. In addition,
946 sea-level at the Jurassic-Cretaceous boundary was ~15 m less than the present sea-level (Tennant
947 et al., 2017).

948 The exposed thickness of the Dezadeash Formation is ~3000 m. This is equivalent to a
949 compacted sediment rate of 100 m/Ma (100 mm/Ka), compatible with sedimentation rates of
950 modern submarine fans (Barnes and Normark, 1985; Reid et al., 1996). The present-day porosity
951 (ϕ_N) for the Dezadeash Formation is estimated to be 0.05 and the porosity when deposited (ϕ_O) is
952 inferred to have been 0.4 (based on porosity of shaly-sand, Sclater and Christie, 1980). The
953 decompacted thickness of the Dezadeash Formation at the time of deposition (T_O), assuming all
954 changes in porosity with depth are the result of compaction (Angevine et al., 1990, their equation
955 3.1), is ~4750 m. This is equivalent to a decompacted sediment rate of 158 m/Ma (158 mm/Ka)
956 that is also compatible with sedimentation rates of modern submarine fans (Barnes and Normark,
957 1985; Reid et al., 1996). Taking burial into account and assuming that the base of the Dezadeash
958 Formation was buried to 4000 m (i.e., 3000 m for the Dezadeash Formation plus 1000 m for the
959 Amphitheater Formation), the decompacted thickness of the Dezadeash Formation is ~3700 m.

960 This is equivalent to a decompacted sediment rate of 123 m/Ma (123 mm/Ka) that is also
961 compatible with sedimentation rates of modern submarine fans (Barnes and Normark, 1985;
962 Reid et al., 1996). The decompacted thicknesses of 4750 m and 3700 m represents a vertical
963 shortening of 36% and 19%, respectively.

964 The following parameters were used for backstripping the Dezadeash Formation
965 according to a one-dimensional, local isostatic Airy model employing the formula in Angevine et
966 al. (1990, their equation 3.4): decompacted thickness of the basin fill (S^*) = 3700 m and 4750 m,
967 density of the basin fill sediment (ρ_s) = 2685 kg/m³, density of the asthenosphere (ρ_a) = 3300
968 kg/m³, density of ocean water (ρ_w) = 1028 kg/m³, water depth of the basin (Wd_i) = 1000 m, and
969 sea-level below present day sea-level (ΔSL_i) = 15 m. The calculated tectonic subsidence is ~2000
970 m and ~2300 m respectively, suggesting that about 50% of the total subsidence is due to tectonic
971 driving forces, and 50% is due to sediment loading of the basin fill. The backstripped depth to
972 the basin basement is equivalent to a tectonic subsidence rate of ~66 m/Ma (66 mm/Ka) and ~76
973 m/Ma (76 mm/Ka) respectively, compatible with tectonic subsidence rates of forearc and rift
974 basins (Xie and Heller, 2009; Allen and Allen, 2013).

975

976 4. Discussion

977 4.1. Constraints on the burial history of the Nutzotin-Dezadeash basin

978 Typically, very low-grade metamorphism (VLGM) of siliciclastic sedimentary rocks
979 results in a complex mixture of heterogeneous relic detrital minerals, patchiness of secondary
980 minerals, and variable amounts of altered organic material, all of which may be individually
981 metastable, in addition to an absence of a well developed penetrative tectonic fabric (Kisch,
982 1991; Merriman and Peacor, 1999). The bulk composition of the sedimentary protolith (i.e.,

983 basically the type of sedimentary rock) exerts a first-order control on the range of secondary
984 minerals formed during VLGGM (Caddick and Thompson, 2008; Frey and Kisch, 1987), and
985 therefore a variety of techniques must be employed to determine the post-depositional alteration
986 of rocks of diverse lithologies.

987 The results of various techniques utilized in determining the mineralogic and organic
988 thermal indicators in rocks of diverse lithologies (e.g., sandstone, mudstone, hemipelagite, and
989 tuff) from the Dezadeash Formation are summarized in a correlation diagram (Fig. 8). In
990 particular, secondary mineral assemblages in sandstone and tuff indicate high temperature zeolite
991 facies metamorphism; Kübler indices of illite and *Árkai* indices of chlorite in mudstone record
992 diagenetic to high anchizone metapelitic conditions; and pyrolysis of organic matter and the
993 color of organic matter (i.e., Thermal Alteration Index of palynomorphs and Conodont Alteration
994 Index) in mudstone and hemipelagite beds suggest that thermal maturation reached catagenesis
995 to mesogenesis stages. Correlation of the various mineralogic and organic thermal indicators is
996 internally consistent and suggests VLGGM of the Dezadeash Formation. The development of an
997 incipient slaty cleavage (i.e., S₀-S₁ pencil structure) in the Dezadeash Formation is also
998 compatible with VLGGM (Kisch, 1991; Merriman and Peacor, 1999).

999 Note that on the correlation diagram, illite and chlorite crystallinities document slightly
1000 higher thermal alteration than secondary mineral assemblages, whereas organic matter records an
1001 even slightly higher thermal alteration than illite and chlorite crystallinities. This general trend of
1002 increasing thermal alteration from zeolite facies, to diagenesis-anchizone conditions, to
1003 catagenesis-mesogenesis stages is attributed to the various “phases” (i.e., hydrous Ca-Al
1004 silicates, sheet silicates, and organic matter) reacting at different rates, or kinetics. (Kisch, 1987;
1005 Merriman and Frey, 1999; Merriman and Peacor, 1999). The varying reaction kinetics imply that

1006 these out-of-equilibrium phases provide only qualitative estimates of paleopressure and
1007 paleotemperature and (Essene, 1989; Frey et al., 1991; Merriman and Peacor, 1999).

1008 A first-approximation of the P-T conditions experienced by the Dezadeash Formation can
1009 be derived from the secondary mineral assemblage: zeolite facies metamorphism is generally
1010 considered to range from 200–300 °C with total pressures below 3 kbar (Liou et al., 1987;
1011 Bousquet, et al., 2008), and the high temperature zeolite facies (i.e., laumontite with prehnite) is
1012 calculated to reach a temperature of around 230 °C (Liou et al., 1987). In addition, the absence of
1013 wairakite and lawsonite suggests metamorphic conditions are limited by the laumontite-wairakite
1014 and laumontite-lawsonite equilibrium for $P_{\text{tot}}=P_{\text{CO}_2}$, specifically $P < 3$ kbars and $T < 300$ °C
1015 (Liou, 1971; Boles and Coombs, 1975). If these P-T values represent the *absolute maximum*
1016 conditions experienced by the Dezadeash Formation, and assuming a rock density of $\rho=2685$
1017 kg/m^3 , the maximum depth of burial of the strata would be ~11 km, equivalent to a maximum
1018 paleogeothermal gradient of ~27 °C/km (i.e., within a “normal” geothermal gradient of 25-30
1019 °C/km; Merriman and Frey, 1999). The widespread veining
1020 (quartz±calcite±laumontite±prehnite) in the strata also suggests P-T conditions did not exceed
1021 the brittle-ductile transition zone that occurs at a depth of ~13–18 km and temperatures of ~250–
1022 400 °C (Wikipedia, accessed August 28, 2020).

1023 Other P-T constraints include the laumontite dehydration equilibrium of laumontite=
1024 wairakite+2H₂O at ~230 °C and 0.5 kbar, ~255 ±5 °C and 1 kbar, and ~282 ±5 °C and 2 kbar
1025 (Liou, 1970); the laumontite equilibrium of laumontite=anorthite+2quartz+4H₂O at 310 ±10 °C
1026 and 1 kbar, and 317 ±10 °C and 2 kbar (Thompson, 1970); the laumontite equilibrium of
1027 laumontite=lawsonite +2quartz+2H₂O at 2.75 ±0.25 kbar and 250 °C (Thompson, 1970); the
1028 laumontite stability of paragonite+prehnite+5quartz+6H₂O =2laumontite at <260 °C; and the

1029 laumontite stability field restricted to 180-285 °C at <3 kbar in the NCASH system (Na₂O-Cao-
1030 Al₂O₂-SiO₂-H₂O) with excess H₂O and SiO₂, and the zeolite facies estimated to occur between
1031 210–250 °C at 2.1–2.9 kbar (Schmidt et al., 1997).

1032 P-T restrictions from other minerals include the prehnite stability of
1033 3prehnite+chlorite+4quartz+18H₂O=4hulandite+tremolite estimated to be between 200–280 °C
1034 and <3 kbar (Frey et al., 1991); the prehnite stability calculated at T >200 °C and P <2 kbar for
1035 low XCO₂ (McSween et al., 2015); clay compositions containing 5-10% smectite in I/S
1036 interstratification corresponding to 200–250 °C (Weaver, 1989); the R=1 to R=3 transition (i.e.,
1037 short-range to long-range Rietveld ordering in I/S clay) occurring at ~170–180 °C (Aldega et al.,
1038 2007); the 1M to 2M polytypism transition in illite between 200–350 °C at ~2 kbar (Frey, 1987);
1039 straight thick Type II calcite twins developing in the range of 150–300 °C (Burkhard, 1993); the
1040 diagenesis/anchizone boundary estimated at 240 ±15 °C according to fluid inclusion data (Mullis
1041 et al., 2017); and the effective closure temperature (i.e., the temperature for 90% track retention)
1042 of zircon fission tracks at ~240 °C (Bernet and Garver, 2005).

1043 Another estimate of the maximum paleotemperature reach by the Dezadeash Formation
1044 can be obtained from the calculated vitrinite reflectance values. Although several empirically
1045 based formulas have been derived to translate vitrinite data into peak paleotemperature, the
1046 formula by Barker and Pawlewicz (1994), namely $T_{\text{peak}} = [\ln(\%R_o) + 1.68]/0.0124$, was employed
1047 because it is designed for burial heating. Using the calculated equivalent reflectance values of 3.2
1048 and 3.8 for the Dezadeash Formation results in temperatures of 229 °C and 243 °C, respectively.
1049 And based on a diagram of nomograms of vitrinite reflectance vs. time and maximum
1050 temperature (Sweeney and Burnham, 1990, their Fig. 5), the same calculated equivalent
1051 reflectance values correspond to temperatures between ~220–240 °C. Lastly, employing the

1052 Arrhenius plot of temperature vs. time by Epstein et al., (1977, their Figure 9), the conodont CAI
1053 value of 4–4.5 reveals a temperature of ~190–230 °C, whereas the same CAI value equates to a
1054 maximum temperature of 260–285 °C, according to temperatures determined by Raman
1055 spectroscopy of carbonaceous material in conodont species (McMillan and Golding, 2019).

1056 Based on the above P-T constraints (particularly the laumontite stability temperature,
1057 estimates of the P-T region for the zeolite facies, the diagenesis/anchizone boundary determined
1058 from fluid inclusion data, and the effective closure temperature of zircon fission tracks), a
1059 reasonable estimate for the maximum P-T conditions experience by the Dezadeash Formation is
1060 2.5 kbar and 250 °C. The estimated paleopressure corresponds to a burial depth of 9.5 km (again
1061 assuming a rock density of $\rho=2685 \text{ kg/m}^3$), equivalent to a maximum paleogeothermal gradient
1062 of ~27 °C/km (i.e., still a normal geothermal gradient). The estimated P-T conditions are
1063 consistent with the observation by Merriman and Peacor (1999) that burial beneath 4-12 km of
1064 overburden are required (assuming a typical geothermal gradient of 25 °C/km) to bring about
1065 temperatures of 200-300 °C that characterize VLGM. Thus, the Nutzotin-Dezadeash basin
1066 appears to have been subject to VLGM (the Denali fault did not displace the proximal half of the
1067 basin— the Nutzotin Mountains sequence— from the distal half or the Dezadeash Formation
1068 until Eocene time), with the Dezadeash Formation reaching the high temperature zeolite facies.

1069

1070 4.2. Implications regarding the tectonic evolution of the Northern Cordillera

1071 The estimated maximum paleotemperature experienced by the Dezadeash Formation,
1072 together with published thermochronometric data for the strata, are plotted on a time vs.
1073 temperature diagram (Fig. 9). The diagram shows that the Dezadeash Formation underwent
1074 rapid, short-term heating followed by gradual, long-term cooling. Also shown in the diagram is

1075 the tectonic subsidence curve calculated for the Dezadeash Formation, indicating rapid, short-
1076 term subsidence followed by gradual, long-term uplift. The general trend of both plots is similar
1077 (i.e., a steep downward slope followed by a gradual upward slope), indicating correspondence
1078 between the diverse types of data.

1079 The thermochronometric data of McDermott et al. (2019) are not plotted in Figure 9
1080 because it is unclear what unit was sampled. On the geologic map of the Kluane Lake area
1081 (Dodds and Campbell, 1992c), their sample is from an area mapped as undifferentiated Upper
1082 Triassic to Lower Cretaceous phyllite, greywacke, and conglomerate that includes presumed
1083 noncalcareous rocks of the McCarthy Formation (Triassic) and rocks of the Dezadeash
1084 Formation (Jurassic-Cretaceous). Perplexingly, McDermott et al. (2019) do not identify any of
1085 the stratigraphic units that their samples are from. Furthermore, the area McDermott et al. (2019)
1086 collected their sample is characterized by intense faulting, and this may have affected the
1087 integrity of their sample, even if it was collected from the Dezadeash Formation. Namely,
1088 McDermott et al. (2019) obtained a ZHe age of ~14 Ma compared to ~60 and ~69 Ma by
1089 Enkelmann et al. (2017), and McDermott et al. (2019) report a ZFT age of is ~136 Ma versus
1090 ~110 Ma by Enkelmann et al. (2017) (Table 1).

1091 Sedimentary basins display different geothermal gradients due to differences in heat flow
1092 associated with various tectonic settings (Siever, 1979; Peacock, 1996; Doglioni et al., 1999;
1093 Woodcock, 2004; Allen and Allen, 2013). Accordingly, the geothermal gradient of a sedimentary
1094 basin may help distinguish the type of basin, and hence the tectonic setting of the basin (Allen
1095 and Allen, 2013). Results of this study suggest the Nutzotin-Dezadeash basin was characterized
1096 by a normal paleogeothermal gradient (~27 °C). Forearc, foreland, “failed” rift, and continental
1097 “sag” basins display normal or near normal geothermal gradients (e.g., 20–30 °C), whereas

1098 crustal-scale strike-slip, rift and backarc basins are associated with higher geothermal gradients
1099 (e.g., 35–50 °C) (Siever, 1979; Doglioni et al., 1999; Leloup et al., 1999; Merriman, 2005; Vieira
1100 and Hamza, 2018). The secondary clay mineral assemblage observed in the Dezadeash
1101 Formation may also be used to infer the tectonic setting of the Nutzotin-Dezadeash basin.
1102 According to Merriman (2002, 2005) and Stone and Merriman (2004), clay minerals buried in a
1103 sedimentary basin undergo a series of transformations that reflect the geothermal conditions of
1104 the basin, as determined by the tectonic setting. Extensional settings, associated with higher than
1105 normal paleogeothermal gradients, are characterized by a complex assemblage of both K-rich
1106 and Na-rich 2:1 dioctahedral clays (generally aluminous and phengite-poor), whereas convergent
1107 settings, associated with lower to normal paleogeothermal gradients, are characterized by a
1108 simple assemblage of 2:1 dioctahedral clays (phengitic k-micas, or illite) and rare Na/K-mica
1109 (Stone and Merriman, 2004). The secondary clay mineral assemblage observed in the Dezadeash
1110 Formation is characterized by a narrow range of clay minerals including 2M₁ illite and chlorite,
1111 suggesting a convergent rather than extensional tectonic setting. Based on the inferred
1112 paleogeothermal gradient and secondary clay mineral assemblage of the Dezadeash Formation,
1113 rift, backarc, and crustal-scale strike-slip basins fail the “thermal history test”.

1114 Sedimentary basins likewise display different tectonic subsidence curves attributed to
1115 different tectonic driving mechanisms associated with contrasting tectonic settings (Angevine et
1116 al., 1990; Xie and Heller, 2009; Allen and Allen, 2013). Consequently, the tectonic subsidence
1117 curve of a sedimentary basin may also help differentiate the type of basin type, and therefore the
1118 tectonic setting of the basin (Angevine et al., 1990; Xie and Heller, 2009; Allen and Allen,
1119 2013). The tectonic subsidence curve for the Dezadeash Formation indicates rapid, short-term
1120 subsidence of 66–76 m/Ma (66–76 mm/Ka), assuming a basin lifespan of 30 Ma, followed by

1121 gradual, long-term uplift of 22 m/Ma (~22 mm/Ka), assuming uplift lasted about 90 Ma (i.e.,
1122 from the minimum age of the Dezadeash Formation of 130 Ma, to the maximum age of the
1123 Amphitheater Formation of ~40 Ma).

1124 Although several parameters used in backstripping the Dezadeash strata are poorly
1125 constrained, these uncertainties tend to affect the absolute value of the calculated tectonic
1126 subsidence by ± 100 – 200 m and not the overall shape of the curve (Gallagher, 1989; Angevine et
1127 al., 1990; Audet and McConnell, 1994). Typical tectonic subsidence curves for various basins
1128 include: moderately steep to near-vertical linear curves reflecting subsidence rates between 10–
1129 100 m/Ma (10–100 mm/Ka) and lifespans of 10–60 Ma for forearc basins; moderately steep
1130 linear curves reflecting subsidence rates of 200–400 m/Ma (200–400 mm/Ka) that decrease to 15
1131 m/Ma (15 mm/Ka) and lifespans of 30–70 Ma for backarc basins; upward convex curves
1132 reflecting subsidence rates of 200–500 m/Ma (200–500 mm/Ky) and lifespans of 10–50 Ma for
1133 peripheral foreland basins; moderately steep linear curves reflecting subsidence rates of <50
1134 m/Ma (<50 mm/Ka) and lifespans of 20–60 Ma for retroarc foreland basins; near-vertical linear
1135 curves reflecting subsidence rates of >500 m/Ma (>500 mm/Ka) and lifespans of 3–10 Ma for
1136 strike-slip basins; and downward convex curves reflecting subsidence rates of <200 m/Ma (<200
1137 mm/Ka) that decreases exponentially to <50 m/Ma (<50 mm/Ka) and lifespans of 10–100 Ma for
1138 rift basins (Angevine and Heller, 1990; Koesoemadinata et al., 1995; Woodcock, 2004; Xie and
1139 Heller, 2009; Sinclair and Naylor, 2012; Allen and Allen, 2013). Based on the tectonic
1140 subsidence curve calculated for the Dezadeash Formation (i.e., the shape and subsidence rate),
1141 together with the inferred life-span of the Nutzotin-Dezadeash basin, peripheral foreland, strike-
1142 slip, and rift basins fail the “tectonic subsidence curve test”.

1143 Although tectonic subsidence curves may be a useful tool in basin analysis, they are not a
1144 “magic wand” for identifying the tectonic setting of sedimentary basins. The original
1145 compilation of tectonic subsidence curves by Xie and Heller (2009) was based on a limited data
1146 set, and as they cautioned, the method should be used in parallel with other basin analysis
1147 techniques. In addition, some tectonic subsidence curves may represent a complex signal
1148 involving multiple tectonic driving mechanisms (Xie and Heller, 2009; Allen and Allen, 2013);
1149 tectonic subsidence curves may vary within a basin (Parra et al., 2009; Caravaca et al., 2017);
1150 tectonic subsidence curves calculated for basins with a history of overpressuring ignore the
1151 evolution of porosity with time (Audet and McConnell, 1994); and tectonic subsidence curves
1152 for foreland basins may be influenced by the load of the subducted lithospheric slab (in addition
1153 to the topographic load of the thrust wedge) as well as dynamic subsidence due to subduction
1154 (Ziegler et al., 2002; Painter and Carrapa, 2013). Despite these caveats, the overall shape of the
1155 tectonic subsidence curves generally reflects the main tectonic driving force of the tectonic
1156 setting (i.e., downward concave curves corresponding to stretching and thermal cooling of the
1157 lithosphere in divergent settings, upward convex curves corresponding to flexural loading of the
1158 lithosphere in convergent settings, and near-vertical linear curves corresponding to shearing of
1159 the lithosphere in transform settings (Allen and Allen, 2013; Baiyegunhi et al., 2017).

1160 A prevailing model for the tectonic setting of the Nutzotin-Dezadeash basin and Gravina
1161 basin invokes deposition in a sinistral transpressional, crustal-scale rift or strike-slip fault
1162 between the YCT and WCT (Gehrels et al., 2009; Yokelson et al., 2015; Geisler et al., 2016;
1163 Peacha et al., 2016; Beranek et al., 2017). However, the geothermal gradient, time-temperature
1164 plot, and tectonic subsidence curve for the Dezadeash Formation are not compatible with a rift or

1165 crustal-scale strike-slip origin. A similar conclusion was reached for the Gravina belt in
1166 southeastern Alaska by Stowell et al. (2000).

1167 Current reconstructions of the structural deformation and crustal-scale structure of the
1168 northern Cordillera in Yukon suggest that the Dezadeash Formation was thrust to depths >20 km
1169 beneath the Blanchard River assemblage, Kluane Schist, and YCT around ~90 Ma (Mezger et
1170 al., 2001b; Johnston and Canil, 2007; Stanley, 2012; Vice, 2017). The maximum pressure
1171 experienced by the Dezadeash Formation was < 3 kbar and likely ~2.5 kbar (or ~9.5 km of
1172 burial), whereas the Blanchard River assemblage experienced 6.3–6.7 kbar (Vice, 2017) or ~23-
1173 25 km of burial (assuming a rock density of 2,750 kg/m³), and the Kluane schist reached 8 kbar
1174 or ~30 km of burial (again assuming a rock density of 2,750 kg/m³) (Stanley, 2012; Vice, 2017).
1175 Furthermore, the time vs. temperature graph (Fig. 9) demonstrates that the Dezadeash Formation
1176 was undergoing gradual uplift before and during deposition of the Blanchard River assemblage,
1177 and that the Dezadeash Formation was also undergoing uplift during the inferred underthrusting
1178 of the Blanchard River assemblage and Kluane Schist beneath the YCT. Therefore, the proposed
1179 structural deformation and crustal-scale reconstructions are not supported by this study.

1180 Rather, the Dezadeash Formation (and Nutzotin-Dezadeash basin) appears to have been
1181 subject to a temporally and spatially separate burial, deformation, and exhumation history than
1182 that experienced by the Blanchard River assemblage or Kluane Schist, and was only marginally
1183 affected by the Coast Plutonic Complex (Lowey, 2000). Furthermore, the tectono-metamorphic
1184 history of the Nutzotin-Dezadeash basin contrasts sharply with that of the Gravina belt and
1185 Gravina sequence in southeastern Alaska. The Gravina belt was subject to zeolite to amphibolite
1186 facies metamorphism and experienced pressures of 8.7 ± 1 kbar (~25–30 km depth) and
1187 temperatures between 465 ± 50 °C to 545 ± 75 °C (McClelland et al., 1991; Cohen and

1188 Lundberg, 1993), whereas the Gravina sequence experienced greenschist to amphibolite facies
1189 metamorphism (Rubin and Saleeby, 1992). The tectono-metamorphic history of the Gravina belt
1190 and Gravina sequence is attributed to well documented northeast directed underthrusting of both
1191 units beneath the WCT in mid-Cretaceous time as a result of final accretion of the WCT to the
1192 North American margin (Crawford et al., 1987; Rubin et al., 1990; McClelland et al., 1991;
1193 McClelland and Mattinson, 2000; Stowell and Crawford, 2000; Trop and Ridgway, 2007; Trop
1194 et al., 2020). The contradistinction in tectono-metamorphic histories of the more northerly
1195 Nutzotin-Dezadeash basin compared to the more southerly Gravina basins may be a
1196 manifestation the oblique convergence and diachronous, south to north accretion of the WCT and
1197 Chitina arc to the YCT (Trop and Ridgway, 2007; Shepard et al., 2013; Sigloch and Mihalynuk,
1198 2017; Trop et al., 2020).

1199
1200

1201 6. Conclusions

1202 Secondary mineral assemblages in sandstone and tuff indicate high temperature zeolite
1203 facies metamorphism; Kübler indices of illite and Árkai indices of chlorite in mudstone record
1204 diagenetic to high anchizone metapelitic conditions; and pyrolysis of organic matter and the
1205 color of organic matter (i.e., Thermal Alteration Index of palynomorphs and Conodont Alteration
1206 Index) in mudstone and hemipelagite beds suggest that thermal maturation reached catagenesis
1207 to mesogenesis stages. Correlation of the various mineralogic and organic thermal indicators is
1208 internally consistent and suggests VLGM of the Dezadeash Formation. The development of an
1209 incipient slaty cleavage (i.e., S0-S1 pencil structure) in the Dezadeash Formation is also
1210 compatible with VLGM.

1211 Based mainly on published estimates for the laumontite stability temperature, the P-T
1212 region for the zeolite facies, the temperature of the diagenesis/anchizone boundary, and the
1213 effective closure temperature of zircon fission tracks, a reasonable estimate for the maximum P-
1214 T conditions experience by the Dezadeash Formation are 2.5 kbar and 250 °C. The estimated
1215 paleopressure corresponds to a burial depth of 9.5 km (assuming a rock density of $\rho=2685$
1216 kg/m^3), equivalent to a maximum paleogeothermal gradient of ~ 27 °C/km (i.e., a normal
1217 geothermal gradient).

1218 The estimated maximum paleotemperature experienced by the Dezadeash Formation,
1219 together with published thermochronometric data for the strata, shows that the Dezadeash
1220 Formation underwent rapid, short-term heating followed by gradual, long-term cooling. A
1221 calculated tectonic subsidence curve for the Dezadeash Formation indicates rapid, short-term
1222 subsidence, followed by gradual, long-term uplift. The secondary clay mineral assemblage
1223 associated with the rapid heating and subsidence is characterized by a narrow range of clay
1224 minerals dominated by $2M_1$ illite and chlorite. The thermal history, subsidence history, and
1225 secondary clay mineral assemblage are inconsistent with deposition in peripheral foreland,
1226 backarc, strike-slip, and rift basins, in accordance with published geothermal gradients, tectonic
1227 subsidence curves, and clay mineral assemblages for different sedimentary basins from various
1228 tectonic settings.

1229 The thermal history and subsidence history of the Dezadeash Formation are also
1230 inconsistent with reconstructions of the deformation and crustal-scale structure of the Northern
1231 Cordillera that posit the Dezadeash Formation was thrust to depths >20 km beneath the
1232 Blanchard River assemblage, Kluane Schist, and YCT around ~ 90 Ma. Rather, the Dezadeash
1233 Formation was undergoing cooling and uplift when the Blanchard River assemblage experienced

1234 pressures of 6.3-6.7 kbar (~23-25 km of burial, assuming a rock density of 2,750 kg/m³), and the
1235 Kluane Schist reached pressures of 8 kbar (~30 km of burial, again assuming a rock density of
1236 2,750 kg/m³) around ~80 Ma. The Dezadeash Formation (and Nutzotin-Dezadeash basin)
1237 appears to have experienced a temporally and spatially separate burial, deformation, and
1238 exhumation history than that experienced by either the Blanchard River assemblage or Kluane
1239 Schist. The tectono-metamorphic history of the Dezadeash Formation contrasts sharply with the
1240 Gravina belt and Gravina sequence, which were apparently underthrust (~25-30 km) beneath the
1241 YCT.

1242

1243

1244 Acknowledgements

1245 This study was partly funded by the Northern Research Institute and I wish to
1246 acknowledge that field work was undertaken in the traditional territory of the Champagne and
1247 Aishihik First Nations. Aaron Ogden, Marty Mossop, and Werner Liebau are thanked for
1248 providing field assistance in the early phases of this project. Discussions with Stephen Johnston
1249 regarding the “Dezadeash molasse” were, as always, entertaining. Data for this research are
1250 included in this paper and supplementary information files (available through the Open Science
1251 Framework at: <https://doi.org/10.17605/OSF.IO/5264J>), in addition to data cited from:
1252 Enkelmann, E., Piestrzeniewicz, A., Falkowski, S., & Stübner, K., 2017, Thermochronology in
1253 southeast Alaska and southwest Yukon: implications for North American plate response to
1254 terrane accretion, *Earth and Planetary Science Letters*, 457, 348–358; and McDermott, R.G.,
1255 Ault, A.K., Caine, J.S., & Thompson, S.N. , 2019, Thermotectonic history of the Kluane Ranges

1256 and evolution of the eastern Denali fault zone in southwestern Yukon, Canada. *Tectonics*, 38,
1257 2983–3010. The author declares no conflict of interest.

1258

1259

1260 **References**

1261 Aldega, L., Corrado, S., Grasso, M., & Maniscalco, R. (2007). Correlation of diagenetic data
1262 from organic and inorganic studies in the Appeninic-Maghrebian fold-and-thrust belt: A case
1263 study from eastern Sicily. *The Journal of Geology*, 115(3), 335–353.

1264 <https://doi.org/10.1086/512756>

1265

1266 Allen, P.A., & Allen, J.R. (2013). *Basin Analysis: Principles and Application to Petroleum Play*
1267 *Assessment* (3rd Ed.). New York: Wiley-Blackwell.

1268

1269 Amato, J.M., Rioux, M.E., Kelemen, P.B., Gehrels, G.E., Clift, P.D., Pavlis, T.L., & Draut, A.E.
1270 (2007), U-Pb geochronology of volcanic rocks from the Jurassic Talkeema Formation and
1271 detrital zircons from prearc and postarc sequences: Implications for the age of magmatism and
1272 inheritance in the Talkeetna arc. In K.D. Ridgway, J.M. Trop, J.M.G Glen, & J.M. O'Neill (Eds.)
1273 *Tectonic Growth of a Collisional Continental Margin: Crustal Evolution of Southern Alaska*,
1274 *Geological Society of America Special Paper 431* (pp. 253–271). Boulder, Colorado: Geological
1275 Society of America. [https://doi.org/10.1130/2007.2431\(11\)](https://doi.org/10.1130/2007.2431(11))

1276

1277 Anderson, T., Elburg, M.A., & Magwaza, B.N. (2019). Sources of bias in detrital zircon
1278 geochronology: Discordance, concealed lead loss and common lead correction. *Earth-Science*
1279 *Reviews*, 197, 1–15. <https://doi.org/10.1016/j.earscirev.2019.102899>
1280

1281 Anderson, T.H. (2015). Jurassic (170–150 Ma) basins: the tracks of a continental-scale fault, the
1282 Mexico-Alaska megashear, from the Gulf of Mexico to Alaska. In T.H. Anderson, A.N.
1283 Didenko, C.L. Johnson, A.I. Khanchuk, & J.H. MacDonald, Jr. (Eds.), *Late Jurassic Margin of*
1284 *Laurasia—A Record of Faulting Accommodating Plate Rotation*, Geological Society of America
1285 *Special Papers 513* (pp. 1–82). Boulder, Colorado: Geological Society of America.
1286 [https://doi.org/10.1130/2015.2513\(03\)](https://doi.org/10.1130/2015.2513(03))
1287

1288 Angevine, C.L., Heller, P.L., & Paola, C. (1990). Quantitative sedimentary basin modeling.
1289 *Continuing Education Course Note Series 32*. Tulsa, Oklahoma: The American Association of
1290 Petroleum Geologists
1291

1292 Andronicos, C.L., L.S. Hollister, C. Davidson, & D. Chardon (1999). Kinematics and tectonic
1293 significance of transpressive structures within the Coast Plutonic Complex, British Columbia.
1294 *Journal of Structural Geology*, 21, 229–243. [https://doi.org/10.1016/S0191-8141\(98\)00117-5](https://doi.org/10.1016/S0191-8141(98)00117-5)
1295

1296 Árkai, P. (1991). Chlorite crystallinity: an empirical approach and correlation with illite
1297 crystallinity, coal rank and mineral facies as exemplified by Palaeozoic and Mesozoic rocks of
1298 northeast Hungary. *Journal of Metamorphic Geology*, 9, 723–734.
1299 <https://doi.org/10.1111/j.1525-1314.1991.tb00561.x>

1300

1301 Armstrong, R.L. (1988). Mesozoic and Early Cenozoic Magmatism of the Canadian Cordillera.

1302 *Geological Society of America Special Papers 218*, 55–92.

1303 <https://doi.org/10.1130/SPE218-p55>

1304

1305 Audet, D. M., & McConnell, J. D. C. (1994) Establishing resolution limits for tectonic

1306 subsidence curves by forward basin modelling. *Marine Petroleum Geology Letters*, 11, 400–411.

1307 [https://doi.org/10.1016/0264-8172\(94\)90058-2](https://doi.org/10.1016/0264-8172(94)90058-2)

1308

1309 Baiyegunhi, C., Liu, K., & Gwavava, O. (2017) Sedimentation rate and subsidence history of the

1310 southeastern Karro basin, South Africa, using 1D backstripping method. *Arabian Journal of*

1311 *Geosciences*, 10(225), 1–21. <https://doi.org/10.1007/s12517-07-3009-x>

1312

1313 Barker, Ch.E., & Pawlewicz, M.J. (1986). The correlation of vitrinite reflectance with maximum

1314 temperature in humic organic matter. In G. Buntebarth & L. Stegena (Eds.), *Lecture Notes in*

1315 *Earth Sciences 5* (pp. 79–93). Paleothermics, Springer-Verlag: Berlin.

1316 <https://doi.org/10.1007/BFb0012103>

1317

1318 Barker, C.E., & Pawlewicz, M.J. (1994). Calculation of vitrinite reflectance from thermal

1319 histories and peak temperatures, a comparison of methods. In P. Mukhopadhyay (Ed.), *Vitrinite*

1320 *reflectance as a maturity parameter* (pp. 216–219). ACS Symposium Series, American Chemical

1321 Society. <https://doi.org/10.1021/bk-1994-0570.ch014>

1322

1323 Barker, F. (1987). Cretaceous Chisana island arc of Wrangellia, eastern Alaska. *Geological*
1324 *Society of America Abstracts with Programs*, 19: 580.

1325

1326 Barnes, N.E., & Normark, W.R. (1985). Diagnostic parameters for comparing modern submarine
1327 fans and ancient turbidite systems. In: A.H. Bouma, W.R. Normark, and N.E. Barnes (Eds.),
1328 *Submarine Fans and Related Turbidite Systems* (pp. 216–219). Springer-Verlag: New York,
1329 New York.

1330

1331 Behar, F., Beaumont, V., & Penteado, H.L. (2001). Rock-Eval 6 Technology: Performances and
1332 Developments. *Oil & Gas Science and Technology — Rev. IFP*, 56(2), 111–134.
1333 <https://doi.org/10.2516/ogst:2001013>

1334

1335 Beranek, L.P., McClelland, W.C., van Staal, C.R., Israel, S., & Gordee, S.M. (2017). Late
1336 Jurassic flare-up of the Coast Mountains arc system, NW Canada, and dynamic linkages across
1337 the northern Cordilleran orogen. *Tectonics*, 36, 877–901. <https://doi.org/10.1002/2016T004254>

1338

1339 Beranek, L. P., C. R. van Staal, S. M. Gordee, W. C. McClelland, S. Israel, & M. G. Mihalynuk
1340 (2012). Tectonic significance of Upper Cambrian-Middle Ordovician mafic volcanic rocks on
1341 the Alexander terrane, Saint Elias Mountains, northwestern Canada. *Journal of Geology*, 120,
1342 293–314. <https://doi.org/10.1086/664788>

1343

1344 Beranek, L.P., van Staal, C.R., McClelland, W.C., Joyce, N., & Israel, S. (2014). Late Paleozoic
1345 assembly of the Alexander-Wrangellia-Peninsular composite terrane, Canadian and Alaskan
1346 Cordillera. *Geological Society of America Bulletin*, 126, 1531–1550.
1347 [https://doi.org/ doi:10.1130/31066.1](https://doi.org/doi:10.1130/31066.1)
1348
1349 Berg, H.C., Jones, D.L., & Richter, D.H. (1972). Gravina-Nutzotin belt — tectonic significance
1350 of an Upper Mesozoic sedimentary and volcanic sequence in southern and southeastern Alaska
1351 (pp. D1–D24). *United States Geological Survey, Professional Paper 800D*.
1352
1353 Bernet, M., & Garver, J.I. (2005). Fission-track analysis of detrital zircon. *Reviews in*
1354 *Mineralogy and Geochemistry*, 58, 205–238. <https://doi.org/10.2138/rmg.2005.58.8>
1355
1356 Bird, K.J., Burruss, R.C., & Pawlewicz, M.J. (1999). Thermal maturity, Chapter VR. In *The oil*
1357 *and gas resource potential of the 1002 area, Arctic National Wildlife Refuge, Alaska*. ANWR
1358 Assessment Team, *United States Geological Survey, Open File Report 98-34*.
1359
1360 Blatt, H. (1992). *Sedimentary Petrology* (2nd Ed.). W H Freeman & Co.: San Francisco.
1361
1362 Blenkinsop, T.G. (1988). Definition of low-grade metamorphic zones using illite crystallinity.
1363 *Journal of Metamorphic Geology*, 6, 623–636. <https://doi.org/10.1111/j.1525->
1364 [1314.1988.tb00444.x](https://doi.org/10.1111/j.1525-1314.1988.tb00444.x)
1365

1366 Boggs, S., Jr. (2009). *Petrology of sedimentary rocks* (2nd Ed.). Cambridge University Press,
1367 Cambridge, UK.

1368

1369 Boles, J.R., & Coombs, D.S. (1975). Mineral reactions in zeolite Triassic tuff, Hokonui Hills,
1370 New Zealand. *Geological Society of America Bulletin*, 86, 163–173.

1371 [https://doi.org/10.1130/0016-7606\(1975\)86<163:MRIZTT>2.0.CO;2](https://doi.org/10.1130/0016-7606(1975)86<163:MRIZTT>2.0.CO;2)

1372

1373 Bond, G.C., & Kominz, M.A. (1984). Construction of tectonic subsidence curves for the early
1374 Paleozoic miogeocline, southern Canadian Rocky Mountains: Implications for subsidence
1375 mechanisms, age of breakup, and crustal thinning. *Geological Society of America Bulletin*, 95,

1376 155–173. [https://doi.org/10.1130/0016-7606\(1984\)95%3C155:COTSCF%3E2.0.CO;2](https://doi.org/10.1130/0016-7606(1984)95%3C155:COTSCF%3E2.0.CO;2)

1377

1378 Bousquet, R., Oberhänsli, R., Goffé, B., Wiederkehr, M., Koller, F., Schmid, S.M., Schuster, R.,
1379 Engi, M., Berger, A., & Martinotti, G. (2008). Metamorphism of metasediments at the scale of
1380 an orogen: a key to the Tertiary geodynamic evolution of the Alps. In S. Siegesmund, B.

1381 Fugenschuh & N. Froitzheim (Eds.), *Tectonic aspects of the Alpine-Dinaride-Carpathian system*
1382 (pp.393–411). *Geological Society, London, Special Publications*, 298.

1383 <https://doi.org/10.1144/SP298.18>

1384

1385 Brew, D.A., & A.B. Ford (1983). Comment on "Tectonic accretion and the origin of the two
1386 major metamorphic and plutonic belts in the Canadian Cordillera". *Geology*, 11, 427–428.

1387

1388 Brew, D.A., & Ford, A.B., (1998), The Coast Mountains structural zones in southeastern Alaska;
1389 descriptions, relations, and lithotectonic terrane significance. In J.E. Gray, J.E. & J.R. Riehle
1390 (Eds.), *Geologic studies in Alaska by the United States Geological Survey, 1996* (pp. 183–192).
1391 *United States Geological Survey, Professional Paper 1595.*

1392

1393 Brew, D.A., & Morrell, R.P. (1983). Intrusive rocks and plutonic belts in southeastern Alaska,
1394 U.S.A. In J.A. Roddick (Ed.), *Circum-Pacific plutonic terranes* (pp. 171–193). *Geological*
1395 *Society of America, Memoir 159.* Geological Society of America.

1396

1397 Burkhard, M. (1993). Calcite twins, their geometry, appearance and significance as stress-strain
1398 markers and indicators of tectonic regime: a review. *Journal of Structural Geology*, 15 (3-5),
1399 351–368. [https://doi.org/10.1016/0191-8141\(93\)90132-T](https://doi.org/10.1016/0191-8141(93)90132-T)

1400

1401 Caddick, M.J., & Thompson A.B. (2008). Quantifying the tectono-metamorphic evolution of
1402 pelitic rocks from a wide range of tectonic settings: mineral compositions in equilibrium.
1403 *Contributions to mineralogy and Petrology*, 156, 177–195. [https://doi.org/10.1007/s00410-008-](https://doi.org/10.1007/s00410-008-0280-6)
1404 [0280-6](https://doi.org/10.1007/s00410-008-0280-6)

1405

1406 Canil, D., Johnston, S.T., D'Souza, R.J., & Heaman, L.M. (2015). Protolith of ultramafic rocks
1407 in the Kluane Schist, Yukon, and implications for arc collisions in the norther Cordillera.
1408 *Canadian Journal of Earth Sciences*, 52, 431–443. <https://doi.org/10.1139/cjes-2014-0138>

1409

1410 Caravaca, G., Brayard, A., Vennin, E., Guiraud, M., Le Pourhiet, L., Grosjean, A.-S., Escaguel,
1411 G., Bylund, K.G., Jenks, J.F., and Stephen, D.A. (2017). Controlling factors for differential
1412 subsidence in the Sonoma Foreland basin (Early Triassic, western USA). *Geological Magazine*,
1413 155(6), 1305–1329. <https://doi.org/10.1017/S0016756817000164>
1414

1415 Chardon, D., Andronicos, C.L., & L.S. Hollister (1999). Large-scale shear zone patterns and
1416 displacements within magmatic arcs: The Coast Plutonic Complex, British Columbia. *Tectonics*,
1417 18, 278–292. <https://doi.org/10.1029/1998TC900035>
1418

1419 Chen, Y., Gu, Y.J., Currie, C.A., Johnston, S.T., Hung, S.-H., Schaffer, A.J., & Audet, P. (2019).
1420 Seismic evidence for a mantle suture and implications for the origin of the Canadian Cordillera.
1421 *Nature Communications*, 1–8. <https://doi.org/10.1038/s41467-019-09084-8>
1422

1423 Clague, J.J. (1979). The Denali fault system in southwest Yukon Territory — A geologic hazard?
1424 In *Current research part A* (pp. 169–178). *Geological Survey of Canada, Paper 79-1A*
1425

1426 Clift, P.D., Draut, A.E., Kelemen, P.B., Blusztajn, J., & Greene, A. (2005). Stratigraphic and
1427 geochemical evolution of an oceanic arc upper crustal section: the Jurassic Talkeetna Volcanic
1428 Formation, south-central Alaska. *Geological Society of America Bulletin*, 117, 902–925.
1429 <https://doi.org/10.1130/B25638.1>
1430

1431 Cohen, H.A. (1992). *Stratigraphic, sedimentologic, and provenance constraints on the evolution*
1432 *of the Gravina belt, northern southeast Alaska* (Doctoral dissertation). Princeton, New Jersey:
1433 Princeton University.

1434

1435 Cohen, H.A., Hall, C.M., & Lundberg, N. (1995). $^{40}\text{Ar}/^{39}\text{Ar}$ dating of detrital grains constrains
1436 the provenance and stratigraphy of the Gravina belt, southeastern Alaska. *Journal of Geology*,
1437 103, 327–337. <https://doi.org/10.1086/629750>

1438

1439 Cohen, H.A., & Lundberg, N. (1993). Detrital record of the Gravina arc, southeastern Alaska:
1440 petrology and provenance of Seymour Canal Formation sandstones. *Geological Society of*
1441 *America Bulletin*, 105: 1400–1414. [https://doi.org/10.1130/0016-7606\(1993\)1052.3.CO;2](https://doi.org/10.1130/0016-7606(1993)1052.3.CO;2)

1442

1443 Crawford, M.L., Hollister, L.S., & Woodsworth, G.J. (1987). Crustal deformation and regional
1444 metamorphism across a terrane boundary, Coast Plutonic complex, British Columbia. *Tectonics*,
1445 6(3), 343–361. <https://doi.org/10.1029/TC006i003p00343>

1446

1447 Dalrymple, R.W., 2010. Interpreting Sedimentary Successions: Facies, Facies Analysis and
1448 Facies Models. In N.P. James & R.W. Dalrymple (Eds.), *Facies models 4* (pp. 3–18). *Geological*
1449 *Association of Canada*. St John's, Newfoundland: Geological Association of Canada.

1450

1451 Dickinson, W.R., Beard, L.S., Brakenridge, G.R., Erjavec, J.L., Ferguson, R.C., Inman, K.F., et
1452 al. (1983). Provenance of North American Phanerozoic sandstones in relation to tectonic setting.

1453 *Geological Society of America Bulletin*, 94, 222–235. <https://doi.org/10.1130/0016->
1454 [7606\(1983\)942.0.CO;2](https://doi.org/10.1130/0016-7606(1983)942.0.CO;2)
1455
1456 Dickinson, W.R., & Suczek, C.A. (1979). Plate tectonics and sandstone compositions. *American*
1457 *Association of Petroleum Geologists Bulletin*, 63, 2164–2182.
1458 <https://doi.org/10.1306/2F9188FB-16CE-11D7-8645000102C1865D>
1459
1460 Dodds, C.J., & R.B. Campbell (1988). Potassium-argon ages of mainly intrusive rocks in the
1461 Saint Elias Mountains, Yukon and British Columbia. *Geological Survey Canada, Paper 87-16*.
1462
1463 Dodds, C.J., & Campbell, R.B. (1992a). Overview, legend and mineral deposit tabulations for
1464 Geology of southwest Kluane Lake map area (115G and F[E1/2]), Yukon Territory, Open File
1465 2188; Geology of Mount St. Elias map area (115B and C[E1/2]), Yukon Territory, Open File
1466 2189; Geology of southwest Dezadeash map area (115A), Yukon Territory, Open File 2190; and
1467 Geology of northeast Yakutat Map Area (114O) and Tatshenshini River (114 P) map areas.
1468 *Geological Survey of Canada, Open File 2191*.
1469
1470 Dodds, C.J., & Campbell, R.B. (1992b). Geology, SW Dezadeash map area [115A], Yukon
1471 Territory. *Geological Survey of Canada, Open File 2190*. <https://doi.org/10.4095/133476>
1472
1473 Dodds, C.J., & Campbell, R.B. (1992c). Geology, SW Kluane Lake map area [115G & F[E
1474 1/2]], Yukon Territory. *Geological Survey of Canada, Open File 2188*.
1475 <https://doi.org/10.4095/133474>

1476

1477 Doglioni, C., Harabaglia, P., Merlini, S., Mongelli, F., Peccerillo, A. & Piromallo, C.

1478 (1999): Orogens and slabs vs their direct of subduction. *Earth Science Reviews*, 45, 167–208.

1479 [https://doi.org/10.1016/S0012-8252\(98\)00045-2](https://doi.org/10.1016/S0012-8252(98)00045-2)

1480

1481 Dusel-Bacon, C., Csejtey, B., Jr., & Foster, H.L. (1993). Distribution, facies, ages, and proposed

1482 tectonic associations of regionally metamorphosed rocks in east- and south-central Alaska.

1483 *United States Geological Survey, Professional Paper 1497-C.*

1484 <https://pubs.er.usgs.gov/publication/pp1497C>

1485

1486 Eisbacher, G.H. (1976). Sedimentology of the Dezadeash flysch and its implications for strike-

1487 slip faulting along the Denali fault, Yukon Territory and Alaska. *Canadian Journal of Earth*

1488 *Sciences*, 13, 1495–1513. <https://doi.org/10.1139/e76-157>

1489

1490 Eisbacher G.H. (1985). Pericollisional strike-slip faults and synorogenic basins, Canadian

1491 Cordillera. In K.T. Biddie and N. Christie-Blick (Eds.), *Strike-Slip Deformation, Basin*

1492 *Formation, and Sedimentation* (pp. 265–282). *Special Publication of the Society of Economic*

1493 *Paleontologists and Mineralogists* 37.

1494

1495 Enkelmann, E., Piestrzeniewicz, A., Falkowski, S., & Stübner, K. (2017). Thermochemistry in

1496 southeast Alaska and southwest Yukon: implications for North American plate response to

1497 terrane accretion. *Earth and Planetary Science Letters*, 457, 348–358.

1498 <https://doi.org/10.1016/j.epsl.2016.10.032>

1499

1500 Epstein, A.G., Epstein, J.B., & Harris, L.D. (1977). Conodont Color Alteration Index to Organic
1501 Metamorphism. *United States Geological Survey, Professional Paper 995*.

1502

1503 Essene, E.J. (1989). The current status of thermometry in metamorphic rocks. In J.S. Daly, R.A.
1504 Cliff, & B.W.D. Yardley (Eds.), *Evolution of metamorphic belts* (pp. 1–44). *Geological Society
1505 of America Special Publication 43*.

1506

1507 Falkowski, S., & Enkelmann, E. (2016). Upper-crustal cooling of the Wrangellia composite
1508 terrane in the northern St. Elias Mountains, western Canada. *Lithosphere*, 8(4), 359–378.
1509 <https://doi.org/10.1130/L508.1>

1510

1511 Frey, M. (1987). Very low-grade metamorphism of clastic sedimentary rocks. In M. Frey (Ed.),
1512 *Low temperature metamorphism* (pp. 9–58). Blackie & Sons Ltd.: Bishopbriggs, Glasgow.

1513

1514 Frey, M., de Capitani, C., & Liou, J.G. (1991). A new petrogenetic grid for low-grade
1515 metabasites. *Journal of Metamorphic Geology*, 9, 497–509. [https://doi.org/10.1111/j.1525-
1516 1314.1991.tb00542.x](https://doi.org/10.1111/j.1525-1314.1991.tb00542.x)

1517

1518 Frey, M., & Kisch. HJ. (1987). Scope of subject. In M. Frey (Ed.), *Low temperature
1519 metamorphism* (pp. 1-8). Blackie and Son Ltd.: Bishopbriggs, Glasgow.

1520

1521 Fu, R.R., Kent, D.V., Hemming, S.R., Gutierrez, P., & Creveling, J.R. (2020). Testing the
1522 occurrence of Late Jurassic true polar wander using the La Negra volcanics of northern Chile.
1523 *Earth and Planetary Science Letters*, 529, 1–10. <https://doi.org/10.1016/j.epsl.2019.115835>

1524

1525 Gallagher, K. (1989). An examination of some uncertainties associated with estimates of
1526 sedimentation rates and tectonic subsidence. *Basin Research*, 2(93), 97–114.
1527 <https://doi.org/10.1111/j.1365-2117.1989.tb00029.x>

1528

1529 García-López, S., Bastida, F., Aller., J., & and Sanz-López, J. (2001). Geothermal
1530 palaeogradients and metamorphic zonation rom the conodont colour alteration index (CAI).
1531 *Terra Nova*, 13, 79–83. <https://doi.org/10.1046/j.1365-3121.2001.00328.x>

1532

1533 Gehrels, G.E. (2000). Reconnaissance geology and U-Pb geochronology of the western flank of
1534 the Coast Mountains between Juneau and Skagway, southeastern Alaska. In H.H. Stowell &
1535 W.C. McClelland (Eds.), *Tectonics of the Coast Mountains, Southeastern Alaska and British*
1536 *Columbia, Geological Society of America Special Paper 343* (pp. 213–233). Boulder, Colorado:
1537 Geological Society of America. <https://doi.org/10.1130/0-8137-2343-4.213>

1538

1539 Gehrels, G.E., & Berg, H.C. (1994). Geology of southeastern Alaska. In G. Plafker, & H.C. Berg
1540 (Eds.), *The Geology of Alaska* (pp. 451–576). *Geological Society of America, Vol. G-1*. Boulder,
1541 Colorado: The Geology of North America. <https://doi.org/10.1130/DNAG-GNA-G1.451>

1542

1543 Gehrels, G.E., McClelland, W.C., & Yokelson, I. (2017). Reply to “Comment on U-Pb and Hf
1544 isotope analysis of detrital zircons from Mesozoic strata of the Gravina belt, southeast Alaska”
1545 by Yokelson et al. (2015). *Tectonics*, 36, 2741–2743. <https://doi.org/10.1002/2017TC004735>
1546

1547 Gehrels, G.E., Rusmore, M., Woodsworth, G., Crawford, M., Andronicos, C., Hollister, L., et al.
1548 (2009). U–Th–Pb geochronology of the Coast Mountains batholith in north coastal British
1549 Columbia: Constraints on age and tectonic evolution. *Geological Society of America Bulletin*,
1550 121, 1341–1361. <https://doi.org/10.1130/B26404.1>
1551

1552 Geisler, D., Gehrels, Pech, M., White, C., Yokelson, I. G.E., & McClelland (2016). Canadian
1553 *Journal of Earth Sciences*, 53, 979–992. <https://doi.org/10.1139/cjes-2015-0240>
1554

1555

1556 Greene, A.R., Scoates, J.S., Weis, D., Katvala, E.C., Israel, C., & Nixon, G.T. (2010). The
1557 architecture of oceanic plateaus revealed by the volcanic stratigraphy of the accreted Wrangellia
1558 oceanic plateau. *Geosphere*, 6, 47–73. <https://doi.org/10.1130/GES00212.1>
1559

1560 Hampton, B.A., Ridgway, K.D., & Gehrels, G.E. (2010). A detrital record of Mesozoic island arc
1561 accretion and exhumation in the North American Cordillera: U–Pb geochronology of the
1562 Kahiltna basin, southern Alaska. *Tectonics*, 29, 1–21. <https://doi.org/10.1029/2009TC002544>
1563

1564 Hancock, P.L. (1982). Distinction between cleavage and joint using fracture separation. In G.J.
1565 Borradaile, M.B. Baly, & C. McA. Powell (Eds.), *Atlas of deformational and metamorphic rock*
1566 *fabrics* (pp.186–187). Springer-Verlag: New York, New York.

1567

1568 Haeussler, P.J. (1992). Structural evolution of an arc-basin: the Gravina belt in central
1569 southeastern Alaska. *Tectonics*, 11(6), 1245–1265. <https://doi.org/10.1029/92TC01107>

1570

1571 Harris, A.G., & Sweet, W.C. (1989). Mechanical and chemical techniques for separating
1572 microfossils from rock, sediment and residue matrix. In R.M. Feldmann, R.E. Chapman, and J.T.
1573 Hannibal (Eds.), *Paleotechniques* (pp. 70–86). *Paleontological Society Special Publication 4*.
1574 Bethesda, Maryland: Paleontological Society. <https://doi.org/10.1017/S2475262200005013>

1575

1576 Hartkopf-Fröder, C., Königshof, P., Littke, R., & Schwarzbauer, J. (2015). Optical thermal
1577 maturity parameters and organic geochemical alteration at low grade diagenesis to
1578 anchimetamorphism: A review. *International journal of Coal Geology*, 150-151, 74–119.
1579 <https://doi.org/10.1016/j.coal.2015.06.005>

1580

1581 Héroux, Y., Chagnon, A., & Bertrand, R. (1979). Compilation and correlation of major
1582 maturation indicators. *American Association of Petroleum Geologists Bulletin*, 63, 12, 2128–
1583 2144.

1584

1585 Hietpas, J., Samson, S.D., & Moecher, D.P. (2010). Recovering tectonic events from the
1586 sedimentary record: Detrital monazite plays in high fidelity. *Geology*, 38(2), 167–170.

1587 <https://doi.org/10.1130/G30265.1>

1588

1589 Hildebrand, R.S. (2013). Mesozoic assembly of the North American Cordillera. *Geological*
1590 *Society of America Special Paper 495*. Boulder, Colorado: Geological Society of America.

1591 <https://doi.org/10.1130/SPE495>

1592

1593 Himmelberg, G.R., Brew, D.A., & Ford, A.B. (1995). Low-grade M1 metamorphism of the
1594 Douglas Island Volcanics, western metamorphic belt near Juneau. In P. Schiffman & H.W. Day
1595 (Eds.), Low-grade metamorphism of mafic rocks (pp. 51–66). *Geological Society of America,*
1596 *Special Paper 296*. Boulder, Colorado: Geological Society of America.

1597 <https://doi.org/10.1130/SPE296-p51>

1598

1599 Hudson, T. L. (1983) Calc-alkaline plutonism along the Pacific rim of southern Alaska. In J.A.
1600 Roddick (Ed.). Circum-Pacific Plutonic Terranes (pp. 159–169). *Geological Society of America,*
1601 *Memoir 159*.

1602

1603 Huff, W.D. (2016). K-bentonites: A review. *American Mineralogist*, 101,43–70.

1604 <https://doi.org/10.2138/am-2016-5339>

1605

1606 Ibañez-Mejia, M., Pullen, A., Pepper, M., Urbani., F., Ghoshal, G., & Ibañez-Mejia, J.C. (2018).
1607 Use and abuse of detrital zircon U-Pb geochronology— A case from the Río Orinoco delta,
1608 eastern Venezuela. *Geology*, 46, 1–4. <https://doi.org/10.1130/G45596.1>

1609

1610 Ingram, G. M., & Hutton, D. H. W. (1994). The Great Tonalite Sill: Emplacement into a
1611 contractional shear zone and implications for Late Cretaceous to early Eocene tectonics in
1612 southeastern Alaska and British Columbia. *Bulletin of the Geological Society of America*, 106,
1613 715–728.

1614

1615 Jarvie, D. (2018). Correlation of Tmax and measured vitrinite reflectance. Accessed August 18,
1616 2019.

1617 [https://www.wildcattechnologies.com/application/files/9915/1689/1979/Dan_Jarvie_Correlation](https://www.wildcattechnologies.com/application/files/9915/1689/1979/Dan_Jarvie_Correlation_of_Tmax_and_measured_vitrinite_reflectance.pdf)
1618 [_of_Tmax_and_measured_vitrinite_reflectance.pdf](https://www.wildcattechnologies.com/application/files/9915/1689/1979/Dan_Jarvie_Correlation_of_Tmax_and_measured_vitrinite_reflectance.pdf)

1619

1620 Johnston, S.T., & Canil, D. (2007). Crustal structure of SW Yukon, northern Cordillera:
1621 implications for crustal growth in a convergent margin orogen. *Tectonics*, 26, 1–18.

1622 <https://doi.org/10.1029/2006TC001950>

1623

1624 Kisch, H.J. (1987). Correlation between indicators of very low-grade metamorphism. In M. Frey
1625 (Ed.), *Low temperature metamorphism* (pp. 227-300). Blackie & Sons Ltd.: Bishopbriggs,
1626 Glasgow.

1627

1628 Kisch, H.J. (1991). Illite crystallinity: recommendations on sample preparation, X-ray diffraction
1629 settings, and interlaboratory samples. *Journal of Metamorphic Geology*, 9(6), 665–670.

1630 <https://doi.org/10.1111/j.1525-1314.1991.tb00556.x>

1631

1632 Klepeis, K.A., M.L. Crawford, & G. Gehrels (1998). Structural history of the crustal-scale Coast
1633 shear zone north of Portland, southeast Alaska and British Columbia. *Journal of Structural*
1634 *Geology*, 20, 883–904. [https://doi.org/10.1016/S0191-8141\(98\)00020-0](https://doi.org/10.1016/S0191-8141(98)00020-0)
1635

1636 Koesoemadinata, R.P., Samuel, L., & Tachjudin, M.I. (1995). Subsidence curves and modelling
1637 of some Indonesian Tertiary basins. *Geological Society of Malaysia Bulletin* 37, 205–230.
1638 <https://doi.org/10.1306/A25FE711-171B-11D7-8645000102C1865D>
1639

1640 Kozinski, J. (1985). *Sedimentology and tectonic significance of the Nutzotin mountains*
1641 *sequence, Alaska* (Master's thesis). Albany, New York: State University of New York.
1642

1643 Lafargue, E., Marquis, F., & Pillot, D. (1998) Rock-Eval 6 applications in hydrocarbon
1644 exploration, production, and soil contamination studies. *Oil & gas Science and technology —*
1645 *Rev. IFP*, 53(4), 421–437. <https://doi.org/10.2516/ogst:1998036>
1646

1647 Langford, F.F., & Blanc-Valleron, M. -M. (1990). Interpreting rock-eval pyrolysis data using
1648 graphs of pyrolizable hydrocarbons vs. total organic carbon. *American Association of Petroleum*
1649 *Geologists Bulletin*, 74(6), 799–804.
1650 <https://doi.org/10.1306/0C9B238F-1710-11D7-8645000102C1865D>
1651

1652 Lanthram, E.H., Pomeroy, J.S., Berg, H.C., & Loney, R.A. (1965). Reconnaissance Geology of
1653 Admiralty Island Alaska. *United States Geological Survey, Bulletin* 1181-R.
1654

1655 Leloup, P.H., Ricard, Y., Battaglia, J., & Lacassin, R. (1999). Shear heating in continental strike-
1656 slip shear zones: Model and field examples. *Geophysical Journal International*, 136, 19–40.
1657 <https://doi.org/10.1046/j.1365-246X.1999.00683.x>
1658
1659 Liou, J.G., (1970). Synthesis and stability relations of wairakite, $\text{CaAl}_2\text{Si}_4\text{O}_{12}\cdot 2\text{H}_2\text{O}$.
1660 *Contributions to Mineralogy and Petrology*, 27, 259–282. <https://doi.org/10.1007/BF00389814>
1661
1662 Liou, J.G. (1971). Synthesis and stability relations of prehnite, $\text{Ca}_2\text{Al}_2\text{Si}_3\text{O}_{10}(\text{OH})_2$. *The*
1663 *American Mineralogist*, 56, 507–531.
1664
1665 Liou, J.G., Maruyama, S., & Cho, M. (1987). Very low-grade metamorphism of volcanic and
1666 volcanoclastic rocks- mineral assemblages and mineral facies. In M. Frey (Ed.), *Low temperature*
1667 *metamorphism* (pp. 59–113). Blackie & Sons Ltd.: Bishopbriggs, Glasgow.
1668
1669 Lowey, G.W. (1980). *Depositional themes in a turbidite succession, Dezadeash Formation*
1670 *(Jura–Cretaceous), Yukon* (Master’s thesis). Calgary, Alberta: University of Calgary.
1671
1672 Lowey, G.W. (1992). Variation in bed thickness in a turbidite succession, Dezadeash Formation
1673 (Jurassic–Cretaceous), Yukon, Canada: Evidence of thinning-upward and thickening-upward
1674 cycles. *Sedimentary Geology*, 78, 217–232. [https://doi.org/10.1016/0037-0738\(92\)90021-I](https://doi.org/10.1016/0037-0738(92)90021-I)
1675
1676 Lowey, G.W. (1998). A new estimate of the amount of displacement on the Denali Fault system
1677 based on the occurrence of carbonate megaboulders in the Dezadeash Formation (Jura-

1678 Cretaceous), Yukon, and the Nutzotin Mountains sequence (Jura–Cretaceous), Alaska. *Bulletin*
1679 *of Canadian Petroleum Geology*, 46, 379–386. <https://doi.org/10.35767/gscpgbull.46.3.379>
1680

1681 Lowey, G.W. (2000). The Tatshenshini shear zone (new) in southwestern Yukon,
1682 Canada: Comparison with the Coast shear zone in British Columbia and southeastern Alaska and
1683 implications regarding the Shakwak suture. *Tectonics*, 19(3), 512–528.
1684 <https://doi.org/10.1029/1999TC001119>
1685

1686 Lowey, G.W. (2007). Lithofacies analysis of the Dezadeash Formation (Jura– Cretaceous),
1687 Yukon, Canada: The depositional architecture of a mud/sand-rich turbidite system. *Sedimentary*
1688 *Geology*, 198, 273–291. <https://doi.org/10.1016/j.sedgeo.2006.12.011>
1689

1690 Lowey, G.W. (2011). Volcaniclastic gravity flow deposits in the Dezadeash Formation (Jura–
1691 Cretaceous), Yukon, Canada: Implications regarding the tectonomagmatic evolution of the
1692 Chitina arc in the northern Cordillera of North America. *Lithos*, 125, 86–100.
1693 <https://doi.org/10.1016/j.lithos.2011.01.014>
1694

1695 Lowey, G.W. (2017). Comment on “U-Pb and Hf isotope analysis of detrital zircons from
1696 Mesozoic strata of the Gravina belt, southeast Alaska” by Yokelson et al. (2015). *Tectonics*, 36,
1697 2736–2740. <https://doi.org/10.1002/2017TC004507>
1698

1699 Lowey, G.W. (2019). Provenance analysis of the Dezadeash Formation (Jurassic–Cretaceous),
1700 Yukon, Canada: Implications regarding a linkage between the Wrangellia composite terrane and
1701 the western margin of Laurasia. *Canadian Journal of Earth Sciences*, 56(1), 77–10.

1702 <https://doi.org/10.1139/cjes-2017-0244>

1703

1704 MacKevett, E.M., Jr. (1971). Stratigraphy and general geology of the McCathy C-5 Quadrangle,
1705 Alaska. *United States Geological Survey, Bulletin 1323*.

1706 <https://pubs.usgs.gov/bul/1323/report.pdf>

1707

1708 MacKevett, E.M., Jr. (1978). Geologic map of the McCarthy Quadrangle, Alaska. *United States*
1709 *Geological Survey, Map I-1032*. Scale 1:250,000. <https://doi.org/10.3133/i1032>

1710

1711 Manselle, P., Brueseke, M.E., Trop, J.M., Benowitz, J.A., Snyder, D.C., & Hart, W.K. (2020).

1712 Geochemical and stratigraphic analysis of the Chisana Formation, Wrangellia terrane, eastern

1713 Alaska: insights into Early Cretaceous magmatism and tectonism along the northern Cordilleran

1714 margin. *Tectonics*, 39(8), e2020TC006131. <https://doi.org/10.1029/2020TC006131>

1715

1716 Manuszak, J.D. (2000). *Sedimentary and structural record of late Jurassic–early Cretaceous*

1717 *collisional tectonics, Nutzotin and Mentasta Mountains, east-central Alaska* (Master's thesis).

1718 West Lafayette, Indiana: Purdue University.

1719

1720 Manuszak, J.D., & Ridgway, K.D. (2000). Stratigraphic architecture of the Upper Jurassic–

1721 Lower Cretaceous Nutzotin Mountains sequence, Nutzotin and Mentasta Mountains, Alaska. In

1722 *Short Notes on Alaska Geology 1999* (pp. 63–75). *Alaska Division of Geological and*

1723 *Geophysical Surveys, Professional Report 119*.

1724

1725 Manuszak, J.D., Ridgway, K.D., Trop, J.M., & Gehrels, G.E. (2007). Sedimentary record of the
1726 tectonic growth of a collisional continental margin: Upper Jurassic-Lower Cretaceous Nutzotin
1727 Mountains sequence, eastern Alaska Range, Alaska. In K.D. Ridgway, J.M. Trop, J.M.G Glen
1728 and J.M. O'Neill (Eds.), *Tectonic growth of a collisional continental margin: Crustal evolution*
1729 *of southern Alaska* (pp. 345–377). *Geological Society of America Special Paper 431*. Boulder,
1730 Colorado: Geological Society of America. [https://doi.org/10.1130/2007.2431\(14\)](https://doi.org/10.1130/2007.2431(14))

1731

1732 McClelland, W.C., Anovitz, L.M., & Gehrels, G. 1991. Thermobarometric constraints on the
1733 structural evolution of the Coast Mountains batholith, central southeastern Alaska. *Canadian*
1734 *Journal of Earth Sciences*, 28, 912–928. <https://doi.org/10.1139/e91-083>

1735

1736 McClelland, W.C., Gehrels, G.E., and Saleeby, J.B. (1992a). Upper Jurassic-Lower Cretaceous
1737 basinal strata along the Cordilleran margin: implications for the accretionary history of the
1738 Alexander-Wrangellia-Peninsular terrane. *Tectonics*, 11: 823–835.

1739 <https://doi.org/10.1029/92TC00241>

1740

1741 McClelland, W.C., Gehrels, G.E., Samson, S.D., & Patchett, P.J. (1992b). Protolith relations of
1742 the Gravina Belt and Yukon–Tanana terrane in central southeastern Alaska. *Journal of Geology*,
1743 100, 107–123.

1744

1745 McClelland, W.C., Gehrels, G.E., Scott D. Samson, S.D., & Patchett, P.J. (1991). Protolith
1746 Relations of the Gravina Belt and Yukon-Tanana Terrane in Central Southeastern Alaska.
1747 *Journal of Geology*, 100, 107–123. <https://www.jstor.org/stable/30082321>

1748
1749
1750
1751
1752
1753
1754
1755
1756
1757
1758
1759
1760
1761
1762
1763
1764
1765
1766
1767
1768
1769
1770

McClelland, W. C., & Mattinson, J. M. (2000), Cretaceous-Tertiary evolution of the western Coast Mountains, central southeastern Alaska. In H.H. Stowell & W.C. McClelland (Eds.), *Tectonics of the Coast Mountains, Southeastern Alaska and British Columbia* (pp. 159–182). *Geological Society of America Special Paper 343*. Boulder, Colorado: Geological Society of America. <https://doi.org/10.1130/0-8137-2343-4.159>

McDermott, R.G., Ault, A.K., Caine, J.S., & Thompson, S.N. (2019). Thermotectonic history of the Kluane ranges and evolution of the eastern Denali fault zone in southwestern Yukon, Canada. *Tectonics*, 38, 2983–3010. <https://doi.org/10.1029/2019TC005545>

McMillan, R., & Golding, M. (2019). Thermal maturity of carbonaceous material in conodonts and the Color Alteration Index: independently identifying maximum temperature with Raman spectroscopy. *Palaeogeography, Palaeoclimatology, Palaeoecology*, 534, 1–11. <https://doi.org/10.1016/j.palaeo.2019.109290>

McSween, H.Y., Labotka, T.C., & Viviano-Beck, C.E. (2015). Metamorphism in the Martian crust. *Meteoritics & Planetary Science* 50, Nr 4, 590–603. <https://doi.org/10.1111/maps.12330>

Merriman, R.J. (2002). Contrasting clay mineral assemblages in British Lower Paleozoic slate belts: The influence of geotectonic setting. *Clay Minerals*, 37, 207–219.

<http://doi.org/10.1180/0009855023720041>

1771 Merriman, R.J. (2005). Clay minerals and sedimentary basin history. *European Journal of*
1772 *Mineralogy*, 17, 7–20. <https://doi.org/10.1127/0935-1221/2005/0017-0007>
1773

1774 Merriman, R.J., & Frey, M. (1999). Patterns of very low-grade metamorphism in metapelitic
1775 rocks. In M. Frey, & D. Robinson (Eds.), *Low-grade metamorphism* (pp. 61–107). Blackwell
1776 Science Ltd.: Osney Mead, Oxford. <https://doi.org/10.1002/9781444313345.ch3>
1777

1778 Merriman, R.J., & Peacor, D.R. (1999). Very low-grade metapelites: mineralogy, microfabrics
1779 and measuring reaction progress. In M. Frey, & D. Robinson (Eds.), *Low-grade metamorphism*
1780 (pp. 10–60). Blackwell Science Ltd.: Osney Mead, Oxford.
1781 <https://doi.org/10.1002/9781444313345.ch2>
1782

1783 Meunier, A., Velde, B., & Zalba, P. (2004). Illite K–Ar dating and crystal growth processes in
1784 diagenetic environments: A critical review. *Terra Nova*, 16, 296–304.
1785 <https://doi.org/10.1111/j.1365-3121.2004.00563.x>
1786

1787 Mezger, J.E. (1997). *Tectonometamorphic evolution of the Kluane metamorphic assemblage, SW*
1788 *Yukon: Evidence for Late Cretaceous eastward subduction of oceanic crest underneath North*
1789 *America* (Doctoral dissertation). Edmonton, Alberta: University of Alberta.
1790

1791 Mezger, J.E., Chacko, T., & Erdmer, P. (2001a). Metamorphism at a late Mesozoic accretionary
1792 margin: a study from the Coast Belt of the North American Cordillera. *Journal of Metamorphic*
1793 *Geology*, 19, 121–137. <https://doi.org/10.1046/j.0263-4929.2000.00300.x>

1794

1795 Mezger, J.E., Creaser, R.A., Erdmer, P., & Johnston, S.T. (2001b). A Cretaceous back-arc basin
1796 in the Coast Belt of the northern Canadian Cordillera: Evidence from geochemical and
1797 neodymium isotope characteristics of the Kluane metamorphic assemblage, southwest Yukon.
1798 *Canadian Journal of Earth Sciences*, 38, 91–103. <https://doi.org/10.1139/e00-076>

1799

1800 Miller, T.P., 1994. Pre-Cenozoic plutonic rocks in mainland Alaska. In: G. Plafker & H.C. Berg,
1801 (Eds.), *The Geology of Alaska* (pp. 535–554). *Geological Society of America, Geology of North*
1802 *America, Vol. G-1*. Geological Society of America.

1803

1804 Moecher, D.P., & Sampson, S.D. (2006). Differential zircon fertility of source terranes and
1805 natural bias in the detrital zircon record: Implications for sedimentary provenance analysis.
1806 *Earth and Planetary Science Letters*, 247(3), 252–266.
1807 <https://doi.org/10.1016/j.epsl.2006.04.035>

1808

1809 Monger, J.W.H. (2014). Logan medallist 1. Seeking the suture: The Coast–Cascade conundrum.
1810 *Geoscience Canada*, 41, 379–398. <https://doi.org/10.12789/geocanj.2014.41.058>

1811

1812 Monger, J.W.H., & Journeay, J.M. (1994). Guide to the geology and tectonic evolution of the
1813 southern Coast Mountains. *Geological Survey of Canada, Open File 2490*.

1814

1815 Monger, J.W.H., & Nokleberg, W.J. (1996), Evolution of the northern North American
1816 Cordillera: Generation, fragmentation, displacement and accretion of successive North American

1817 plate-margin arcs. In A.R. Coyner & P.L. Fahey (Eds.), *Geology and Ore Deposits of the*
1818 *American Cordillera* (pp. 1133–1152). *Geological Society of Nevada, Symposium Proceedings*
1819 *Vol. III.*

1820

1821 Monger, J.W.H., & Price, R. (2002). The Canadian Cordillera: Geology and tectonic evolution.
1822 *CSEG Recorder*, 17, 18–36.

1823

1824 Monger, J.W.H., Price, R.A., & Tempelman-Kluit, D.J. (1982). Tectonic accretion and the origin
1825 of the two major metamorphic and plutonic belts in the Canadian Cordillera. *Geology*, 10, 70–
1826 75. [https://doi.org/10.1130/0091-7613\(1982\)102.0.CO;2](https://doi.org/10.1130/0091-7613(1982)102.0.CO;2)

1827

1828 Monger, J.W.H., van der Heyden, P., Journeay, J.M., Evenchick, C.A., & Mahoney, J.B. (1994).
1829 Jurassic–Cretaceous basins along the Canadian Coast Belt: Their bearing on pre-mid-Cretaceous
1830 sinistral displacements. *Geology*, 22, 175–178. [https://doi.org/10.1130/0091-](https://doi.org/10.1130/0091-7613(1994)0222.3.CO;2)
1831 [7613\(1994\)0222.3.CO;2](https://doi.org/10.1130/0091-7613(1994)0222.3.CO;2)

1832

1833 Moore, J.C. and Connelly, W. (1979). Tectonic history of the continental margin of southwestern
1834 Alaska, Late Triassic to earliest Tertiary. In A. Sisson (Ed.), *The Relationship of Plate Tectonics*
1835 *to Alaskan Geology and Resources* (pp. H1-H29). Alaska Geological Society: Anchorage,
1836 Alaska.

1837

1838 Mullis, J., Mählmann, R.F., & Wolf, M. (2017). Fluid inclusion microthermometry to calibrate
1839 vitrinite reflectance (between 50 and 270 °C), illite Kübler-index data and the

1840 diagenesis/anchizone boundary in the external part of the Central Alps. *Applied Clay Science*,
1841 143, 307–319. <https://doi.org/10.1016/j.clay.2017.03.023>
1842
1843 Munsell Color (1994). *Munsell Soil Color Charts* (Revised Edition). Windsor, New York:
1844 Macbeth Division of Kollmogen Instruments Corporation.
1845
1846 Nelson, J.L., Colpron, M., & Israel, D. (2013). The cordillera of British Columbia, Yukon, and
1847 Alaska: tectonics and metallogeny. In N. Colpron, T. Bissig, B.G. Rusk, & J.F.H. Thompson
1848 (Eds.), *Tectonics, metallogeny, and discovery: The North American cordillera and similar*
1849 *accretionary settings* (pp. 53–110). *Special Publications of the Society of Economic Geologists*,
1850 *Vol. 17*. Society of Economic Geologists: Littleton, Colorado. <https://doi.org/10.5382/SP.17.03>
1851
1852 Neuhoff, P.S., & Bird, D.K. (2001). Partial dehydration of laumontite: Thermodynamic
1853 constraints and petrogenetic implications. *Mineralogical Magazine*, 65(1), 59–70.
1854 <https://doi.org/10.1180/002646101550127>
1855
1856 Nokleberg, W.J., Jones, D.L., & Silberling, N.J. (1985). Origin and tectonic evolution of the
1857 Maclaren and Wrangellia terranes, eastern Alaska Range, Alaska. *Geological Society of America*
1858 *Bulletin*, 96, 1251–1270. [https://doi.org/10.1130/0016-7606\(1985\)962.0.CO;2](https://doi.org/10.1130/0016-7606(1985)962.0.CO;2)
1859
1860 Nokleberg, W.J., Parfenov, W.J., Monger, J.W.H., Norton, I.O., Khanchuk, A.I., Stone, D.B.,
1861 Scotese, C.R., Scholl, D.W., & Fujita, K. (2000). Phanerozoic Tectonic Evolution of the Circum-
1862 North Pacific. *United States Geological Survey, Professional Paper 1626*.

1863

1864 Nokleberg, W.J., Plafker, G., & Wilson, F.H. (1994). Geology of south-central Alaska. In G.
1865 Plafker, & H.C. Berg (Ed.), *The Geology of Alaska* (pp. 311–366). *Geological Society of*
1866 *America, Geology of North America, Vol. G-1*. Geological Society of America: Boulder,
1867 Colorado. <https://doi.org/10.1130/DNAG-GNA-G1.311>

1868

1869 Ogg, J.G., Ogg, G., & F. M. Gradstein, F.M. (2016). *A Concise Geologic Time Scale: 2016*.
1870 Elsevier: New York. New York.

1871

1872 Orchard, M.J., & Forster, P.J.L. (1991). Conodont color and thermal maturity of the Late
1873 Triassic Kunga Group, Queen Charlotte Islands, British Columbia. In *Evolution and*
1874 *hydrocarbon potential of the Queen Charlotte Basin, British Columbia* (pp. 453–464).
1875 *Geological Survey of Canada, Paper 90-10*. <https://doi.org/10.4095/131983>

1876

1877 Painter, C.S., & Carrapa, B. (2013). Flexure versus dynamic processes of subsidence in the
1878 North American Cordillera foreland basin. *Geophysical Research Letters*, 40, 4242–4253.
1879 <https://doi.org/10.1002/grl.50831>

1880

1881 Parra, M., Jaramillo, C., Strecker, M.R., Sobel, E.R., Quiroz, L., Rueda, M., & Torres, V. (2009).
1882 Orogenic wedge advance in the northern Andes: Evidence from the Oligocene-Miocene
1883 sedimentary record of the medina basin, eastern Cordillera, Columbia. *Geological Society of*
1884 *America Bulletin*, 121(5/6), 780–800. <https://doi.org/10.1130/B26257.1>

1885

1886 Passchier, C.W., & Trouw, R.A.J. 1996. *Micro-tectonics*. Springer-Verlag: New York, New
1887 York.
1888

1889 Pavlis, T.L., Amato, J.M., Trop, J.M., Ridgway, K.D., Roeske, S.M., & Gehrels, G.E. (2019).
1890 Subduction polarity in ancient arcs: a call to integrate geology and geophysics to decipher the
1891 Mesozoic tectonic history of the Northern Cordillera of North America. *Geological Society of*
1892 *America Today*, 29. <https://doi.org/10.1130/GSATG3402A.1>
1893

1894 Pavlis, T.L., & Roeske, S.M. (2007). The Border Ranges fault system, southern Alaska, In K.D.
1895 Ridgway, J.M. Trop, J.M.G. Glen, & J.M. O'Neill (Eds.), *Tectonic growth of a collisional*
1896 *continental margin: Crustal evolution of Southern Alaska* (pp. 95–127). *Geological Society of*
1897 *America Special Paper 431*. Boulder, Colorado: Geological Society of America.
1898 [https://doi.org/10.1130/2007.2431\(05\)](https://doi.org/10.1130/2007.2431(05))
1899

1900 Peacock, S.M. (1996). Thermal and petrologic structure of subduction zones. In G.E. Bebout,
1901 D.W. Scholl, S.H. Kirby & J.P. Platt, (Eds.), *Subduction top to bottom, Geophysical Monograph*
1902 *96* (pp. 119-133). <https://doi.org/10.1029/GM096p0119>
1903

1904 Pecha, M.E., Gehrels, G.E., McClelland, W.C., Giesler, D., White, C., & Yokelson, I. (2016).
1905 Detrital zircon U-Pb geochronology and Hf isotope geochemistry of the Yukon-Tanana terrane,
1906 Coast Mountains, southeast Alaska. *Geosphere*, 12(5), 1556–1574.
1907 <https://doi.org/10.1130/GES01301.1>
1908

1909 Peters, K.E., (1986). Guidelines for evaluating petroleum source rock using programmed
1910 pyrolysis. *American Association of Petroleum Geologists Bulletin*, 70, 318–329.
1911 <https://doi.org/10.1306/94885688-1704-11D7-8645000102C1865D>
1912

1913 Peters, K. E. and Casa, M. R. (1994) Applied source rock geochemistry. In L. B. Magoon and W.
1914 G. Dow (Eds.), *The Petroleum System from Source to Trap*, *The American Association of*
1915 *Petroleum Geologists, Memoir 60*, pp. 93–120. <https://doi.org/10.1306/M60585C5>
1916

1917 Plafker, G., & Berg, H.C. (1994). Overview of the geology and tectonic evolution of Alaska. In
1918 G. Plafker & H.C. Berg (Eds.), *The Geology of Alaska* (pp. 989–1021). *Geology of North*
1919 *America, Vol. G-1*. Boulder, Colorado: Geological Society of America.
1920 <https://doi.org/10.1130/DNAG-GNA-G1.989>
1921

1922 Plafker, G., Moore, J. C., & G. R. Winkler (1994), Geology of the southern Alaska margin. In G.
1923 Plafker & H.C. Berg, (Eds.), *The Geology of Alaska* (pp. 389–449). *Geology of North America,*
1924 *Vol. G-1*. Boulder, Colorado: Geological Society of America.
1925

1926 Plafker, G., Nokleberg, W.J., & Lull, J.S. (1989). Bedrock geology and tectonic evolution of the
1927 Wrangellia, Peninsular, and Chugach terranes along the trans-Alaska crustal transect in the
1928 Chugach Mountains and southern Copper River basin, Alaska. *Journal of Geophysical Research:*
1929 *Solid Earth*, 94, 4255–4295. <https://doi.org/10.1029/JB094iB04p04255>
1930

1931 Randive, K.R., K. R. Hari, K.R., M. L. Dora, M.L., Malpe, D.B. & Bhondwe, A.A. (2014).

1932 Study of Fluid Inclusions: Methods, Techniques and Applications. *Gondwana Geological*
1933 *Magazine*, 29(1-2), 19–28.
1934 https://www.researchgate.net/publication/275337661_Study_of_Fluid_Inclusions_Methods_Tec
1935 [hniques_and_Applications](https://www.researchgate.net/publication/275337661_Study_of_Fluid_Inclusions_Methods_Tec)
1936
1937 Reading, H.G. (1980). *Sedimentary environments and facies*. Oxford Blackwell Scientific
1938 Publications.
1939
1940 Reed, B.L., Miesch, A.T., & Lanphere, M.A. (1983). Plutonic rocks of Jurassic age in the
1941 Alaska–Aleutian Range batholith: Chemical variations and polarity. *Geological Society of*
1942 *America Bulletin*, 94, 1232–1240. [https://doi.org/10.1130/0016-](https://doi.org/10.1130/0016-7606(1983)94<1232:PROJAI>2.0.CO;2)
1943 [7606\(1983\)94<1232:PROJAI>2.0.CO;2](https://doi.org/10.1130/0016-7606(1983)94<1232:PROJAI>2.0.CO;2)
1944
1945 Reid, R.P., Carey, S.N., & Ross, D.R. (1996). Late Quaternary sedimentation in the Lesser
1946 Antilles island arc. *Geological Society of America Bulletin*, 108, 78–100.
1947 [https://doi.org/10.1130/0016-7606\(1996\)108<0078:LQSITL>2.3.CO;2](https://doi.org/10.1130/0016-7606(1996)108<0078:LQSITL>2.3.CO;2)
1948
1949 Reiners, P.W., & Ehlers, T. (2005). Low-Temperature Thermochronology: Techniques,
1950 Interpretations, and Application. *Reviews in mineralogy and geochemistry* 58. Mineralogical
1951 Society of America. <https://doi.org/10.1515/9781501509575>
1952
1953 Richter, D.L. (1976). Geologic map of the Nabesna Quadrangle, Alaska. *United States*
1954 *Geological Survey, Miscellaneous Investigations Series Map I-932*. 1:250,000 scale.

1955

1956 Ridgway, K.D., Sweet, A.R., & Cameron, A.R. (1995). Climatically induced floristic changes
1957 across the Eocene-Oligocene transition in the northern high latitudes, Yukon Territory, Canada.
1958 *Geological Society of America Bulletin*, 107(6), 676–696.

1959 [https://doi.org/10.1130/0016-7606\(1995\)107%3C0676:CIFCAT%3E2.3.CO;2](https://doi.org/10.1130/0016-7606(1995)107%3C0676:CIFCAT%3E2.3.CO;2)

1960

1961 Ridgway, K.D., Trop, J.M., Nokleberg, W.J., Davidson, C.M., & Eastham, K.R. (2002).
1962 Mesozoic and Cenozoic tectonics of the eastern and central Alaska range: Progressive basin
1963 development and deformation in a suture zone. *Geological Society of America Bulletin*, 114(12),
1964 1480–1504. [https://doi.org/10.1130/0016-7606\(2002\)114%3C1480:MACTOT%3E2.0.CO;2](https://doi.org/10.1130/0016-7606(2002)114%3C1480:MACTOT%3E2.0.CO;2)

1965

1966 Ridgwell, A. (2004). A Mid Cenozoic revolution in the regulation of ocean chemistry. *Marine*
1967 *Geology*, 217, 339–357. <https://doi.org/10.1016/j.margeo.2004.10.036>

1968

1969 Rioux, M., Hacker, B., Mattinson, J., Kelemen, P., Hanghoj, K., & Plank, T. (2003). The role of
1970 intermediate to felsic plutonism in the accreted Talkeetna arc, south-central Alaska. *Geological*
1971 *Society of America, Abstracts with Programs*, 35, 430.

1972

1973 Rioux, M., Hacker, B., Mattinson, J., Kelemen, P., Blusztajn, J., & Gehrels, G. (2007). Magmatic
1974 development of an intra-oceanic arc: high-precision U–Pb zircon and whole-rock isotopic
1975 analyses from the accreted Talkeetna arc, south-central Alaska. *Geological Society of America*
1976 *Bulletin*, 119, 1168–1184. <https://doi.org/10.1130/B25964.1>

1977

1978 Roeske, S.M., Pavlis, T.L., Snee, L.W., & Sisson, V.B. (1991). $^{40}\text{Ar}/^{39}\text{Ar}$ isotopic ages from the
1979 combined Wrangellia-Alexander terrane along the Border Ranges fault system in the eastern
1980 Gugach Mountains and Glacier Bay, Alaska. In *Geologic Studies in Alaska by the United States*
1981 *Geological Survey 1990* (pp. 180–195).

1982

1983 Roeske, S.M., Snee, L.W., & Pavlis, T.L. (2003). Dextral-slip reactivation of an arc-forearc
1984 boundary during Late Cretaceous–Early Eocene oblique convergence in the northern Cordillera.
1985 In V.D. Sisson, M. Roeske & T.L. Pavlis (Eds.), *Geology of a transpressional orogen developed*
1986 *during ridge–trench interaction along the North Pacific margin* (pp. 141–170). *Geological*
1987 *Society of America Special Papers, Vol. 371*. Boulder, Colorado: Geological Society of America.
1988 <https://doi.org/10.1130/0-8137-2371-X.141>

1989

1990 Rubin, C.M., & Saleeby, J.B. (1991). The Gravina Sequence: remnants of a Mid-Mesozoic
1991 Oceanic Arc in Southern Southeast Alaska. *Journal of Geophysical Research*, 96, 14,551–
1992 14,568. <https://doi.org/10.1029/91JB00591>

1993

1994 Rubin, C.M., & Saleeby, J.B. (1992) Tectonic history of the eastern edge of the Alexander
1995 terrane, Southeast Alaska. *Tectonics*, 11(3), 586–602. <https://doi.org/10.1029/91TC02182>

1996

1997 Rubin, C.M., Saleeby, J.B., Cowan, D.S., Brandon, M.T., & McGroder, M.F. (1990). Regionally
1998 extensive mid-Cretaceous west-vergent thrust system in the northwestern Cordillera:
1999 implications for continent-margin tectonism. *Geology*, 18, 276–280.
2000 [https://doi.org/10.1130/0091-7613\(1990\)018%3C0276:REMCWV%3E2.3.CO;2](https://doi.org/10.1130/0091-7613(1990)018%3C0276:REMCWV%3E2.3.CO;2)

2001

2002 Saleeby, (1983). Accretionary tectonics of the North American Cordillera. *Annual Review of*

2003 *Earth and Planetary Sciences*, 15, 45–73. <https://doi.org/10.1146/annurev.ea.11.050183.000401>

2004

2005 Schmidt, D., Schmidt, S.Th., Mullis, J., Mählmann, R.F. & Frey, M. (1997). Very low-grade

2006 metamorphism of the Taveyanne formation of western Switzerland. *Contributions to Mineralogy*

2007 *and Petrology*, 129, 385–403. <https://doi.org/10.1007/s004100050344>

2008

2009 Sclater, J.G., & Christie, P.A.F. (1980). Continental stretching: an explanation of the post-mid-

2010 Cretaceous subsidence of the central North Sea basin. *Journal of Geophysical Research*, 85,

2011 3711-3739. <https://doi.org/10.1029/JB085iB07p03711>

2012

2013 Seilacher, A. (2007). *Trace fossil analysis*. Springer: New York, New York.

2014

2015 Shepard, G.E., Müller, R.D., & Seton, M. (2013). The tectonic evolution of the Arctic since

2016 Pangea breakup: Integrating constraints from surface geology and geophysics with mantle

2017 structure. *Earth-Science Reviews*, 124, 148–183. <https://doi.org/10.1016/j.earscirev.2013.05.012>

2018

2019 Short, E.J., Snyder, D.C., Trop, J.M., Hart, W.K., & Layer, P.W. (2005). New findings on Early

2020 Cretaceous volcanism within the allochthonous Wrangellia terrane, south-central Alaska:

2021 Stratigraphic, geochronologic, and geochemical data from the Chisana Formation, Nutzotin

2022 Mountains. *Geological Society of America, Abstracts with Programs*, 37, 81.

2023

2024 Siever, R. (1979). Plate-tectonic controls on diagenesis. *The Journal of Geology*, 87, 127–155.
2025 <https://www.jstor.org/stable/30060249>
2026

2027 Sigloch, K., & Mihalynuk, M.G. (2017). Mantle and geological evidence for a Late Jurassic-
2028 Cretaceous suture spanning North America. *Geological Society of America Bulletin*, 129(11/12),
2029 1489–1520. <https://doi.org/10.1130/B31529.1>
2030

2031 Sinclair, H.D., & Naylor, M. (2012). Foreland basin subsidence driven by topographic growth
2032 versus plate subduction. *Geological Society of America Bulletin*, 124(3/4), 368–379.
2033 <https://doi.org/10.1130/B30383.1>
2034

2035 Stamatakos, J.A., Trop, J.M., & Ridgway, K.D. (2001). Late Cretaceous paleogeography of
2036 Wrangellia: Paleomagnetism of the MacColl Ridge Formation, southern Alaska, revisited.
2037 *Geology*, 29, 947–950. [https://doi.org/10.1130/0091-7613\(2001\)029<0947:LCPOWP>2.0.CO;2](https://doi.org/10.1130/0091-7613(2001)029<0947:LCPOWP>2.0.CO;2)
2038

2039 Stanley, B. (2012). *Structural geology and geochronology of the Kluane Schist, southwest Yukon*
2040 *Territory* (Master's thesis). Waterloo, Ontario: University of Waterloo.
2041 <http://hdl.handle.net/10012/7096>
2042

2043 Staplin, F. L. (1969). Sedimentary organic matter, organic metamorphism, and oil and gas
2044 occurrence. *Bulletin of Canadian Petroleum Geologists*, 17, 47–66.
2045 <https://doi.org/10.35767/gscpgbull.17.1.047>
2046

2047 Stone, P., & Merriman, R.J. (2004). Basin history favours an accretionary origin for the Southern
2048 Uplands terrane, Scottish Caledonides. *Journal of the Geological Society*, London, 161, 829–
2049 836. <https://doi.org/10.1144/0016-764903-170>
2050

2051 Stowell, R. R., & Crawford, M. L., (2000). Metamorphic history of the Coast Mountains orogen,
2052 western British Columbia and southeastern Alaska. In H.H. Stowell & W.C. McClelland (Eds.),
2053 *Tectonics of the Coast Mountains, Southeastern Alaska and British Columbia* (pp. 257–283).
2054 *Geological Society of America Special Paper 343*. Boulder, Colorado: Geological Society of
2055 America. <https://doi.org/10.1130/0-8137-2343-4.257>
2056

2057 Stowell, H.H., & R.J. Hooper (1990). Structural development of the western metamorphic belt
2058 adjacent to the Coast Plutonic Complex: Evidence from Holkham Bay. *Tectonics*, 9, 391–407.
2059 <https://doi.org/10.1029/TC009i003p00391>
2060

2061 Stowell, H.H., Green, N.L. & Hooper, R.J., (2000). Geochemistry and tectonic setting of basaltic
2062 volcanism, northern Coast Mountains. In H.H. Stowell & W.C. McClelland (Eds.), *Tectonics of*
2063 *the Coast Mountains, Southeastern Alaska and British Columbia* (pp. 235–255). *Geological*
2064 *Society of America Special Paper 343*. Boulder, Colorado: Geological Society of America.
2065 <https://doi.org/10.1130/0-8137-2343-4.235>
2066

2067 Sturrock, D.L. (1975). *The Pyroxenite Creek ultramafic complex: an Alaska-type ultramafic*
2068 *intrusion in southwest Yukon* (Master's thesis). Vancouver, British Columbia: University of
2069 British Columbia.

2070

2071 Sturrock, D.L., Armstrong, R.L., & Maxwell, R.B. (1980). Age and Sr isotope composition of
2072 the Pyroxenite Creek ultramafic complex, southwestern Yukon Territory: An Alaskan-type
2073 ultramafic intrusion. In *Current Research, Part B* (pp. 185–188), *Geological Survey of Canada*
2074 *Paper 80-1B*.

2075

2076 Sweeney, J.J., & Burnham, A.K. (1990). Evaluation of a simple model of vitrinite reflectance
2077 based on chemical kinetics. *The American Association of Petroleum Geologists Bulletin*, 74,
2078 1559–1570. <https://doi.org/10.1306/0C9B251F-1710-11D7-8645000102C1865D>

2079

2080 Tempelman-Kluit, D.J. (1976). The Yukon Crystalline terrane: Enigma in the Canadian
2081 Cordillera. *Geological Society of America Bulletin* 87, 1343–1357. [https://doi.org/10.1130/0016-](https://doi.org/10.1130/0016-7606(1976)87<1343:TYCTEI>2.0.CO;2)
2082 [7606\(1976\)87<1343:TYCTEI>2.0.CO;2](https://doi.org/10.1130/0016-7606(1976)87<1343:TYCTEI>2.0.CO;2)

2083

2084 Tennant, J.P., Mannion, P.D., Upchurch, P., Sutton M.D., & Price, G.D. (2017). Biotic and
2085 environmental dynamics through the Late Jurassic-Early Cretaceous transition: Evidence for
2086 protracted faunal and ecological turnover. *Biological Reviews*, 92, 776–814.

2087 <https://doi.org/10.31233/osf.io/gnsb7>

2088

2089 Thompson, A.B. (1970). Laumontite equilibria and the zeolite facies. *American Journal of*
2090 *Science*, 269, 267–275. <https://doi.org/10.2475/ajs.269.3.267>

2091

2092 Tissot, B.P., & Welte, D.H (1984). *Petroleum Formation and Occurrence* (2nd Ed.). Springer-
2093 Verlag: Berlin, Germany.

2094

2095 Traverse, A. (1988). *Paleopalynology*. Unwin Hyman: New York, New York.

2096

2097 Trop, J.M, Benowitz, J.A., Koepp, D.O., Sunderlin, D., Brueske, M.E., Layer, P.W., &
2098 Fitzgerald, P.G. (2020). Stitch the ditch: Nutzotin Mountains (Alaska) fluvial strata and a dike
2099 record ca. 117-114 Ma accretion of Wrangellia with western North America and initiation of the
2100 Totschunda fault. *Geosphere*, 16(1), 82–110. <https://doi.org/10.1130/GES02127.1>

2101

2102 Trop, J.M., & Ridgway, K.D. (2007). Mesozoic and Cenozoic tectonic growth of southern
2103 Alaska: a sedimentary basin perspective. In K.D. Ridgway, J.M. Trop & J.M. O’Neils (Eds.),
2104 *Tectonic growth of a collisional continental margin; crustal evolution of southern Alaska* (pp.
2105 55–94). *Geological Society of America Special Paper 421*. The Geological Society of America.
2106 [https://doi.org/10.1130/2007.2431\(04\)](https://doi.org/10.1130/2007.2431(04))

2107

2108 Trop, J.M., Ridgway, K.D., Manuszak, J.D., & Layer, P. (2002). Mesozoic sedimentary-basin
2109 development on the allochthonous Wrangellia composite terrane, Wrangell Mountains basin,
2110 Alaska: A long-term record of terrane migration and arc construction. *Geological Society of*
2111 *America Bulletin*, 114, 693–717. [https://doi.org/10.1130/0016-7606\(2002\)1142.0.CO;2](https://doi.org/10.1130/0016-7606(2002)1142.0.CO;2)

2112

2113 Uchman, A. and Wetzel, A. (2012). Deep-sea fans (Chapter 21, 643–671). In R.G. Bromley & D.
2114 Knaust (Eds.), *Trace Fossils as Indicators of Sedimentary Environments*. Developments in
2115 Sedimentology 64. Elsevier: Amsterdam. <https://doi.org/10.1016/B978-0-444-53813-0.00021-6>
2116

2117 van Andel, T.H. (1975). Mesozoic/Cenozoic compensation depth and the global distribution of
2118 calcareous sediments. *Earth and Planetary Science Letters*, 26, 187–194.
2119 [https://doi.org/10.1016/0012-821X\(75\)90086-2](https://doi.org/10.1016/0012-821X(75)90086-2)
2120

2121 van der Heyden, P. (1992). A Middle Jurassic to Early Tertiary Andean-Sierran arc model for the
2122 Coast Belt of British Columbia. *Tectonics*, 11, 82–97. <https://doi.org/10.1029/91TC02183>
2123

2124 van Hite, J.E. (1978). Geohistory analysis- application of micropaleontology in exploration
2125 geology. *American Association of Petroleum Geologists Bulletin*, 62, 201–222.
2126 <https://doi.org/10.1306/C1EA4815-16C9-11D7-8645000102C1865D>
2127

2128 Vice, L. (2017). *Late Cretaceous to Paleocene evolution of the Blanchard River assemblage,*
2129 *southwest Yukon: implications for Mesozoic accretionary processes in the northwestern*
2130 *Cordillera* (Master’s thesis). Burnaby, British Columbia: Simon Fraser University
2131

2132 Vieira, F., & Hamza, V. (2018). Global heat flow: New estimates using digital maps and GIS
2133 techniques. *International Journal of Terrestrial Heat Flow and Applied Geothermics*, 1(1), 6–13.
2134 <https://doi.org/10.31214/ijthfa.v1i1.6>
2135

2136 Weaver, C.E. (1989). *Clays, Muds and Shales*. Developments in Sedimentology 44, Elsevier:
2137 Amsterdam.

2138

2139 Weber, J.C., Ferrill, D.A., & Roden-Tice, M.K. (2001). Calcite and quartz microstructural
2140 geothermometry of low-grade metasedimentary rocks, Northern Range, Trinidad. *Journal of*
2141 *Structural Geology*, 23(1), 93–112. [https://doi.org/10.1016/S0191-8141\(00\)00066-3](https://doi.org/10.1016/S0191-8141(00)00066-3)

2142

2143 Wheeler, J.O., & McFeely, P. (1991). Tectonic assemblage map of the Canadian Cordillera and
2144 adjacent parts of the United States of America. *Geological Survey of Canada, Map 1712A*. Scale
2145 1:2,000,000. <https://doi.org/10.4095/133549>

2146

2147 Wikipedia, 2020. “*Brittle-ductile transition zone*”. Accessed August 29, 2020.
2148 https://en.wikipedia.org/wiki/Brittle%E2%80%93ductile_transition_zone

2149

2150 Wolf, K.H., & Chilingarian, G.V. (1976). Diagenesis of sandstones and compaction. In G.V.
2151 Chilingarian & K.H. Wolf (Eds.), *Developments in sedimentology, Volume 18B* (pp. 69–444).
2152 *Compaction of coarse-grained sediments II*. Elsevier Scientific Publishing Company: New York,
2153 New York. [https://doi.org/10.1016/S0070-4571\(08\)71100-2](https://doi.org/10.1016/S0070-4571(08)71100-2)

2154

2155 Woodcock, N.H. (2004). Life span and fate of basins. *Geology*, 32(8), 685–688.
2156 <https://doi.org/10.1130/G20598.1>

2157

2158 Xie, X., & Heller, P.L. (2009). Plate tectonics and basin subsidence history. *Geological Society*
2159 *of America Bulletin*, 121(1/2), 55–64. <https://doi.org/10.1130/B30383.1>
2160

2161 Yokelson, I., Gehrels, G.E., Pecha, M., Giesler, D., White, C., & McClelland, W.C. (2015). U–
2162 Pb and Hf isotope analysis of detrital zircons from Mesozoic strata of the Gravina belt, southeast
2163 Alaska. *Tectonics*, 34, 2052–2066. <https://doi.org/10.1002/2015TC003955>
2164

2165 Zhang, W. Johnston, S.T. & Currie, C.A. (2019). Kimberlite magmatism induced by west-
2166 dipping subduction of the North American plate. *Geology*, 47, 395–398.
2167 <https://doi.org/10.1130/G45813.1>
2168

2169 Ziegler, P.A., Bertotti, G., & Cloetingh, S. (2002). Dynamic processes controlling foreland
2170 development — the role of mechanical (de)coupling of orogenic wedges and forelands.
2171 *European Geoscience Union Stephan Mueller Special Publication Series, 1* (pp. 17–56).
2172 <https://doi.org/10.5194/smsps-1-17-2002>
2173
2174
2175
2176

Table 1. Published low-temperature thermochronometric data, Dezadeash Formation, Yukon, Canada.

Sample	Lithology	Elevation (m)	AHe (Ma)	ZHe (Ma)	AFT (Ma)	ZFT (Ma)
KLB04	metapelite	605	17.8 ± 1.6	59.7 ± 8.1	n.a.	n.a.
KLB91	mudstone	725	11.4 ± 0.8	68.8 ± 2.3	n.a.	109.9 ± 8.9
61115-2A	metagreywacke	941	n.a.	14.0 ± 0.4	n.a.	136.5 ± 8.5
T_c (°C)			70	180	120	240
PRZ (°C)			40-70	130-180	n.a.	n.a.
PAZ (°C)			n.a.	n.a.	60-120	180-240

•AHe= apatite (U-Th)/He, ZHe= zircon (U-Th)/He, AFT= apatite fission-track, and ZFT= zircon fission-track thermochronometer age.

•T_c= closure temperature (radioactive decay product retained below this temperature, but not above it; also the temperature of a mineral at the time given by its radiometric age).

•PRZ= partial retention zone (temperature window over which radioactive decay product is retained).

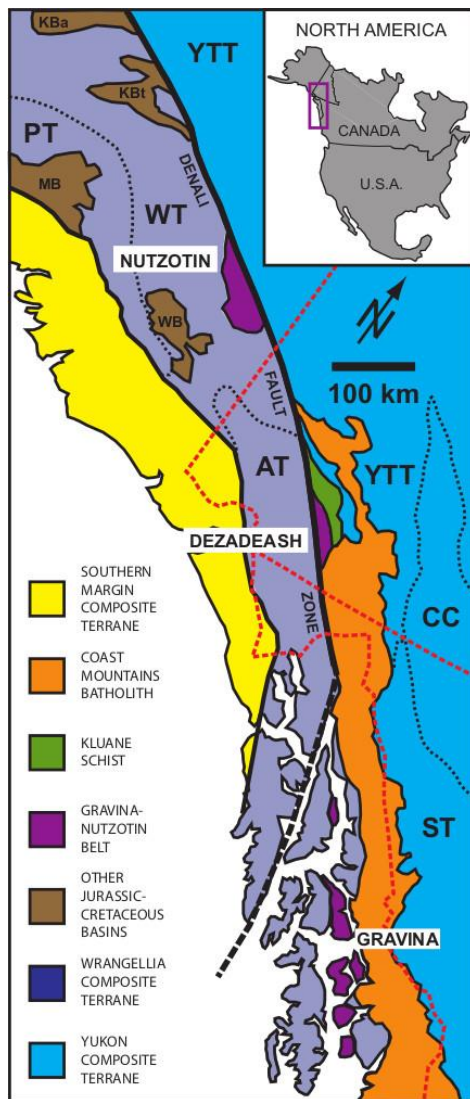
•PAZ= partial annealing zone (temperature window over which radioactive decay product is preserved). Temperatures from Brandon and Vance (1998) and Peyton and Carrapa (2013). Note that the temperatures are only approximate because they depend on the cooling rate, chemistry of the mineral, and grain-size of the mineral (Brandon and Vance, 1998).

•Samples KLB4 and KLB91 from Enkelmann et al. (2017). Sample 61115-2A from McDermott et al. (2019), although it is uncertain if this came from the Dezadeash Formation.

2177

2178

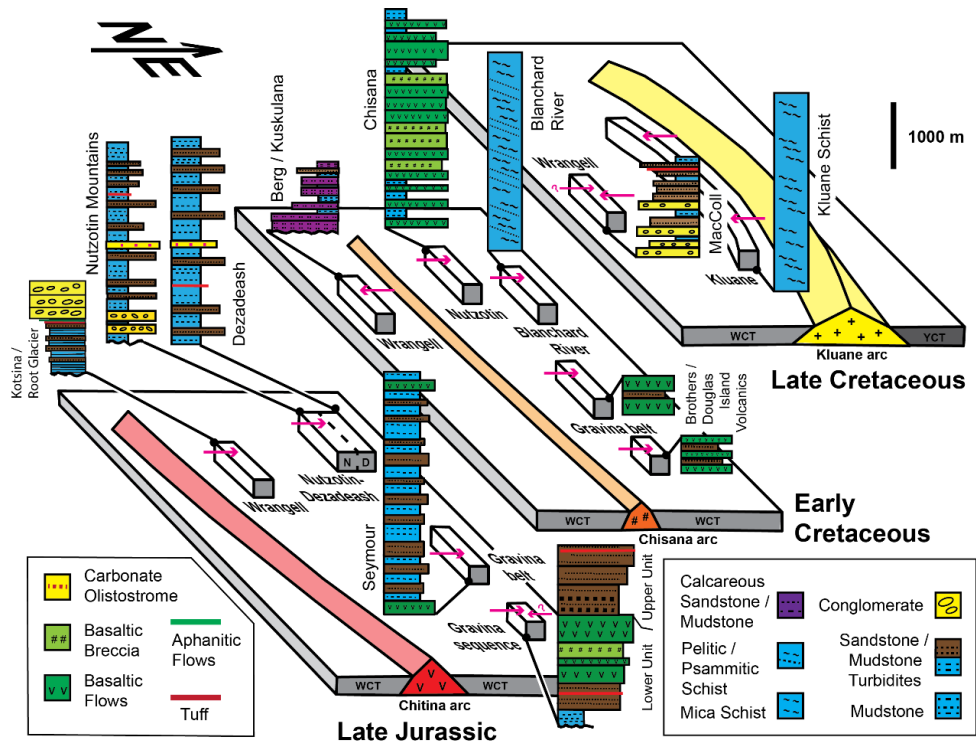
2179



2180

2181

2182 Fig. 1. Location map and geologic setting of the Dezadeash Formation, Yukon (compiled from
 2183 MacKevett 1978; Wheeler and McFeely 1991; and Monger 2014). AT, Alexander terrane; CC,
 2184 Cache Creek terrane; PT, Peninsular terrane; ST, Stikine terrane; Y, Yakutat terrane; YTT,
 2185 Yukon-Tanana terrane; WT, Wrangellia terrane. Kootenay, Cassiar, and Quesnel terranes not
 2186 shown. Other Jurassic-Cretaceous basins not part of the Gravina-Nutzotin belt: KBa, Kahiltna
 2187 basin-Alaska Range; KBt, Kahiltna basin-Talkeetna Mountains; MB, Matanuska Valley basin;
 2188 WB, Wrangell Mountains basin; T, Talkeetna arc; C, Chitina arc; A, Chisana arc; K, Kluane arc.



2189

2190

2191 Fig. 2. Conceptual diagram depicting the spatial-temporal relationships of magmatic arcs (i.e.,

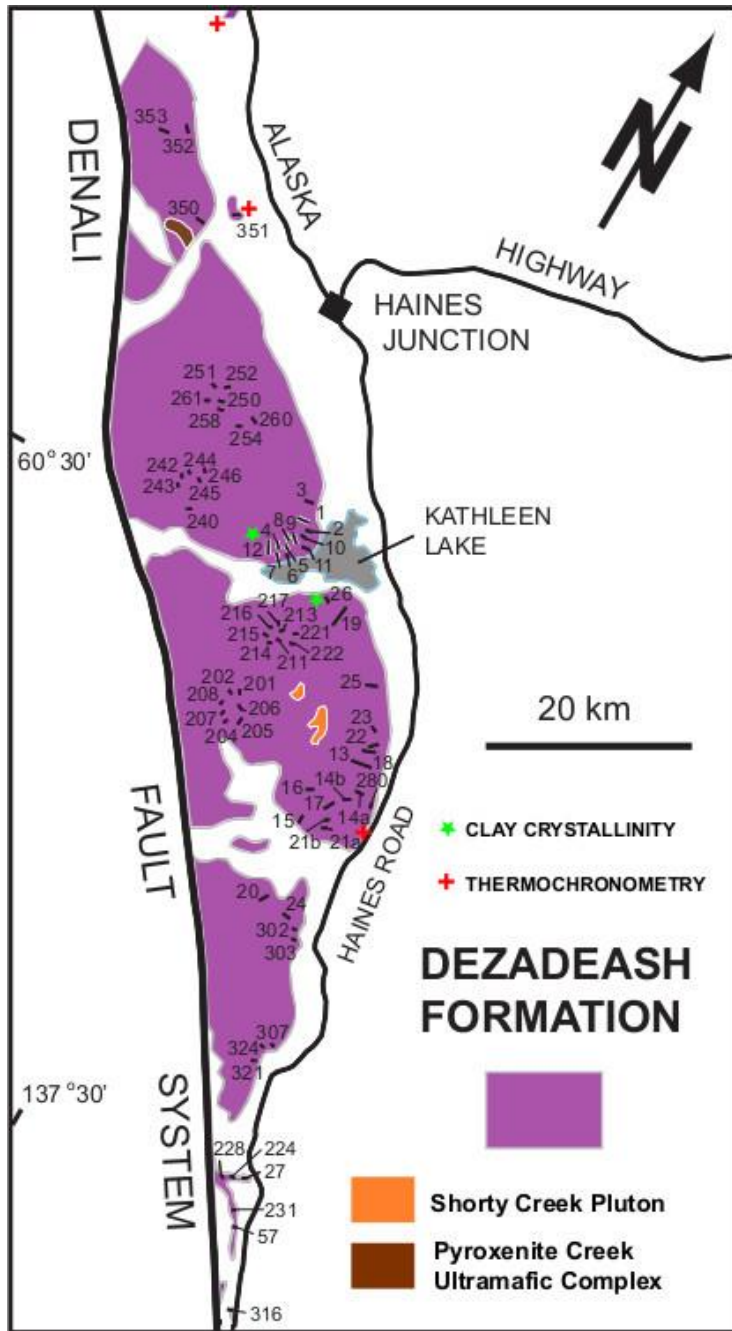
2192 Chitina, Chisana, and Kluane) and associated basins (i.e., Wrangell, Nutzotin-Dezadeash,

2193 Gravina belt, Gravina sequence, Blanchard River assemblage, and Kluane Schist). Only

2194 movement on the Denali fault (dashed line separating Nutzotin-Dezadeash basin) has been

2195 restored. Small (pink) arrows indicate general paleoflow directions.

2196



2197

2198

2199 Fig. 3. Location of measured sections (numbers) in the Dezadeash Formation, Yukon, from
 2200 which samples were collected. Also shown is location of published thermochronometric data for
 2201 the Dezadeash Formation (see text for details).

2202



2203

2204

2205 Fig. 4. Photographs of representative secondary structures in the Dezadeash Formation, Yukon.

2206 (A) Parting (sub-vertical) in thin- to medium-bedded sandstone-mudstone couplets, 1.5m long

2207 Jacob's Staff for scale. (B) Parting (sub-vertical) in thin-bedded sandstone-mudstone couplets,

2208 green squares at top of scale card are 1cm long. (C) Spaced cleavage (vertical) in mudstone,

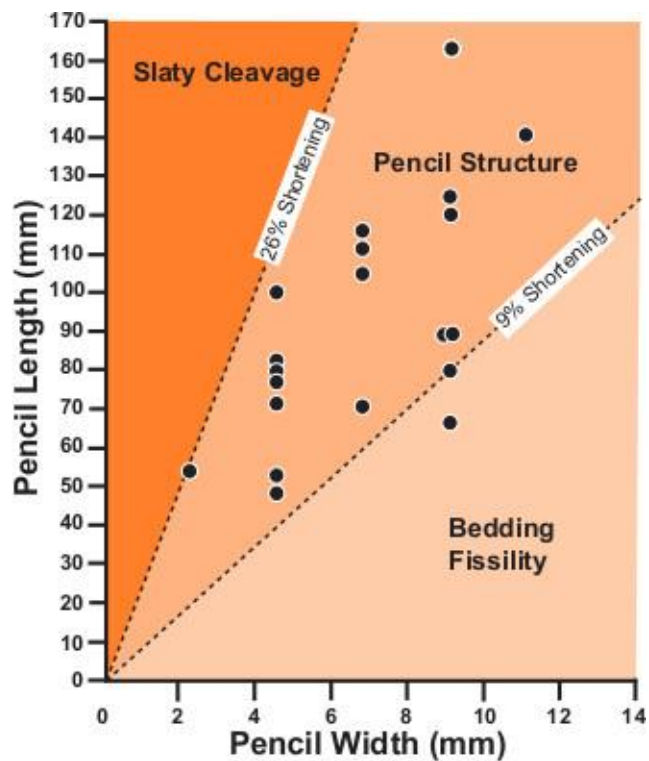
2209 1.5m long Jacob's Staff for scale. (D) Pencil structure in mudstone, length of black bar in circle

2210 on notebook is 6 cm. (E) Parting (vertical) in hemipelagite bed (brown bed), dark brown interval

2211 on Jacob's Staff is 0.1m long. (F) Parting (horizontal) in tuff bed, 1.5m long Jacob's Staff for

2212 scale.

2213



2214

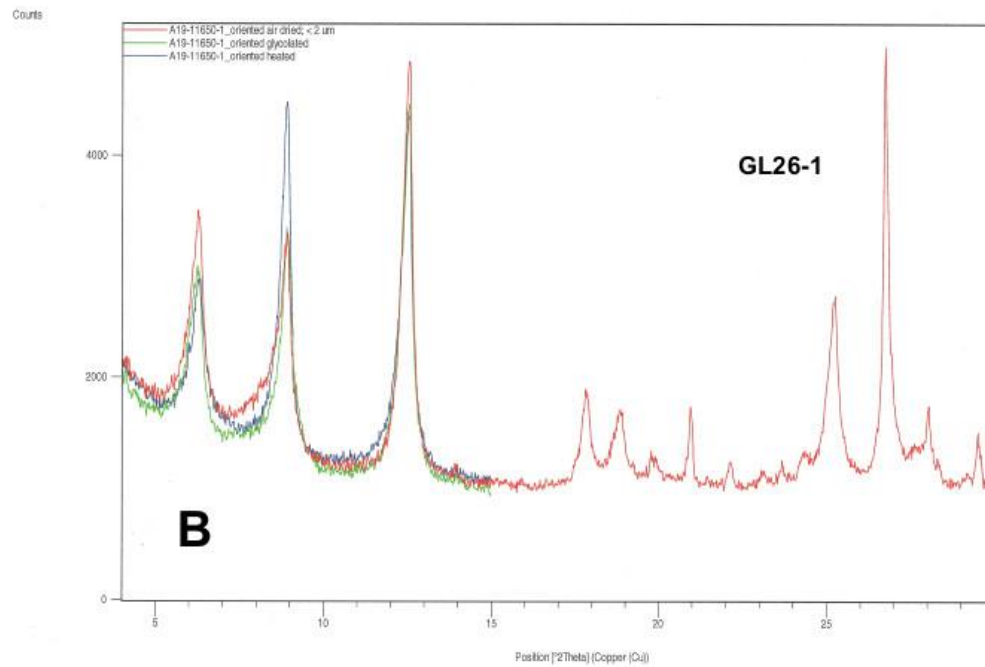
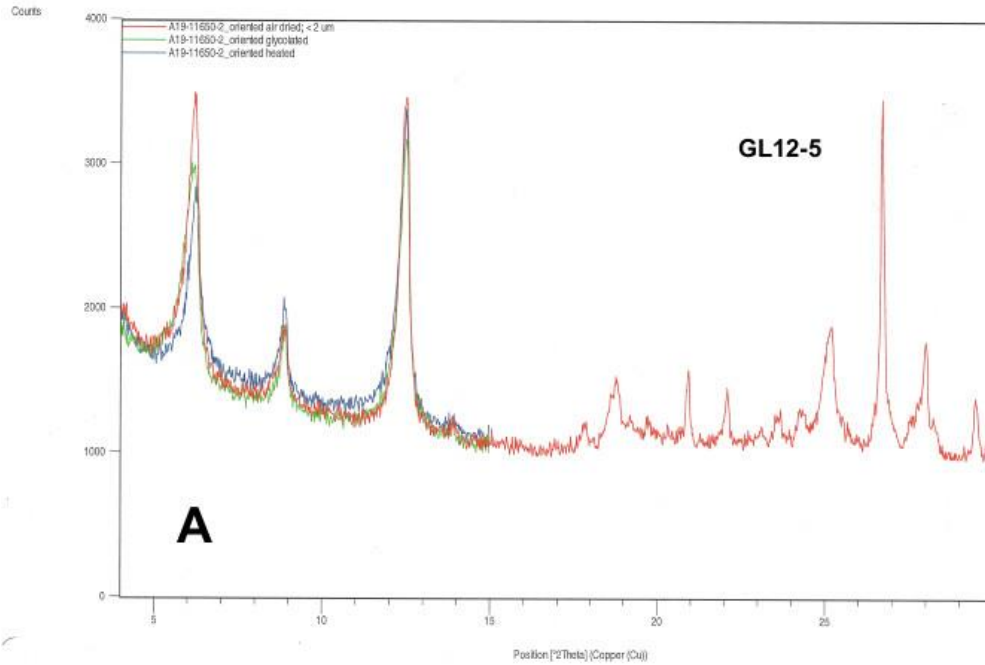
2215

2216 Fig. 5. Plot of pencil width vs. length of mudstone samples from the Dezadeash Formation,

2217 Yukon (diagram after Passchier and Trouw, 1996).

2218

2219



2220

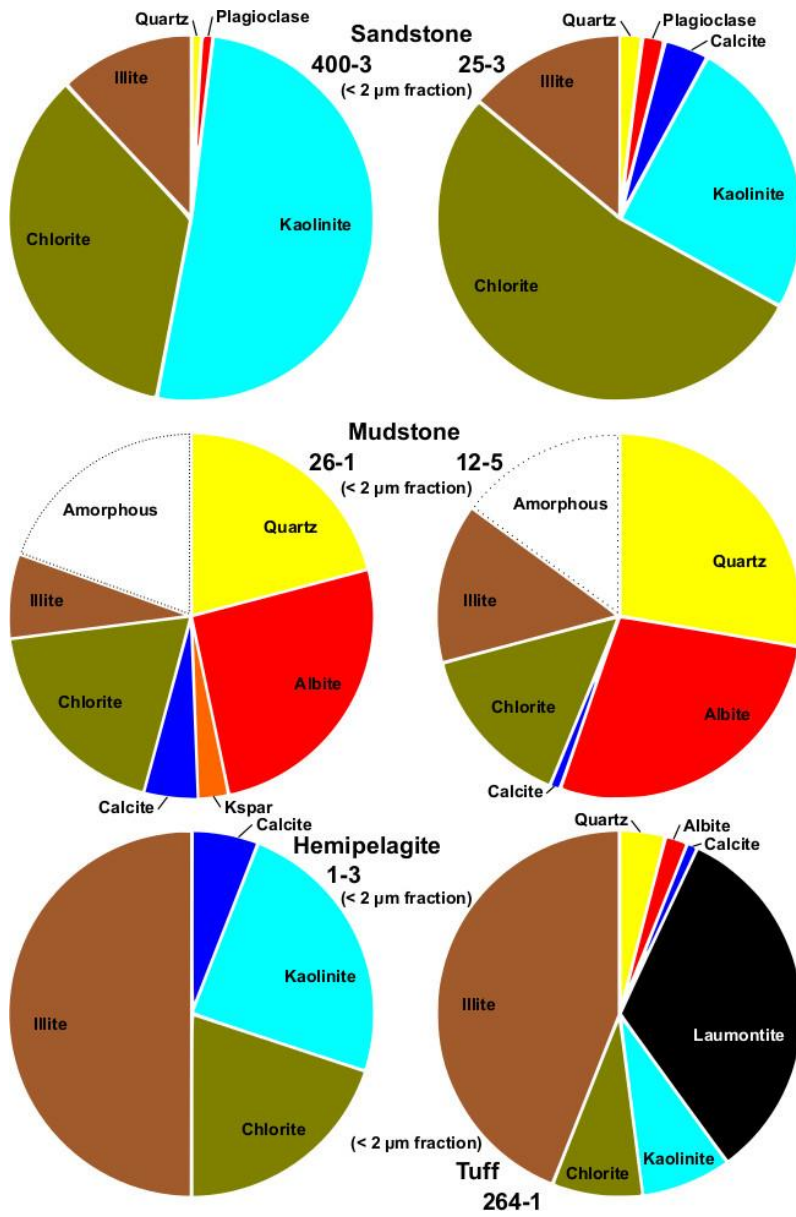
2221

2222 Fig. 6. X-ray diffractograms of mudstone samples from the Dezadeash Formation, Yukon. (A)

2223 GL12-5. (B) GL26-1.

2224

2225



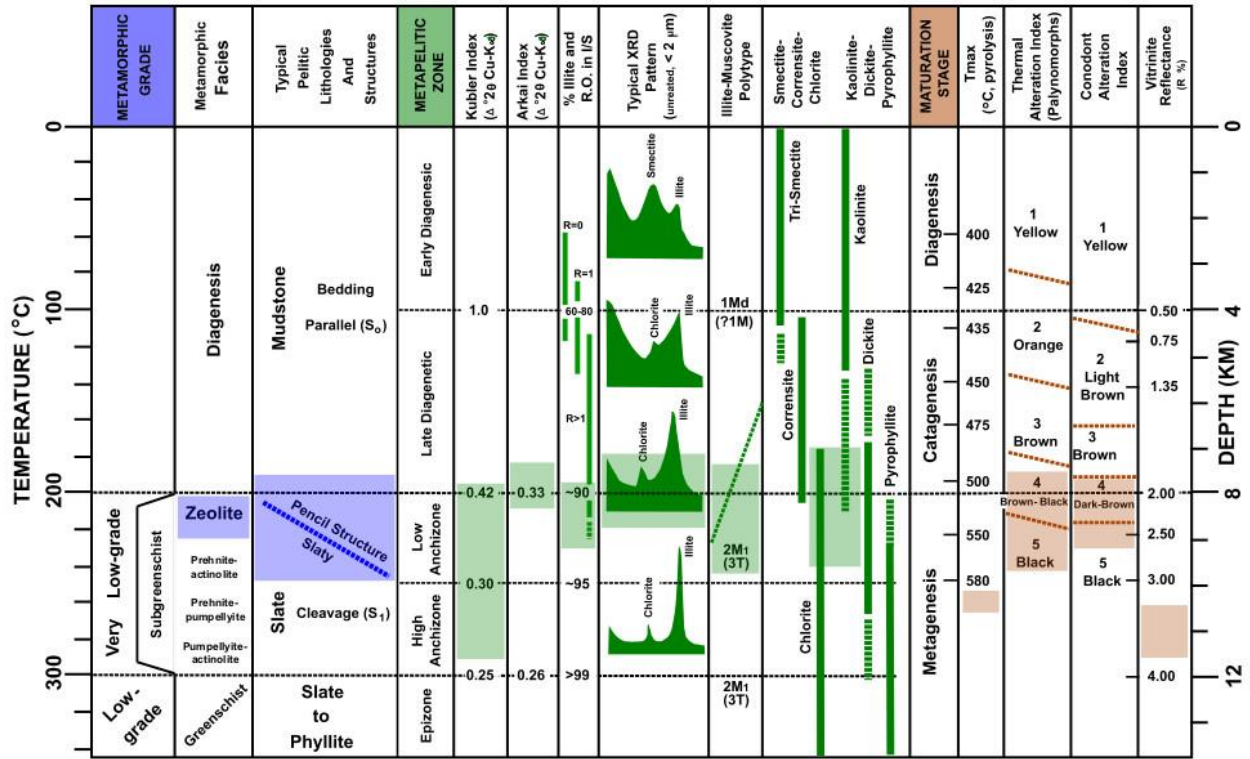
2226

2227

2228 Fig. 7. Pie diagrams of clay-size fraction (< 2 μm) in sandstone, mudstone, hemipelagite, and

2229 tuff samples from the Dezadeash Formation, Yukon.

2230



2231

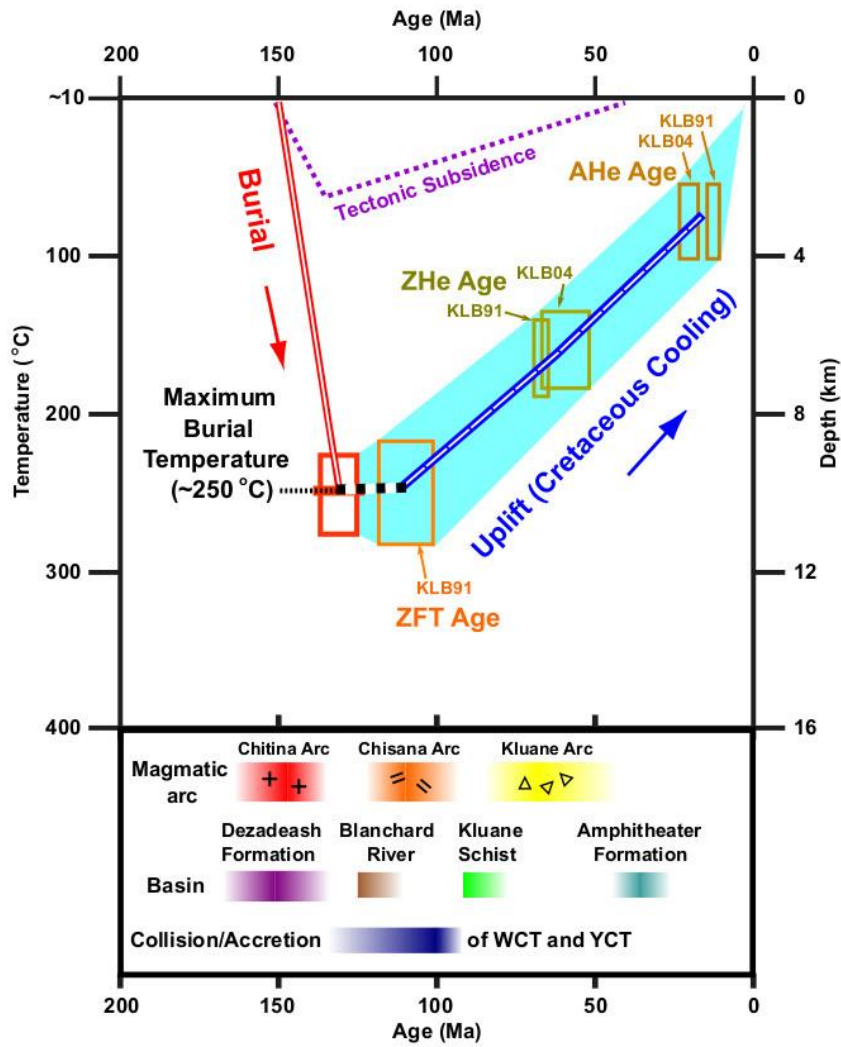
2232

2233 Fig. 8. Correlation diagram of metamorphic grade, metapelitic zone, and maturation stage for the

2234 Dezadeash Formation, Yukon. Note that temperature and depth are only approximate. Compiled

2235 from Héroux et al. (1979), Bird et al. (1999), and Hartkopf-Fröder et al. (2015).

2236



2237

2238

2239 Fig. 9. Time vs. temperature diagram for the Dezhadeash Formation, Yukon. Thermochronometric

2240 samples KBL04 and KBL91 from Enkelmann et al. (2017). Size of the boxes for

2241 thermochronometric samples indicate uncertainties in age and temperature estimates.

2242

2243

Table S1. Section locations (along which samples were collected), Dezadeash Formation, Yukon, Canada.

Section	NTS Map		Easting	Northing		Easting	Northing
1	115 A/11	Start	371000	6719500	End	369200	6718000
2	115 A/11	Start	371600	6718700	End	371200	6718600
3	115 A/11	Start	370400	6720800	End	369200	6720500
4	115 A/11	Start	369700	6716600	End	369200	6716200
5	115 A/11	Start	369700	6716500	End	369400	6716700
6	115 A/11	Start	370500	6716300	End	370300	6716600
7	115 A/11	Start	369500	6715600	End	369300	6716000
8	115 A/11	Start	370300	6717000	End	369400	6717500
9	115 A/11	Start	370600	6717800	End	369800	6718300
10	115 A/11	Start	370900	6718300	End	370400	6718200
12	115 A/11	Start	369300	6715700	End	368500	6716700
13	115 A/11	Start	385400	6702500	End	383600	6702300
14A	115 A/11	Start	385500	6699300	End	384800	6699200
14B	115 A/11	Start	384700	6698800	End	384300	6698700
16	115 A/11	Start	381200	6698200	End	380700	6698200
17	115 A/11	Start	383300	6696900	End	384200	6697700
18	115 A/11	Start	385100	6703900	End	384100	6703800
19	115 A/11	Start	377000	6715000	End	376200	6714300
20	115 A/11	Start	382500	6687700	End	382300	6687300
21B	115 A/11	Start	384300	6695700	End	384300	6695700
22	115 A/11	Start	384700	7604600	End	384500	6705000
23	115 A/11	Start	384300	6705400	End	383800	6705900
24	115 A/11	Start	384700	6684700	End	384500	6684800
25	115 A/11	Start	382200	6709300	End	381400	6708700
26							
27	115 A/2	Start	392000	6665100	End	392000	6665100
201	115 A/6	Start	371800	6701400	End	371800	6701400
208	115 A/6	Start	371200	6701400	End	371200	6701400
219	115 A/6	Start	373000	6708700	End	373000	6708700
244	115 A/12	Start	358200	6717500	End	358200	6717500
247	115 A/12	Start	359400	6717700	End	359400	6717700
250	115 A/12	Start	358500	6725000	End	358500	6725000
257	115 A/12	Start	358600	6724700	End	358600	6724700
260	115 A/12	Start	361600	6724500	End	360700	6725300
280 (74B, 400)	116 A/6	Start	387094	6608552	End	387094	6608552
351 (74A)	115 A/12	Start	352956	6740958	End	352956	6740958
352	115 A/13	Start	344400	6745700	End	344300	6745800

2244

2245

Supplementary Table S2. X-ray diffraction analyses, Dezadeash Formation, Yukon, Canada.

Sample	Lithology	Grain-size	Weight (%)	Quartz (%)	Plagioclase (%)	Kspar (%)	Calcite (%)	Muscovite (%)	Laumontite (%)	Siderite (%)	Kaolinite (%)	Chlorite (%)	Illite (%)	Other (%)	Clay Minerals	Total (%)	
25-3	Sandstone	Bulk (Coarse+Clay)	100.00	22	25	0	12	4	0	0	15	20	2			37	100
		Coarse (>2µm)	90.88	24	28	0	12	5	0	0	14	17	0			31	100
		Clay (<2µm)	9.12	2	2	0	4	0	0	0	25	53	14			92	100
400-3	Sandstone	Bulk	100.00	24	37	0	2	2	0	0	11	15	9			34	100
		Coarse	94.96	25	40	0	2	2	0	0	8	55	8			31	100
		Clay	5.04	1	1	0	0	0	0	0	51	35	12			98	100
1-3	Hemipelagite	Bulk	100.00	12	5 (Albite)	<0.1	63	2	0	0	8	8	2	Pyrite	18	100	
		Coarse	96.00	13	5	<0.1	66	2	0	0	7	7	0	Bassanite	15	100	
		Clay	4.00	0	0	0	6	0	0	0	24	20	50		94	100	
264-1	Tuff	Bulk	100.00	37	7 (Albite)	0	6	3	41	3	0.5	0.5	2			2	100
		Coarse	94.93	37	7	0	7	4	42	3	0	0	0			0	100
		Clay	5.07	4	2	0	1	0	33	0	8	8	44			60	100
12-5	Mudstone	Bulk	-	-	-	-	-	-	-	-	-	-	-	<10% expandable clay	-	-	
		Coarse	-	-	-	-	-	-	-	-	-	-	-	-	KI=0.42, AI=0.34	-	-
		Clay	100	29.8	21.9 (Albite)	<0.1	1.0	-	-	-	0	15.9	15.3	Amorphous (16.1%)	31.2	100	
26-1	Mudstone	Bulk	-	-	-	-	-	-	-	-	-	-	-	KI=0.26, AI=0.33	-	-	
		Coarse	-	-	-	-	-	-	-	-	-	-	-	-	-	-	
		Clay	100	20.9	25.8 (Albite)	2.7	4.8	0	0	0	0	18.8	7.5	Amorphous (19.5%)	26.3	100	

KI=Kübler Index (units of Δ°2θ)
AI=Årkaei Index (units of Δ°2θ)

2246

Supplementary Table S3. Palynological analysis of mudstone and hemipelagites, Fezadeash Formation, Yukon, Canada.

Sample	Lithology	Spores	Pollen	AOM	Phytoclasts	Other
1-1	Mudstone	Trilete, dark brown, corroded	Monosulcate grain, dark brown, corroded	Black debris, round particles, dark brown to black, semi-opaque or opaque; Irregular 'fluffy' masses, dark brown and partly translucent; Globular masses, dark brown, degraded <i>Botryococcus</i> colonies ?	Black phytoclasts	Pyrite
1-2	Mudstone	Barren	Bisaccate grain, dark brown to black, corroded	black debris, round particles, dark brown to black, semi-opaque or opaque; irregular 'fluffy' masses, dark brown and partly translucent		
1-3	mudstone	Barren	Monosulcate grain, black, corroded	black debris, round particles, dark brown to black, semi-opaque or opaque		
1-4	mudstone	Trilete, dark brown, corroded	barren	black debris, round particles, dark brown to black, semi-opaque or opaque; irregular 'fluffy' masses, dark brown and partly translucent	black phytoclasts (leaf cuticles?)	
1-5	hemipelagite	Barren	Barren	black debris, round particles, dark brown to black, semi-opaque or opaque; irregular 'fluffy' masses; dark brown and partly translucent	black phytoclasts (leaf cuticles?)	pyrite
GL1-6	hemipelagite	Barren	Barren	black debris, round particles, dark brown to black, semi-opaque or opaque		pyrite
GL1-7	hemipelagite	Barren	Barren	black debris, round particles, dark brown to black, semi-opaque or opaque		
GL1-8	hemipelagite	Barren	Barren	black debris, round particles, dark brown to black, semi-opaque or opaque		

2247

AOM=amorphous organic matter.

Thermal Alteration Index (TAI)= ~4.5.

Table S3. Microfossil analysis of carbonate boulder, Dezadeash Formation, Yukon, Canada (modified from Orchard, 2000).

Sample	Fossils	Age	CAI
247-1	ichthyoliths microbivalves foraminifer conodonts: ramiform elements <i>Neogondolella steinbergensis</i> (Mosher, 1968) <i>Epigondolella bidentata</i> (Mosher 1968)	Late Triassic (Late Norian)	4–4.5

2248

Table S5. Rock-Eval data, Dezadeash Formation, Yukon, Canada.

Sample	Lithology	TOC (wt%)	T _{max} (°C)	S ₁ (mg HC/g rock)	S ₂ (mg HC/g rock)	S ₃ (mg CO ₂ /g rock)	HI	OI
1-3	Hemipelagite	0.03	437	0.01	0.06	0.24	200	800
2-2	Hemipelagite	0.17	451	0.00	0.02	0.35	12	206
3-2	Hemipelagite	0.20	442	0.07	0.03	0.35	15	175
3-9	Hemipelagite	0.12	481	0.00	0.00	0.50	0	413
4-2	Hemipelagite	0.06	-40	0.01	0.00	0.21	0	350
4-7	Hemipelagite	0.15	285	0.16	0.03	0.36	20	240
4-8	Mudstone	1.26	589	0.04	0.06	0.41	5	33
8-5	Hemipelagite	0.08	362	0.01	0.00	0.23	0	288
9-4	Mudstone	0.15	342	0.00	0.00	0.35	0	233
9-6	Hemipelagite	0.17	406	0.01	0.00	0.54	0	318
12-4	Hemipelagite	0.10	428	0.01	0.00	0.38	5	380
12-5	Mudstone	0.19	314	0.12	0.01	0.28	0	147
16-1	Mudstone	0.14	-40	0.00	0.00	0.31	20	221
18-1	Sandstone	0.05	487	0.00	0.01	0.30	0	600
18-4	Hemipelagite	0.04	-40	0.00	0.00	0.42	0	1050
22-1	Mudstone	0.07	421	0.00	0.00	0.35	14	500
23-1	Sandstone	0.07	428	0.00	0.01	0.24	0	343
26-1	Hemipelagite	0.07	430	0.00	0.00	0.27	0	386
28-1	Phyllite	0.01	-40	0.00	0.00	0.28	0	2800
203-1	Mudstone	0.11	-40	0.00	0.00	0.30	0	273
210-1	Hemipelagite	0.25	433	0.00	0.00	0.27	0	108
213-1	Mudstone	0.08	-40	0.00	0.00	0.26	0	325
307-1	Mylonite	0.09	362	0.01	0.00	0.77	0	856

TOC=total organic carbon

T_{max}=Rock-Eval oven temperature at maximum S₂ generation

S₁=hydrocarbons thermally distilled from sample ('free hydrocarbons')

S₂=hydrocarbons generated by pyrolytic degradation of kerogen in sample ('potential hydrocarbons')

S₃=carbon dioxide generated during pyrolysis

HI=Hydrogen Index=(S₂x100/TOC)

OI=Oxygen Index=(S₃x100/TOC)

HC=hydrocarbons

2249